

## Atomic scale simulations on LWR and Gen-IV fuel

**Thesis submitted by Emre ÇAĞLAK**

in fulfilment of the requirements of the PhD Degree in Engineering Sciences and Technology (“Docteur en Sciences de L’Ingénieur et Technologie”)

Academic year 2021-2022

Supervision: Prof. Pierre-Etienne Labeau (ULB)

Co-supervision: Prof. Dirk Lamoen (UA)

Dr. Marc Verwerft (SCK CEN)

### **Thesis jury:**

Nicolas PAULY (ULB, Chair)

Pierre-Etienne LABEAU (ULB, co-promoter)

Dirk LAMOEN (UA, Co-promoter)

Marc Verwerft (SCK CEN, Co-promoter)

Jérémy DOHET-ERALY (ULB, Secretary)

Michel FREYSS (CEA, External)

**sck cen**



*"İki Mustafa Kemal vardır: Biri ben, et ve kemik, geçici Mustafa Kemal... İkinci Mustafa Kemal, onu "ben" kelimesiyle ifade edemem; o, ben değil, bizdir! O, memleketin her köşesinde yeni fikir, yeni hayat ve büyük ülkü için uğraşan aydın ve savaşçı bir topluluktur. Ben, onların rüyasını temsil ediyorum. Benim teşebbüslerim, onların özlemini çektikleri şeyleri tatmin içindir. O Mustafa Kemal sizsiniz, hepinizsiniz. Geçici olmayan, yaşaması ve başarılı olması gereken Mustafa Kemal odur!"* **Mustafa Kemal ATATURK**

---

1 "There are two Mustafa Kemal: one is me, flesh and bone, temporary Mustafa Kemal... The second Mustafa Kemal, I cannot express him with the word "I "; he is not me, he is us! He is a new idea, new life and great in every corner of the country. It is a community of intellectuals and warriors striving for this ideal. I represent their dream. Mustafa Kemal's undertakings are for the satisfaction of what they long for. That is Mustafa Kemal - all of you. This Mustafa Kemal, who is not temporary, must live and succeed!" **Mustafa Kemal ATATURK**, own translation.



## **Acknowledgements**

This PhD thesis is dedicated to the memory of my initial scientific advisor Prof. Alain Dubus.

First and foremost, I would like to thank my scientific advisors: Prof. Pierre-Etienne Labeau, Prof. Dirk Lamoen, Dr. Marc Verwerft and Dr. Kevin Govers, for all their help and advice.

I am in debt to my parents, my siblings and my partner Dr. Andrea Winterstetter and my daughter Charlotte Ezgi for their understanding and limitless support which allowed me to pursue my research to such extent. The financial support of this research by SCK CEN is gratefully acknowledged.

## Abstract

Fundamental understanding of the behaviour of nuclear fuel has been of great importance. Enhancing this knowledge not only by means of experimental observations, but also via multi-scale modelling is of current interest. The overall goal of this thesis is to understand the impact of atomic interactions on the nuclear fuel material properties. Two major topics are tackled in this thesis. The first topic deals with non-stoichiometry in uranium dioxide ( $\text{UO}_2$ ) to be addressed by empirical potential (EP) studies. The second fundamental question to be answered is the effect of the atomic fraction of americium (Am), neptunium (Np) containing uranium (U) and plutonium (Pu) mixed oxide (MOX) on the material properties.

$\text{UO}_2$  has been the reference fuel for the current fleet of nuclear reactors (Gen-II and Gen-III); it is also considered today by the Gen-IV International Forum for the first cores of the future generation of nuclear reactors on the roadmap towards minor actinide (MA) based fuel technology. The physical properties of  $\text{UO}_2$  highly depend on material stoichiometry. In particular, oxidation towards hyper stoichiometric  $\text{UO}_2 - \text{UO}_{2+x}$  – might be encountered at various stages of the nuclear fuel cycle if oxidative conditions are met; the impact of physical property changes upon stoichiometry should therefore be properly assessed to ensure safe and reliable operations. These physical properties are intimately linked to the arrangement of atomic defects in the crystalline structure. The first paper evaluates the evolution of defect concentration with environment parameters – oxygen partial pressure and temperature by means of a point defect model, with reaction energies being derived from EP based atomic scale simulations. Ultimately, results from the point defect model are discussed, and compared to experimental measurements of stoichiometry dependence on oxygen partial pressure and temperature. Such investigations will allow for future discussions about the solubility of different fission products and dopants in the  $\text{UO}_2$  matrix at EP level.

While the first paper answers the central question regarding the dominating defects in non-stoichiometry in  $\text{UO}_2$ , the focus of the second paper was on the EP prediction of the material properties, notably the lattice parameter of Am, Np containing U and Pu MOX as a function of atomic fractions.

The configurational space of a complex  $\text{U}_{1-y-y'-y''}\text{Pu}_y\text{Am}_{y'}\text{Np}_{y''}\text{O}_2$  system, was assessed via Metropolis-Monte Carlo techniques. From the predicted configuration, the relaxed lattice parameter of Am, Np bearing MOX fuel was investigated and compared with available

literature data. As a result, a linear behaviour of the lattice parameter as a function of Am, Np content was observed, as expected for an ideal solid solution. These results will allow to support and increase current knowledge on Gen-IV fuel properties, such as melting temperature, for which preliminary results are presented in this thesis, and possibly thermal conductivity in the future.

**Keywords:** Non-stoichiometry, point defect model, defect chemistry, hybrid Monte Carlo Molecular Dynamics simulation, nuclear fuel, uranium dioxide, americium, neptunium bearing uranium, plutonium MOX fuel, material properties of Light Water Reactor (LWR) and Gen-IV fuel.

## List of Appended Papers

- I. E. Caglak, K. Govers, D. Lamoen, P.-E. Labeau, M. Verwerft, Atomic scale analysis of defect clustering and predictions of their concentrations in  $\text{UO}_{2+x}$ , J. Nucl. Mater. 541 (2020) 152403.
- II. E. Caglak, P.-E. Labeau, Lattice parameter of Am, Np bearing MOX fuel: an empirical potential study, J. Phy. Commun. (2021) 5 035012.

## Contribution to the Papers (I-II)

**Emre Caglak:** Conceptualization, Methodology, Software, Validation, Formal analysis, Investigation, Resources, Data curation, Writing - original draft, Writing - review & editing, Visualization.



## Contents

1.	How physics matter for the safe operation of nuclear facilities: The bigger picture.....	1
1.1.	Nuclear fission and nuclear fuel.....	1
1.2.	Nuclear fuel cycle.....	5
1.3.	GEN-IV fuel concept .....	15
1.4.	The objectives and structure of this thesis .....	16
2.	The uranium-oxygen system .....	17
2.1.	Crystal structure of $\text{UO}_2$ .....	18
2.2.	Material properties of $\text{UO}_2$ .....	18
2.3.	State-of-the-art research .....	25
3.	Techniques.....	27
3.1.	Empirical potentials in ionic crystal.....	28
3.2.	Static calculations.....	30
3.3.	Molecular dynamics simulations.....	33
3.4.	Monte Carlo simulations .....	34
3.5.	Defect chemistry .....	35
4.	Proposed approach: configurational space exploration .....	40
4.1.	Monte Carlo (MC) – Molecular Dynamics (MD) method.....	40
4.2.	Rigid lattice approach.....	42
4.3.	Verification of methods.....	44
4.4.	Performance assessment.....	50
5.	Validation of the proposed approach: application to defect chemistry in $\text{UO}_{2+x}$ .....	51
6.	Application to Gen-IV fuels .....	53
7.	Conclusions & Outlook .....	59
8.	List of Figures.....	64
9.	List of Tables .....	68

10.	List of Abbreviations / Acronyms.....	69
11.	Bibliography .....	73
12.	Annex (Paper I & II).....	82

# 1. How physics matter for the safe operation of nuclear facilities: The bigger picture

The overall goal of this thesis is to understand the impact of atomic interactions on the nuclear fuel properties, which is ultimately linked to the fuel performance. Therefore, in the first two chapters the rationale of this thesis is presented by highlighting the relevance of a fundamental understanding of the physics involved to design, develop, and operate nuclear facilities. Some basic background together with relevant definitions related to nuclear technology and its key material, namely nuclear fuel, are provided in the first two chapters.

- Section 1.1 briefly describes nuclear fission and the features of nuclear fuel.
- Section 1.2 explains the nuclear fuel cycle starting from uranium metal mining over energy production until its final waste management.
- Section 1.3 details the Gen-IV nuclear fuel concept
- Section 1.4 explains the objectives and structure of the thesis
- Section 2.1 describes the crystal structure of UO<sub>2</sub>
- Section 2.2 describes the material properties of UO<sub>2</sub>
- Section 2.3 outlines the state of art research of atomic scale calculations in UO<sub>2</sub>

## 1.1. Nuclear fission and nuclear fuel

Fission event:

A nuclear fission event is defined as the splitting of a heavy nuclide into usually two fragments [1]. Some heavy nuclides, such as <sup>242</sup>Cm and <sup>252</sup>Cf, feature spontaneous fission; for others, such as <sup>233</sup>U, <sup>235</sup>U and <sup>239</sup>Pu, a captured neutron activates this event. An alternative way of inciting fission is through photons bombardment or excitation of the nucleus via high energy particles e.g., protons, deuterons, and helium. An example for neutron induced fission of a <sup>235</sup>U is shown in Eq. (1-1) [2,3].



The products of such reactions e.g., fission products (FPs), fast neutrons ( $n$ ) and gammas ( $\gamma$ ) appear with large kinetic energy (about 200 MeV), which is then converted into heat to eventually produce electrical power in nuclear reactors.

The distribution of fission fragments is generally measured by mass spectroscopic and chemical techniques [4]. Figure 1-1 shows a typical  $^{235}\text{U}$  fission yield as a function of fragment mass [5]. Fission events are generally asymmetric, in the sense that they most often produce a light and a heavier fragment, rather than two fragments of a same mass. In general, fission fragments ranging from atomic mass ( $A$ ) of 72 to 161 result from a thermal neutron induced  $^{235}\text{U}$  fission reaction.

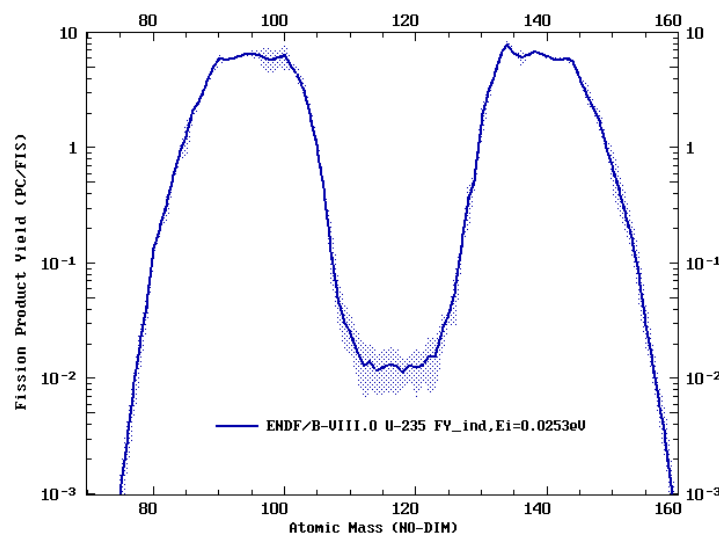


Figure 1-1  $^{235}\text{U}$  fission yield (FY) as a function of fragment mass.  $E_i$  is the incoming neutron energy. ENDF stands for US Evaluated Nuclear Data File / version B-VIII.0. (From [5].)

In addition, during the fission reaction several neutrons are produced. Most of these neutrons appear as ‘prompt neutrons’ right after the fission event, while very few of them (typically less than 1%) appear with a gradual delay, which is crucial for the effective control of a nuclear reactor. The average numbers of immediately released neutrons and delayed neutrons emitted per fission of  $^{235}\text{U}$  are  $2.432 + 0.066E_i$  ( $0 \leq E_i \leq 1$  MeV) and  $2.349 + 0.15E_i$  ( $E_i > 1$  MeV), and  $0.01668 \pm 0.0007$ , respectively. With an average neutron energy of about 2 MeV, these neutrons propagate the fission chain reaction [6].

For the abundant isotope of uranium,  $^{238}\text{U}$  fissions occur above 1 MeV incident neutron energy [5]. However, when capturing an additional neutron,  $^{238}\text{U}$  becomes unstable and decays to

$^{239}\text{Pu}$ . Eq. (1-2) shows a typical neutron capture reaction of a  $^{238}\text{U}$  isotope.  $^{239}\text{Pu}$ , in turn, is a fissile isotope with a half-life of 24 thousand years, which can be stored and used as a nuclear fuel.

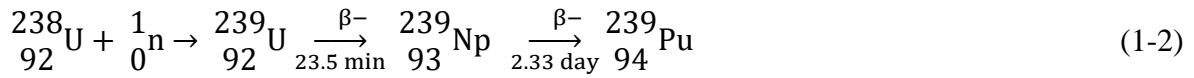


Figure 1-2 shows the energy dependence of the cross section for the neutron induced fission reaction for  $^{235}\text{U}$ ,  $^{238}\text{U}$  and  $^{239}\text{Pu}$  [5]. The higher cross section of  $^{235}\text{U}$  and  $^{239}\text{Pu}$  occurs at low neutron energies; the fission cross section behaves  $\sim v^{-1}$ , with neutron speed ( $v$ ) or  $\sim E_i^{-1/2}$  for the neutron energies being less than  $\sim 1$  eV, called thermal energies.  $\sim 1$  eV to  $\sim 100$  eV are epithermal neutrons, and their reactions exhibit a large resonance in the cross section. Between  $\sim 100$  eV to 1 MeV, the energy levels of excited states in the nuclei overlap and no resonance appears. The neutrons with energies higher than 1 MeV are called fast neutrons. In the fast region, the fission cross section of  $^{235}\text{U}$  and  $^{239}\text{Pu}$  decreases roughly in the order of 1 to 1000 barns, while the fission probability of  $^{238}\text{U}$  increases in a similar order [6].

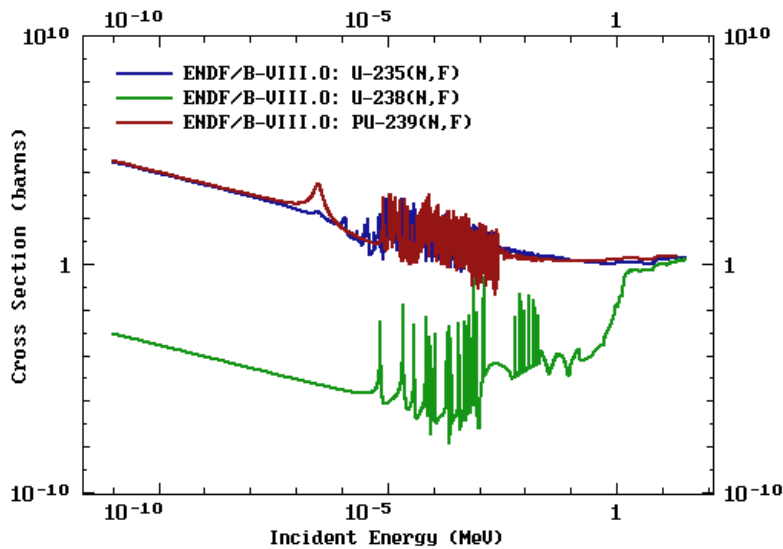


Figure 1-2 Comparison of total fission cross-sections of  $^{235}\text{U}$ ,  $^{238}\text{U}$  and  $^{239}\text{Pu}$ . ENDF stands for US Evaluated Nuclear Data File / version B-VIII.0. (From [5].)

## Nuclear Fuel:

The energy source within the core of a nuclear reactor is the nuclear fuel. It produces heat via fission reactions, which is converted into electricity or used for other applications. Nuclear fuel is made of fissile and fertile or fissionable materials. Uranium is the key material of any nuclear fuel. In nature, it exhibits an isotopic composition of ~99.284%  $^{238}\text{U}$ , ~0.711%  $^{235}\text{U}$  and trace amount of  $^{234}\text{U}$  [7]. Depending on the design of a nuclear reactor, nuclear fuels are produced in various forms, compositions and geometries [8].

The most common classification of nuclear fuel is the form, differentiating between metal and ceramic fuels. Metallic fuels are made from pure uranium or plutonium metals or their Mo, Zr etc., alloys. Pure metals are, however, avoided as they exhibit several polymorphs which make fuel fabrication exceedingly difficult. Ceramic fuels are oxides, nitrides, carbides or silicides. Further, there are more complex materials taking the form of cercer (ceramic–ceramic combinations) or cermet (ceramic–metal composites) [8–10].

There are many criteria which have an impact on the selection of nuclear fuel. Metallic fuels, for example, are attractive in terms of thermal conductivity and fuel density. However, low melting point, phase changes during irradiation, low irradiation and thermal resistivity, and fuel swelling due to lack of porosity are some of the main drawbacks associated with metallic fuels [8–10]. Oxides, on the other hand, have a high melting point and both irradiation and chemical stability, but low thermal conductivity [8–10]. Alternative fuels, such as carbides, nitrides, silicides and dispersed fuels, might be better in many aspects as compared to the oxides and metallic fuels; however, insufficient knowledge makes it hard to use them [8–10].

Modern power reactors utilize ceramic uranium dioxide ( $\text{UO}_2$ ) with ~10  $\mu\text{m}$  grain size and ~5% volume porosity, with a composition of 3-5% enriched  $^{235}\text{U}$  in a cylindrical pellet of ~1 cm diameter and height [8]. Figure 1-3 a) shows a schematic view of a standard double dish chamfered pellet. Figure 1-3 b) depicts the nuclear fuel element, a typically zircaloy sealed tube filled with  $\text{UO}_2$  pellets under 2.5 MPa of helium atmosphere with a height of ~4 m. Figure 1-3 c) displays the nuclear fuel bundle, the assembled unit of fuel elements. In a classical Westinghouse design pressurized water reactor (PWR), the fuel bundle has 17 x 17 fuel element-array with 264 fuel elements, 24 guide tubes and an instrumentation tube [6]. The  $\text{UO}_2$  fuel operates typically at average linear power rate of  $20 \text{ kWm}^{-1}$ , while maximum fuel centreline temperature remains below  $2000 \text{ }^\circ\text{C}$  [6].

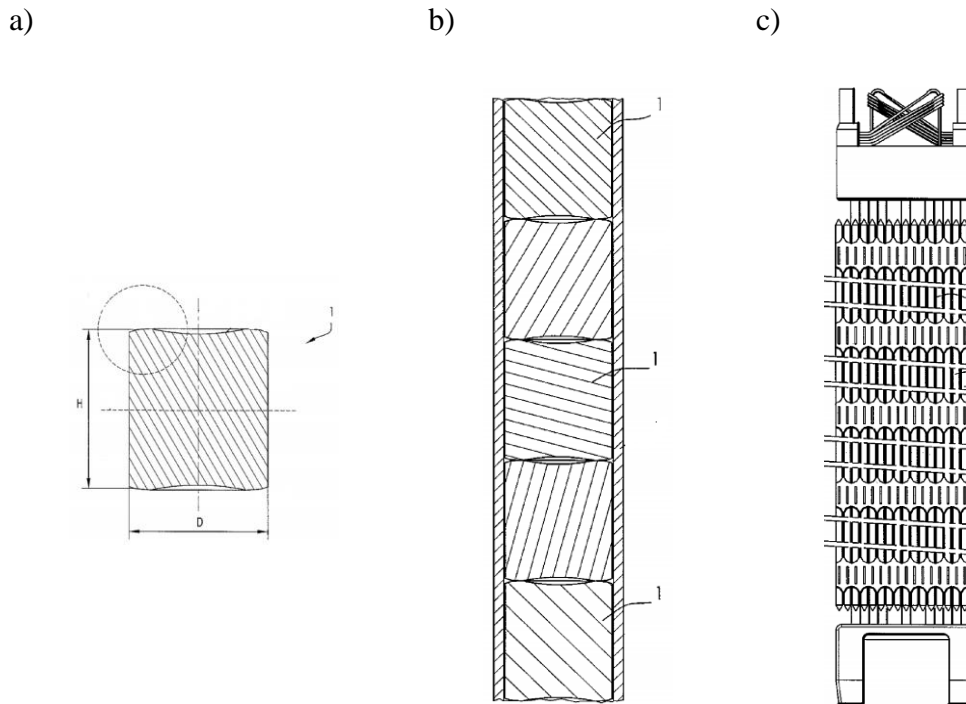


Figure 1-3 Schematic view of a) double dish chamfered fuel pellet, b) nuclear fuel element, and c) nuclear fuel assembly. (From [11].)

## 1.2. Nuclear fuel cycle

The nuclear fuel cycle covers uranium in all relevant stages, that is, from mining until its utilization in a reactor until the management of spent nuclear fuel. Figure 1-4 shows the schematic representation of the uranium nuclear fuel cycle.

### Mining and Milling:

The first step of the nuclear fuel cycle is the extraction of uranium ores from the ground, for which the concentration is high enough to be economically feasible. Uranium naturally occurs with an overall abundance of approximately 3-4 ppm in the Earth's crust [7]. The most common occurrence of uranium is as pitchblende or uranite, in a mixed oxide composition [7].

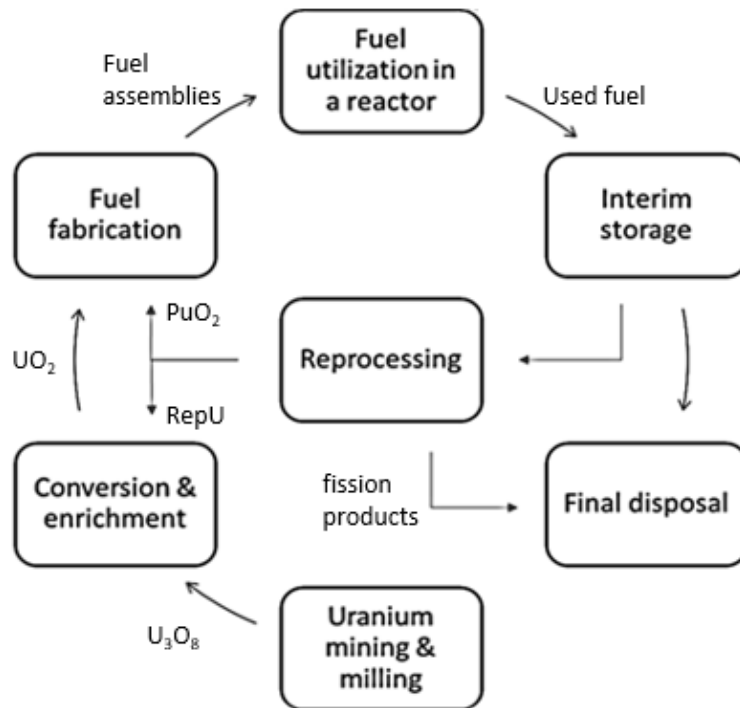


Figure 1-4 Schematic diagram of nuclear fuel cycle (NFC). RepU stands for reprocessed uranium.

Typically, uranium ores can be extracted from the ground in three different ways, namely either by means of open pit mining, underground mining, or in-place (in-situ) leaching. The selected mining strategy depends on a uranium deposit's properties, such as depth, shape and geological conditions [7]. Open pit mining is preferred if the resources are located near the surface, whereas underground mining is used for deeper deposits. In case of solution mining, liquid solutions are pumped through the ore to recover uranium by leaching on site. Even though the selection of in-situ mining results in less tailings, the use of leaching solvents can lead to the contamination of underground water and soil.

Milling is the production stage of yellow cake  $U_3O_8$ . Here the uranium is concentrated to 70-80% for further operations [12]. This stage comprises ore crushing and leaching, followed by solid-liquid separation, concentration, purification, and uranium recovery.



### Refining, Conversion and Enrichment:

Following the milling stage,  $U_3O_8$  is further purified by solvent extraction with tri-butyl phosphate (TBP) and then exposed by chemical conversion techniques. The obtained  $UO_2$  will either directly be shipped to a fuel manufacturing facility or converted to uranium hexafluoride for further isotopic enrichment process. A typical uranium-fluoride reaction is shown in Eq. (1-3).



The product of green salt  $UF_4$  is converted to gaseous  $UF_6$  by  $F_2$  fluorination [12]. Metallic uranium can also be produced by metallothermic reduction methods [12].

Enrichment is a physical separation process, which uses the mass difference between  $^{238}U$  and  $^{235}U$ . The aim is to increase the  $^{235}U$  isotopic content from 0.711% to 3-5% for energy production. Different processes of isotopic enrichment are economically feasible:

- Gaseous diffusion takes advantage of the fact that at a certain temperature, lighter molecules diffuse faster than heavier molecules. A central membrane is used in order to separate the two molecules  $^{235}UF_6$  and  $^{238}UF_6$  [12].
- Gas centrifugation uses a high-speed rotating container. The difference in the centrifugal forces of heavy and lighter molecules is used for the separation of the two molecules  $^{235}UF_6$  and  $^{238}UF_6$  [12].

The feasibility and commercial reliability of other available enrichment techniques, such as electromagnetic separation, laser enrichment, chemical exchange, plasma separation etc., is still subject to R&D [12].

### Deconversion:

To convert the enriched  $UF_6$  to  $UO_2$ , several routes have been industrially implemented, but we will limit ourselves here to a description of the Integrated Dry Route (IDR). First uranium oxyfluoride  $UO_2F_2$  powder is produced from  $UF_6$  reacting with heated steam  $H_2O$ , typically at 400 °C [12]. Then, the  $UO_2F_2$  is defluorinated and heated to  $UO_2$  with a steam-hydrogen

mixture, typically at 600 °C [12]. After cooling, the UO<sub>2</sub> powders are collected in containers, which maintain a critically safe geometry, and are shipped to the fuel manufacturing plant.

### Fuel Fabrication:

UO<sub>2</sub> powders from deconversion further undergo the following steps before being refuelled into a nuclear reactor:

- Powder preparation
- Fuel pellet processing
- Fuel rod fabrication
- Fuel bundle assembly

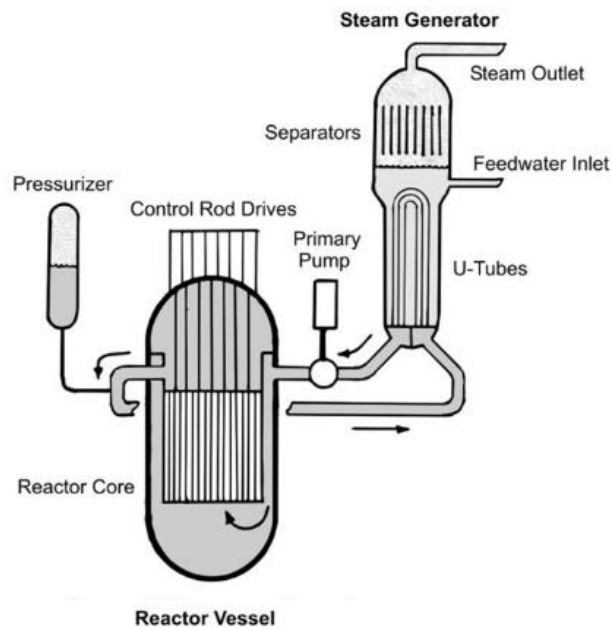


Figure 1-5 A typical pressurised water reactor (PWR) nuclear steam supply system (NSSS). (From [13].)

The powder preparation comprises homogenisation, blending with additives, pre-compaction and granulation, spheroidization and lubrication phases [14]. In each of these phases, quality control and quality assurance are crucial for safe reactor operation.

The prepared and blended powder is sintered at high temperatures and in a reducing atmosphere into green pellets [14]. The pellets are then loaded into a rod with helium, which is subsequently sealed. Eventually the rods are assembled into fuel bundles [14].

Nuclear power plants:

In a commercial plant, the heat generated by the nuclear fission is used to convert water into high temperature and pressure steam. The steam’s latent energy is converted first to mechanical energy by a turbine and then into electricity by a generator, which is connected to the electrical grid. To complete the cycle, the used steam must be condensed and pumped back into the nuclear steam supply system (NSSS). The condensed water is usually obtained from cooling by a nearby water source (often from rivers, lakes, or the sea) and/or artificial cooling towers.

Nuclear reactors are generally referred to, based on the type of coolant. Ordinary water, as used in LWRs (Light Water Reactor), is the most common type of coolant and serves also as a neutron moderator. Table 1-1 displays various data of different types of nuclear power reactors. Among the LWRs, PWRs (Pressurized Water Reactor) are the majority. A typical NSSS of a PWR design, consisting of a nuclear reactor, primary coolant loops, circulation devices and a steam generator, is shown in Figure 1-5 [13]. In a typical Westinghouse PWR-1200 reactor with a discharge burnup of 33-50 GWdtU<sup>-1</sup>, the high-pressure (15.5 MPa) coolant enters the core at 300 °C and exits at 332 °C [6].

Table 1-1 A typical nuclear power reactor data (From [6].)

<b>General data</b>	<b>PWR (W)</b>	<b>PWR (B&amp;W)</b>	<b>PWR (CE)</b>	<b>BWR/6</b>	<b>HTGR</b>	<b>LMFBR</b>	<b>GCFR</b>	<b>CANDU PHWR</b>
<b>MW<sub>th</sub></b>	3411	3600	3800	3579	3000	2410	2530	1612
<b>MW<sub>e</sub></b>	1150	1200	1300	1200	1170	1000	1000	500
<b>η [%]</b>	33.7	33.3	34.2	33.5	39.0	39.0	39.5	31.0
<b>Fuel type</b>	UO <sub>2</sub>	UO <sub>2</sub>	UO <sub>2</sub>	UO <sub>2</sub>	UC, ThO <sub>2</sub>	PuO <sub>2</sub> , UO <sub>2</sub>	PuO <sub>2</sub> , UO <sub>2</sub>	UO <sub>2</sub>
<b>Coolant</b>	H <sub>2</sub> O	H <sub>2</sub> O	H <sub>2</sub> O	H <sub>2</sub> O	He	Na	He	D <sub>2</sub> O
<b>Cladding material</b>	Zircaloy	Zircaloy	Zircaloy	Zircaloy-2	Graphite	316SS	316SS	Zircaloy-4
<b>Moderator</b>	H <sub>2</sub> O	H <sub>2</sub> O	H <sub>2</sub> O	H <sub>2</sub> O	graphite	-	-	D <sub>2</sub> O

Vendor codes are as follows:

W= Westinghouse; B&W=Babcock & Wilcox Company; CE=ABB Combustion Engineering

PWR = Pressurized-water reactor; BWR = Boiling-water reactor; HTGR= High temperature gas reactor; LMFBR=Liquid metal fast breeder reactor; GCFR=gas-cooled fast reactor; CANDU=CANada deuterium uranium; PHWR=Pressurized-heavy water reactor.

### Spent fuel interim storage:

In a normal operating scenario, one-third of the core of a nuclear reactor is discharged and replaced with fresh fuel every 12 to 18 months [15]. Managing the discharged (or spent) nuclear fuel from nuclear reactors is a great challenge as it contains fissile isotopes ( $^{235}\text{U}$ ,  $^{239}\text{Pu}$ ,  $^{241}\text{Pu}$ ), minor actinides [MAs (Am, Np, Cm, mainly)] and fission products.

The idea of an interim storage is to reduce the activity and heat output of the fuel after removal from the reactor to a relatively safe margin. Later, spent nuclear fuel will be either disposed or shipped to reprocessing facilities.

For the interim storage of spent nuclear fuel, two concepts are in use:

- Wet storage (on-site)
- Dry storage (near the site or off-site)

During the first year of wet storage, the radioactivity of spent fuel (SF) drops to about 1% of its initial value, followed by another reduction of a factor 10 over the subsequent 10 years of cooling [12].

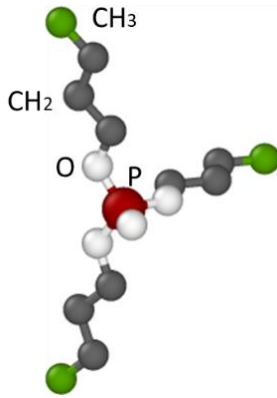
### Reprocessing:

The most widely used method for the reprocessing of spent nuclear fuel is the PUREX process. PUREX is the abbreviation of Plutonium URanium EXtraction, Plutonium Uranium Recovery by EXtraction or Plutonium Uranium Reduction Extraction. These PUREX facilities are designed and licensed depending on the discharge burnup, the fissile content and/or the cooling time of SF [12].

PUREX comprises the uranium and plutonium extraction and purification after dissolving SF with nitric acid. This process can be described as the separation of uranium and plutonium from the fission products first, and later partially or completely from each other. A 30% v/o TPB (tri n- butyl phosphate) diluted with paraffinic hydrocarbons, such as n-dodecane, kerosene etc., is commercially used as an organic solvent [12]. Figure 1-6 depicts the molecular structure of TBP and a typical diluent: n-dodecane molecule.

a) Tri-n butyl phosphate (TBP)

Chemical formula:  $(\text{CH}_3\text{CH}_2\text{CH}_2\text{CH}_2\text{O})_3\text{PO}$



b) Hydrocarbon: n-dodecane (nDD)

Chemical formula:  $\text{CH}_3(\text{CH}_2)_{10}\text{CH}_3$

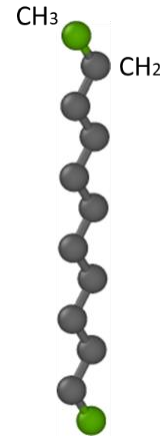
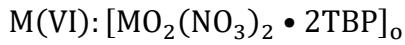


Figure 1-6 The molecular structure of tri butyl phosphate (TBP) and hydrocarbon: n-dodecane (nDD).

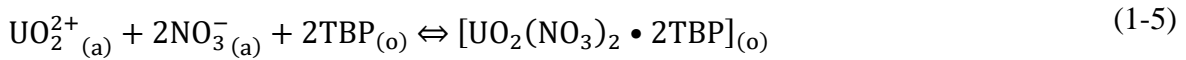
The PUREX process includes the following steps [12]:

- De-cladding (de-jacketing)
- Dissolution
- Feed preparation
- Co-decontamination and partition
- Uranium purification
- Plutonium purification
- Uranium and plutonium reversion to oxides

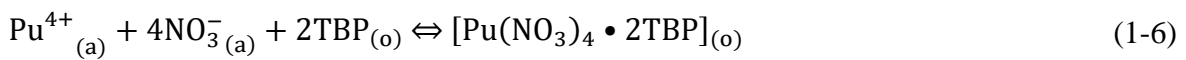
TBP extraction makes advantages of the extractable aqueous nitrate complexes of the elements. Figure 1-7. shows the effect of nitric acid concentration on the distribution coefficient of various metals at room temperature [12]. This confirms the high selectivity of TBP for the separation of uranium and plutonium from other elements. For the various valence (e.g., III, IV and VI) of metals (M), the TPB extraction mechanism is shown in Eq. (1-4).



For example, uranium metal M(VI), and plutonium metal M(IV), react with TBP according to the reaction in Eq. (1-5) and Eq. (1-6), respectively. In these equations the subscript (a) is the aqueous phase while the subscript (o) represents the organic phase [12].



and



For the nitric acid, the TBP extraction mechanism is  $[\text{HNO}_3 \cdot n\text{TBP}]_o$  where n is 1 and 2, dominantly [12]. TBP is covalently bonding with metal ions, whereas hydrogen bonding with nitric acid and water [12]. Partitioning of uranium and plutonium is achieved by reduction of Pu (IV) to non-extractable Pu (III). After the purification, uranium and plutonium are converted to their oxides.

#### Waste disposal:

Currently, most of the spent nuclear fuels are kept temporarily in spent fuel pools at the reactor site or in special casks, near the site or off-site. Uncertainty remains on the topic of permanent (or final) disposal of the spent nuclear fuel due to environmental, technical, economical, and political reasons.

The most realistic method is the storage of spent nuclear fuel in deep underground repositories, where it may remain confined and isolated from biosphere for very long periods of time. Confinement and isolation are foreseen to be achieved by multiple barriers in such repositories. The radioactive waste is placed into a steel canister in a special form that blocks mobilization

of radioactive materials. That canister is covered by multiple engineered barriers in order to prevent the SF from any physical and chemical damage or to delay such occurrences to times where the waste radiotoxicity has sufficiently decreased [12].

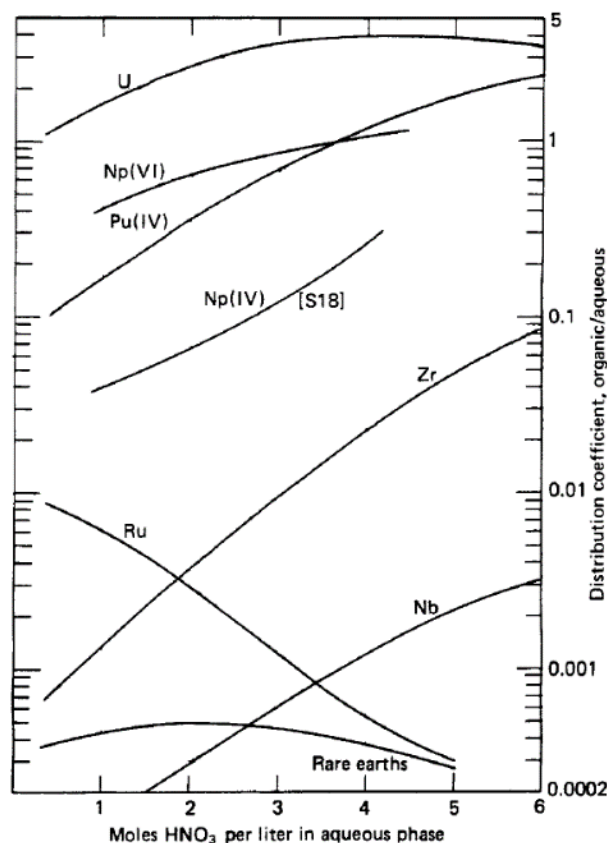


Figure 1-7 Effect of nitric acid concentration on distribution coefficients in 30% v/o TBP 80% uranium saturation at room temperature. (From [12].)

### Nuclear fuel cycle: overview and challenges

The use of nuclear technology requires several different industrial facilities. The necessary steps for uranium to be turned into nuclear fuel are illustrated in Figure 1-4. There are two scenarios for nuclear fuel: once-through (or open) nuclear fuel cycle (NFC) and closed NFC. The former considers the direct disposal of nuclear fuel after irradiation in a reactor and the latter refers to the reprocessing or re-use of nuclear fuel after irradiation in a reactor. There are many factors that can have an impact on the choice of the type of NFC [16]:

Safety: in uranium mining, fuel fabrication, spent fuel handling and treatment, geological disposal as well as all the transportations.

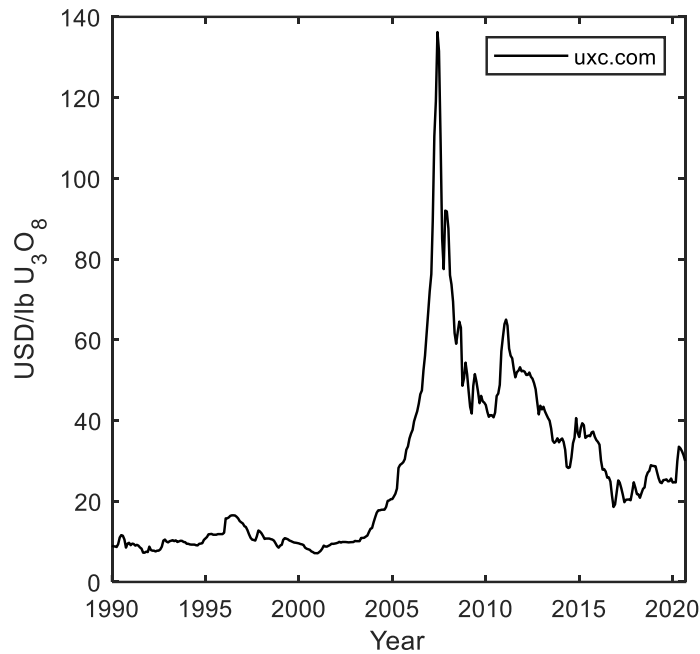


Figure 1-8 Uranium spot price in USD per pound from 1990 to 2021.

Sustainability: covers e.g., efficient nuclear resource utilization, sustainability on the interim storage and reprocessing and nuclear waste management.

Non-proliferation and security: the possibility to divert or access fissile materials, being it from institutional side or malevolent group of people.

Economy: Overall cost e.g., uranium spot prices, fuel fabrication cost, the cost of back-end facilities, cost of transportation, disposal, and personnel and so on.

Although once-through nuclear fuel cycle is generally accepted, closing the cycle would provide better nuclear resource utilization and significant decrease of volume of the high-level waste. For example, with an open NFC, natural uranium utilization is 200 tonnes per year for



1000-MWe PWR reactor at 80 percent capacity factor. On the other hand, this value decreases by a factor 100 with fully closed cycle with fast reactor [12]. However, the cost would probably be compensated by additional back-end facilities. The main determining factor will therefore be the future uranium prices. Figure 1-8 shows the uranium spot prices in the market from 1990 to 2021. In the global picture, selecting of open or closed cycle might differ from one country to another.

### 1.3. GEN-IV fuel concept

The management of spent fuel (SF) from Light Water Reactors (LWRs) is a great challenge as it contains many radioactive elements, that is, fissile isotopes ( $^{235}\text{U}$ ,  $^{239}\text{Pu}$ ,  $^{241}\text{Pu}$ ), minor actinides [MAs (Am, Np, Cm, mainly)] and fission products. The main concern is the minimization of long-term environmental effects of the spent nuclear fuel. Therefore, appropriate back-end scenarios have to be elaborated.

Over the decades, many back-end strategies have been devised for safe and sustainable energy production. In the case of a once-through nuclear fuel cycle, currently the most popular scenario is to isolate SFs from the environment. Alternative technologies have been developed in order to re-use and reprocess SFs. The PUREX process, for example, which is the standard method for reprocessing, aims at recycling U and/or Pu as a pure stream, leaving the fission products and MAs in a raffinate, which is classified as high-level waste (HLW). After that, the extracted U and/or Pu is shipped either to fuel fabrication or enrichment facilities.

Partitioning and transmutation (P&T) is considered a future management strategy to reduce the final radiotoxicity and heat load of the SF [17,18]. It includes the extraction (or partitioning) of MAs from PUREX waste and the preparation of MA bearing oxide fuel. The transmuted fuel will then be irradiated under a high energy neutron flux in a Fast Neutron Reactor (FNR) or an Accelerator Driven Hybrid System (ADS) [17,18].

Figure 1-9 shows the radiotoxicity changing with time for one tonne of 10-years-cooled spent nuclear fuel, from a standard PWR reactor with 4.2 wt% initially enriched  $^{235}\text{U}$  at 50 GWd/tHM burn-up [17]. Figure 1-9 a) depicts the contribution of FPs, Pu and MAs to the overall SF's

radiotoxicity. Figure 1-9 b) compares the SF's radiotoxicity of three back-end scenarios where I) represents the once-through nuclear fuel cycle, II) shows the PUREX HLW and III) displays the partitioning of MAs from the PUREX waste stream. The FPs do not have long-term radiotoxic effects; their radiotoxicity drops below the one of natural uranium after about 300 years. For the PUREX waste it would take several thousand (~20.000) years and for the direct disposal of SF one would have to wait ~200.000 years until the radiotoxicity drops under the level of natural uranium.

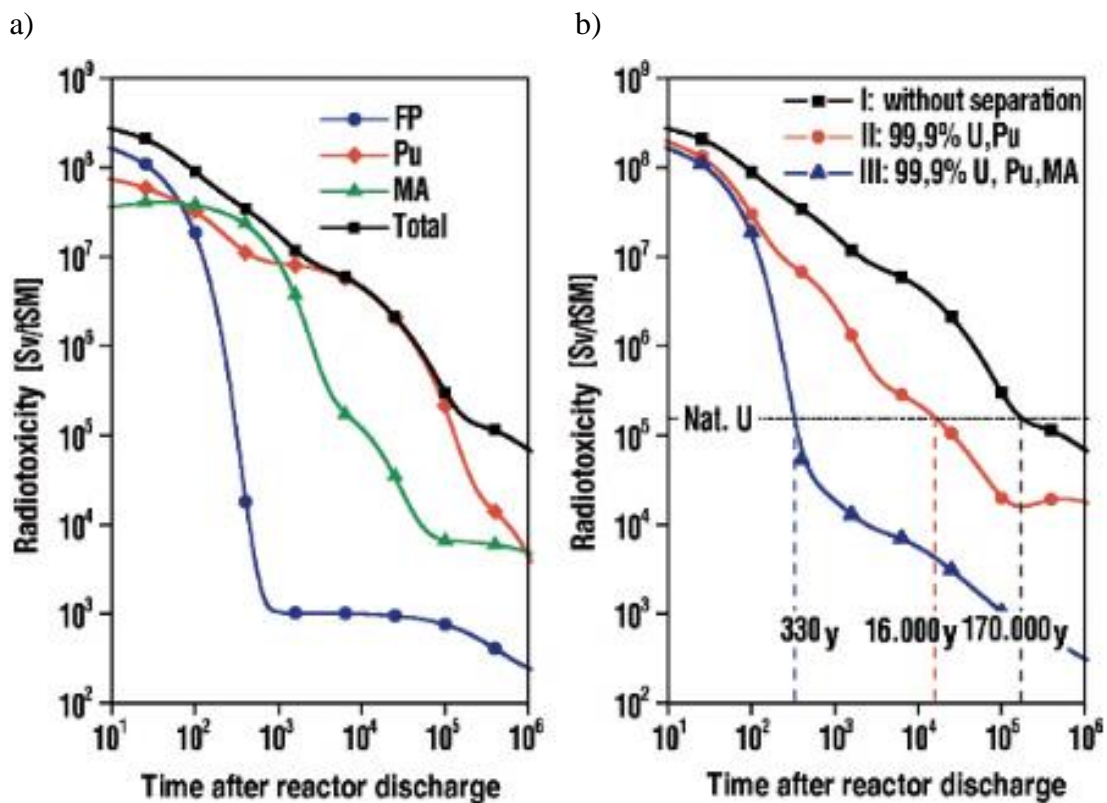


Figure 1-9 Radiotoxicity (Sv/tHM) of 1t of SF from a PWR (initial enrichment 4.2 wt% <sup>235</sup>U, burn-up 50 GWd/tHM) as a function of time after discharge (year). a) Contribution of fission products (FP), plutonium (Pu) and minor actinides (MA) to radiotoxicity. b) Modification of radiotoxicity due to separation of U, Pu or U, Pu and MA. (From [17].)

## 1.4. The objectives and structure of this thesis

The fundamental understanding of the behaviour of nuclear fuel has been of great importance. The overall goal of this thesis is therefore to understand the impact of atomic interactions on the nuclear fuel properties, which is ultimately linked to the fuel performance.

The following research questions are tackled in this thesis:

1. How can non-stoichiometry in uranium dioxide ( $\text{UO}_2$ ) be addressed by empirical potential studies?
2. What are the dominating defects in non-stoichiometric  $\text{UO}_2$ ?
3. How can empirical potentials predict the material properties of americium (Am), neptunium (Np) containing uranium (U) and plutonium (Pu) mixed oxide (MOX) as a function of the atomic fraction?

The thesis is structured as follows: Chapter 1 and 2 provide a short introduction and background, respectively. Chapter 3-4 presents the research design and the methods applied in the articles appended. Chapter 5-6 presents the results and Chapter 7 provides some conclusions and describes potential future research work based on this thesis' outcomes. The papers are integral components of this thesis and can be found in the annex.

## 2. The uranium-oxygen system

Understanding the uranium-oxygen system is important for the nuclear industry as uranium dioxide ( $\text{UO}_2$ ) is a key material for the current fleet of nuclear reactors.  $\text{UO}_2$  is stable at room temperature. At higher temperatures (above  $\sim 600$  K) a non-stoichiometric  $\text{UO}_{2\pm x}$  compound is formed, and with increasing oxidation, the system passes through several intermediate compounds and phases, namely  $\text{U}_4\text{O}_9$ ,  $\text{U}_3\text{O}_7$ ,  $\text{U}_3\text{O}_8$  [19–26]. Figure 2-1 shows the uranium oxygen phase diagram [19]. The first part of this study focuses on the  $\text{UO}_{2+x}$  domain, for which gaining fundamental knowledge is of great technological importance.

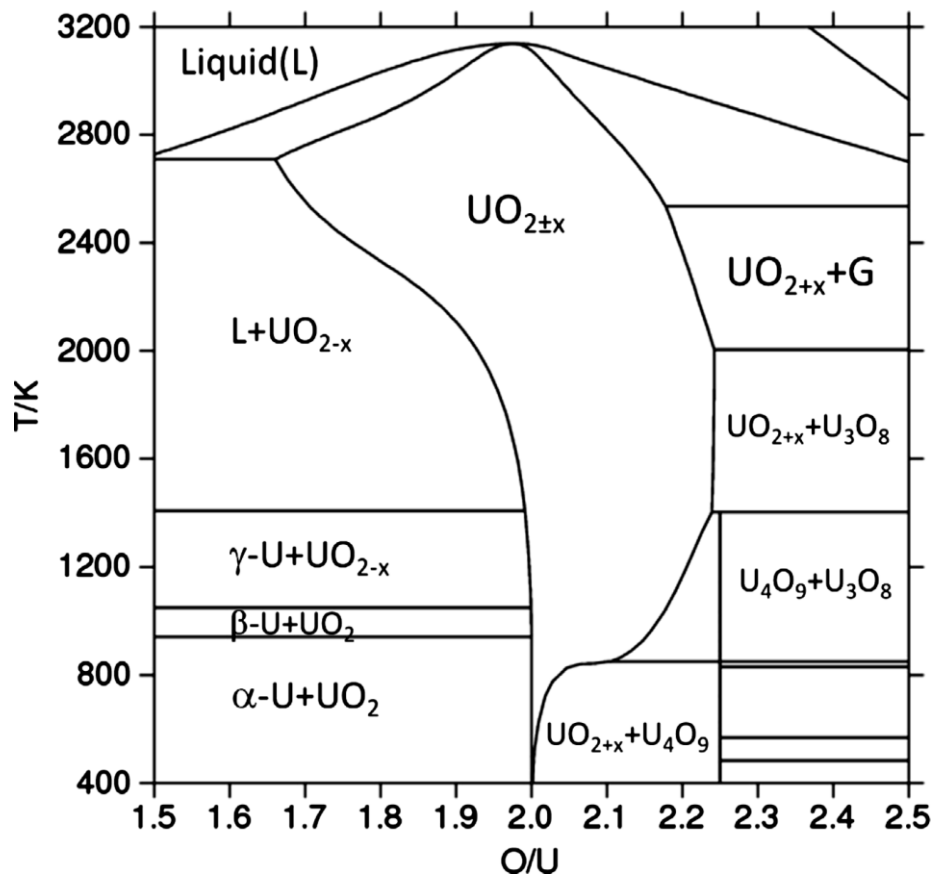


Figure 2-1 Uranium-oxygen phase diagram. (From [19].)

## 2.1. Crystal structure of UO<sub>2</sub>

UO<sub>2</sub> presents a *f.c.c.* type crystal structure (Fm $\bar{3}$ m space group), where uranium ions are located at the Wyckoff 4a octahedral sites and oxygen ions occupy the Wyckoff 8c tetrahedral positions [27]. Figure 2-2 a) and Figure 2-2 b) illustrate the fluorite structure of UO<sub>2</sub> from different perspectives. Figure 2-2 c) shows the thirteen interstitial sites, 12 of them being located along the unit-cell's edge and one interstitial-site being at the unit-cell's centre.

The accepted lattice parameter of UO<sub>2</sub> is 5.47 Å and the corresponding theoretical density is 10.95 gcm<sup>-3</sup> [27,28]. The mean interatomic distances with respect to the nearest neighbour atom are U-U (1<sup>st</sup>-nn) =3.9 Å, O-O (1<sup>st</sup>-nn) =2.7 Å and U-O (1<sup>st</sup>-nn) =2.4 Å at room temperature [27]. Figure 2-3 shows the calculated radial distribution function  $g(r)$  of O-O, U-O and U-U within a  $r=10$  Å (cut-off) distance at 300 K and 3000 K, respectively.

## 2.2. Material properties of UO<sub>2</sub>

Bulk properties of UO<sub>2</sub> were investigated by empirical potential study. A comparison study was carried out between three widely used empirical potential sets, namely Yakub [29], CRG [30,31] and Arima [32], Density Functional Theory (DFT) calculations and experimental results. The Yakub potential was selected as it has been well tested, and because of its ability to adequately address anion clustering formation in UO<sub>2</sub> [29,33,34]. This potential was used to address non-stoichiometry in UO<sub>2+x</sub> in the first paper [35]. Similarly, both the CRG and Arima potential have been extensively tested in literature, especially for dynamic calculations, and reproduce reasonably well thermo-mechanical properties of UO<sub>2</sub> [30,33,36]. In addition, they provide concise sets of interatomic potentials to investigate the material properties of a complex U-Pu-Am-Np-O system [30–32,37,38]. These potentials were used to address the material properties of MA bearing MOX fuel in the second part of the thesis [39].

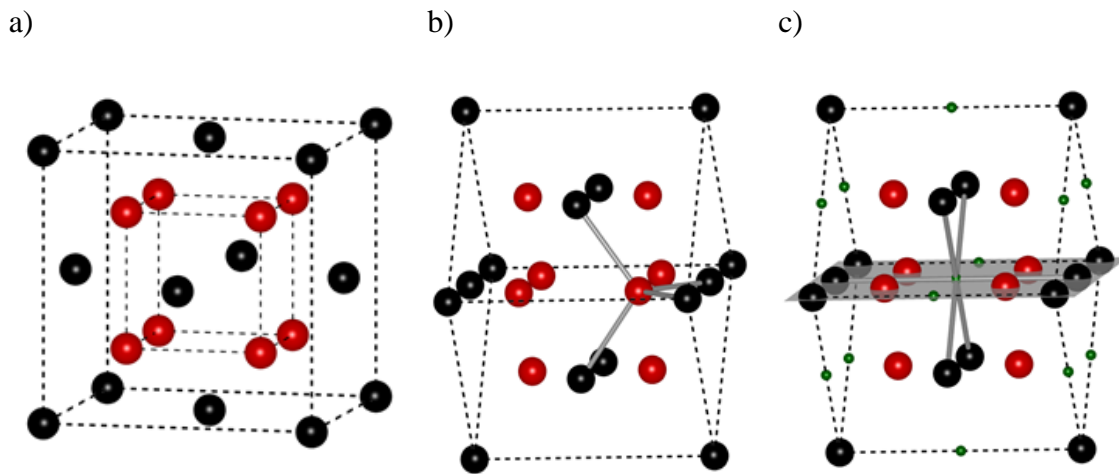


Figure 2-2 a) and b) Various perspectives of the unit cell of uranium dioxide. The black balls represent uranium cations, the red balls stand for oxygen anions and the green balls signify (c) the interstitial sites. The (110) plane of the unit cell, which has 4 oxygen atoms, contains octahedral sites at the mid-point of the plane as well as at the centers of two edges.

Table 2-1. shows the calculated lattice parameters, elastic constant as well as the bulk modulus for various sets of UO<sub>2</sub> potentials. Neither the Yakub nor the Arima potential are capable of reproducing  $C_{12}$  and  $C_{44}$  at the same time [29,32]. This issue was solved by the CRG potential [30,31]. CRG potential sets were therefore selected to study temperature effects on material properties of UO<sub>2</sub> [30,31].

Initially, UO<sub>2</sub> system with 4 x 4 x 4 supercells were heated from 300 K to 3000 K at 50 K intervals with a simulation time step of 2 fs and at zero pressure [33]. System pressure and temperature were controlled by Nosé-Hoover thermostat and barostat with relaxation time of 0.1 ps and 0.5 ps, respectively [33]. At each system temperature, volume and enthalpy were averaged over a certain time period. The averaged lattice parameter and enthalpy were used to calculate the thermal expansion coefficient and specific heat of UO<sub>2</sub>, respectively. Figure 2-4 addresses the temperature effects on material properties of UO<sub>2</sub> as predicted by the CRG potential [30,31]; experimental data were taken from [40].

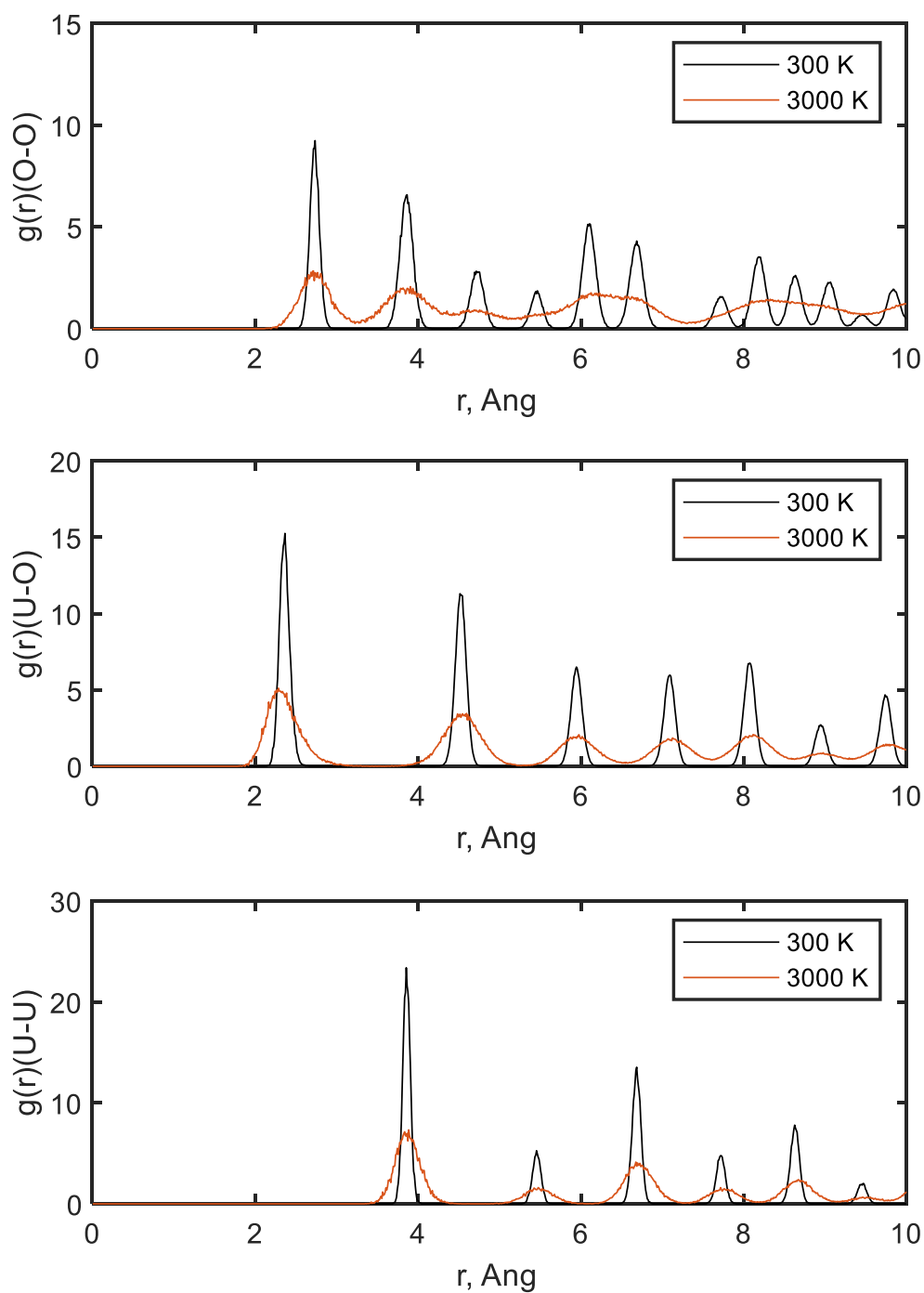


Figure 2-3 The radial distribution function  $g(r)$  of O-O, U-O and U-U within a  $r=10 \text{ \AA}$  (cut-off) distance at 300 K and 3000 K calculated in this thesis using Yakub potential [29].

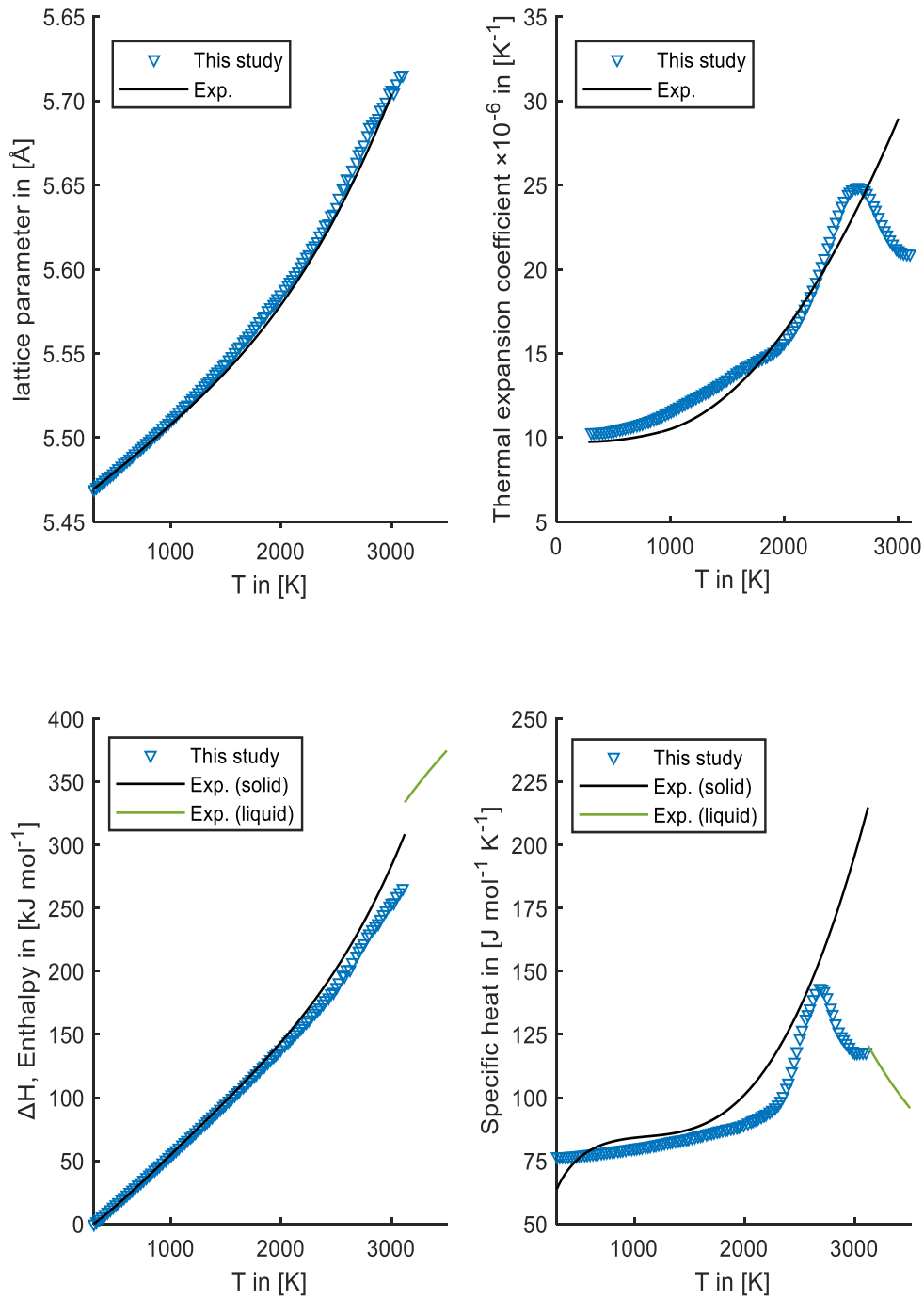


Figure 2-4 Temperature dependence of  $\text{UO}_2$  properties as predicted by CRG potential [30,31] a) lattice parameter [L] b) thermal expansion coefficient  $[\alpha_L = \frac{1}{L}(\frac{\partial L}{\partial T})_P]$  c) change in system enthalpy  $[\Delta H]$  and d) specific heat  $c_p = (\frac{\partial H}{\partial T})_P$ . Experimental data were taken from [40].



Table 2-1 Comparison of bulk properties of UO<sub>2</sub>.

Bulk properties	Yakub [29]	CRG [30,31]	Arima [32]	DFT [41]	Experimental [27,42]
$a_0/\text{nm}$	0.544	0.545	0.545	0.545	0.547
$C_{11}/\text{GPa}$	345.3	406.29	436.02	389.3	389.3±1.7
$C_{12}/\text{GPa}$	71.7	124.70	115.93	138.9	118.7±1.7
$C_{44}/\text{GPa}$	66.7	63.90	106.25	71.3	59.7±0.3
$B/\text{GPa}$	162.9	218.56	222.63	210	209±2

### UO<sub>2+x</sub>

At temperature above ~600 K UO<sub>2</sub> can dissolve oxygen to form UO<sub>2+x</sub> compounds in which the x represents the deviation from stoichiometry or oxidation level [24,43]. Upon oxidation, oxygen ions appear as isolated point defects (O<sub>i</sub>) entering the UO<sub>2</sub> matrix without deforming the lattice structure. These oxygen ions increase the valence state of two uranium ions e.g., from U<sup>4+</sup> to U<sup>5+</sup>. At low values of x in UO<sub>2+x</sub>, a typical oxidation reaction for UO<sub>2</sub> is assumed to occur, as shown in Eq. (2-1).



The deviation from stoichiometry x in UO<sub>2+x</sub> in a regime dominated by isolated oxygen interstitials does not correspond to what is experimentally observed at larger deviation from stoichiometry [20,21]. The higher values of x in UO<sub>2+x</sub> is generally associated with an anion cluster formation [44–49]. Figure 2-5. shows the experimental data for the deviation from stoichiometry x in UO<sub>2+x</sub>.

The well-known di interstitial cluster (2Oi) formation, found by the neutron diffraction experiments performed by Willis, is known to occur at higher departure from stoichiometry [47,50]. In addition, Bevan et al., and Cooper and Willis determined the crystal structure of further oxidation of  $\text{UO}_{2+x}$  to  $\text{U}_4\text{O}_{9-y}$  [22,26]. They concluded that oxygen atoms can even form complex clusters, namely up to the aggregation of five oxygen interstitials with one being at the cluster centre. Based on these pioneering works, the thermodynamic stability conditions of these structures have been intensely discussed [48,51,52]. However, to date, the understanding of these defects' complex nature still remains insufficient. In this thesis, oxygen cluster formation and non-stoichiometry were addressed by empirical potential study.

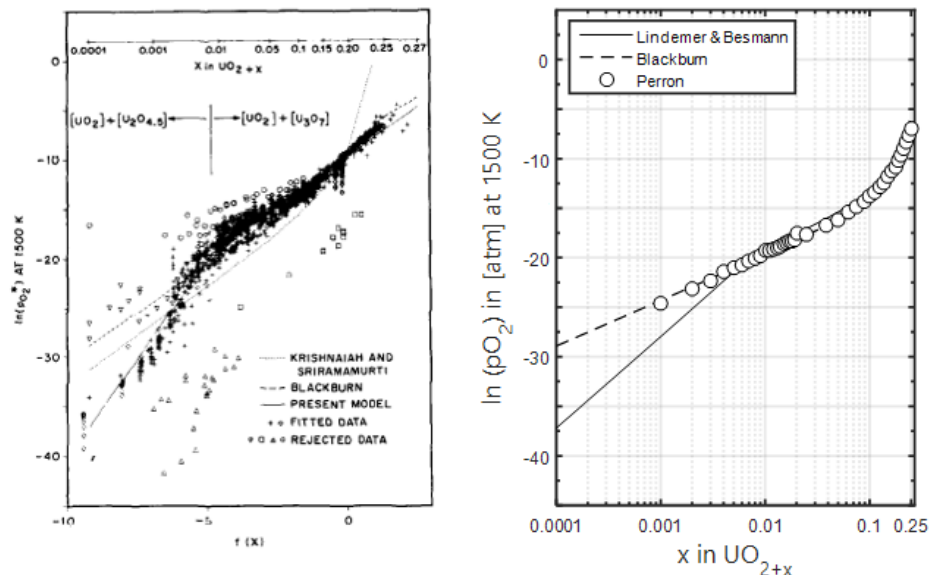
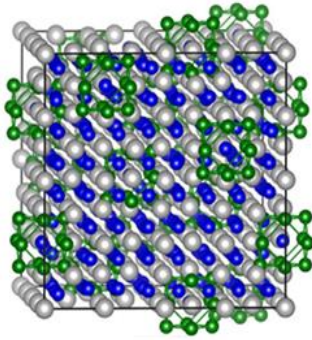


Figure 2-5 The deviation from stoichiometry  $x$  in  $\text{UO}_{2+x}$ . The left graph is taken from Lindemer and Besmann's work, the right graph is the comparison of Blackburn et al.'s, Perron and Lindemer's and Besman's work [20,21,53].

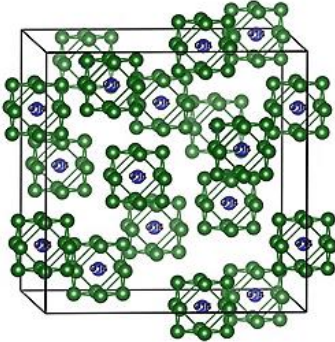
### $\text{U}_4\text{O}_9$

One of the other complicated compounds of the U-O system is  $\text{U}_4\text{O}_9$  because of its non-stoichiometric  $\text{U}_4\text{O}_{9-y}$  form. Three phases of  $\text{U}_4\text{O}_{9-y}$  are known, namely  $\alpha$ - $\text{U}_4\text{O}_{9-y}$ ,  $\beta$ - $\text{U}_4\text{O}_{9-y}$  and  $\gamma$ - $\text{U}_4\text{O}_{9-y}$  [22,26]. The space group of  $\text{U}_4\text{O}_{9-y}$  is I-43d, in which the uranium ions are in a  $4 \times 4 \times 4$  conventional  $\text{UO}_2$  f.c.c. arrangement, while the excess oxygen ions are in cuboctahedron arrangement. Figure 2-6 shows the structure of  $\beta$ - $\text{U}_4\text{O}_{9-y}$ , as proposed by Cooper and Willis [22].

a)



b)



c)

Atom	Site	$x$	$y$	$z$	Atomic groups
U1	16(c)	0	0	0	
U2	24(d)	$1/4+a_1$	0	$1/4$	Octahedron 72 atoms
U3	48(e)	$1/8$	$1/8-a_1$	$1/4$	
U4	24(d)	$a_2$	0	$1/4$	Octahedron 72 atoms
U5	48(e)	$7/8$	0	$1/8-a_2$	
U6	48(e)	$-a_3$	$1/8-a_3$	$3/8-a_3$	Tetrahedron 48 atoms
U7	48(e)	$-a_4$	$1/8-a_4$	$1/8+a_4$	Tetrahedron 48 atoms
O1	48(e)	$7/8+b_1$	$b_1$	$1/4+b_2$	Skewed cuboctahedron 144 atoms
O2	48(e)	$7/8+b_1$	$b_2$	$1/4+b_1$	
O3	48(e)	$7/8+b_2$	$b_1$	$1/4+b_1$	
O4	16(c)	$1/16$	$1/16$	$1/16$	
O5	16(c)	$3/16$	$3/16$	$3/16$	
O6	48(e)	$1/16-b_3$	$3/16-b_3$	$3/16+b_3$	
O7	48(e)	$1/16+b_4$	$1/16+b_5$	$3/16-b_5$	Hexatetrahedron 288 atoms
O8	48(e)	$15/16+b_5$	$1/16+b_5$	$1/16-b_4$	
O9	48(e)	$15/16-b_6$	$1/16-b_6$	$7/16+b_4$	
O10	48(e)	$15/16+b_5$	$3/16+b_4$	$3/16-b_5$	
O11	48(e)	$15/16-b_6$	$3/16+b_4$	$5/16-b_6$	
O12	48(e)	$1/16+b_4$	$1/16-b_6$	$5/16-b_6$	
O13	48(e)	$15/16-b_7$	$3/16-b_7$	$7/16+b_7$	
Empty	12(b)	$7/8$	0	$1/4$	Cluster centre
O15	48(e)	$7/8+b_8$	$b_8$	$1/4+b_8$	Tetrahedron 12 atoms

Figure 2-6 The crystalline structure of  $\beta$ - $U_4O_{9-y}$  proposed by Cooper and Willis [22]. The grey balls represent uranium atoms, the blue balls stand for regular oxygen atoms and the green balls signify the cuboctahedron arrangement of oxygen ions. a) shows the whole lattice arrangement, b) is the cuboctahedron arrangement with a central oxygen and c) is the corresponding atomic coordinates with  $a_1$ - $a_4$  and  $b_1$ - $b_8$  positional parameters.

### $U_3O_8$

$U_3O_8$  exhibits three phases ( $\alpha$ ,  $\beta$ ,  $\gamma$ )-  $U_3O_8$ .  $\alpha$ -  $U_3O_8$  is within the space group of  $C2mm$ ,  $\beta$  -  $U_3O_8$  is  $Cmcm$  and  $\gamma$ -  $U_3O_8$  is  $P21/m$  [54].  $U_3O_8$  is important as it is one of the thermodynamically and kinetically stable compounds of the U-O system.

## 2.3. State-of-the-art research

In the first phase of this research, the clustering behaviour of oxygen interstitials and holes were addressed by empirical potential (EP) based atomic scale simulations. Recent theoretical works on defect chemistry include, for example, Murphy et al., who evaluated point defect concentrations and non-stoichiometry in thorium. They used DFT to predict the defect formation energies [55]. A similar approach was adopted for uranium oxide by Cooper et al. [56]. Soulié et al., and Bruneval et al. extended the  $\text{UO}_2$  study by adding oxygen defect clusters in their model [57,58]. Even though their results qualitatively provide a comparable defect concentration trend, the quantitative understanding still suffers from inconsistencies. This is mainly because of the various approximations used for the descriptions of the strong correlation between uranium  $f$  electrons, which in turn affects the defect formation energies. Unlike the above-mentioned studies, this thesis investigated the oxygen clusters up to di-interstitial by means of EP simulations in expectation of a qualitative agreement between DFT and EP. Motivated by the positive results, a qualitative validation against measurements of stoichiometry dependence on oxygen partial pressure and temperature was performed.

The binary oxides based on  $\text{UO}_2$  fuel matrix ( $\text{U}_{1-y}\text{Pu}_y\text{O}_2$ ,  $\text{U}_{1-y}\text{Am}_y\text{O}_2$ ,  $\text{U}_{1-y}\text{Np}_y\text{O}_2$ ) have been treated extensively in recent studies, concluding a linear relationship between lattice parameter and composition (Vegard's law) [59–64]. Compared to that, the availability of data on their complex ternary and quaternary oxide mixtures are, however, very limited. Therefore, in the second phase of this study, EP methods have been extended to investigate the complex  $\text{U}_{1-y-y'}\text{Pu}_y\text{Am}_{y'}\text{O}_2$  and  $\text{U}_{1-y-y'-y''}\text{Pu}_y\text{Am}_{y'}\text{Np}_{y''}\text{O}_2$  systems' lattice parameters as a function of atomic fraction.

### Research Design

- An atomic scale analysis of defect clustering and predictions of their concentrations in  $\text{UO}_{2+x}$

The simulations were carried out for the clusters of the form of  $\{n\text{O}_i'' : p\text{U}_j^\bullet\}^{(2n-p)'} -$  with  $n$  being the number of oxygen interstitials and  $p$  being the number of holes that would be bound to the defect. The exploration of the arrangement of holes around a single oxygen interstitial defect, or an oxygen interstitials cluster, is a tedious and difficult task, given that the number

of cases to be addressed increases in a combinatorial way with the number of holes considered. In order to optimize the calculation time, several methods were tested:

- The brute force approach was used as a reference, where all possible combinations are relaxed and compared in terms of energy.
- A Monte-Carlo approach was then tested, where  $U^{5+}$  are only displaced when the energy gain after the displacement obeys an acceptance (Metropolis) criterion.
- A rigid lattice approach was used to address the energy gain issue, evoked previously when permuting  $U^{5+}$  and  $U^{4+}$  ions.

The methods described above were used to address the most stable defect configurations in  $UO_2$  in a reasonable time frame. Once the most stable defect cluster configurations were obtained, they were further analysed with respect to their binding energies. Two widely used methods, namely the Mott-Littleton and the supercell method, were applied to address the defect energies in an ionic crystal. Further, these energies were complemented with a Point Defect Model (PDM), in which the defect concentrations were derived from the reaction energies. A validation of the methodology and the results was then conducted based on deviation from stoichiometry in  $UO_{2+x}$  (see Chapter 5).

- Lattice parameter of Am, Np bearing MOX fuel: an empirical potential study.

The lattice parameter of the simple oxides  $AnO_2$  ( $An= U, Pu, Am$  or  $Np$ ) was calculated as a pre-validation. In a second step, binary mixture oxides were modelled for various concentrations of MAs in the host  $UO_2$  matrix. The lattice configuration was predicted via a systematic optimization method called rigid lattice method. From that configuration, relaxed system energies and lattice parameters were investigated as a function of composition. Then, the assessment was extended to complex  $U_{1-y-y'}Pu_yAm_{y'}O_2$  and  $U_{1-y-y'-y''}Pu_yAm_{y'}Np_{y''}O_2$  systems. Finally, the results of this study were compared to the available experimental data and also to the standard ionic radii model (see Chapter 6).

### 3. Techniques

Atomistic simulations allowed for the discovery of a diverse range of solid-state material properties, such as equilibrium and transport properties. For empirical potential (EP) simulations, the overall assumption is the physical interpretation of atomic interactions, which is the basic input of any simulation. In this respect, this research does not only focus on the development of computational and numerical techniques, but also on the deep understanding of the nature of these EPs.

Two techniques are used in EP studies, namely either static simulations, generally aiming at finding stable or meta-stable configurations or time-dependent dynamic simulations where the time-evaluation of the system is tracked by integrating Newton's law of motion. The latter technique, coupled to thermodynamics, enables to derive important thermo-physical parameters of the material under investigation. However, the reliability of EP calculations is still limited by the quality of interatomic potentials. Therefore, the validation is of high importance.

In the following, methods and techniques used to perform EP based atomic scale simulations are described in detail. The fundamental knowledge on the non-stoichiometric  $\text{UO}_2$  and MA based MOX fuel technology is discussed and extended. Throughout the study atomic scale simulations were performed with the Large-scale Atomic/Molecular Massively Parallel Simulator (LAMMPS) [65] and the General Utility Lattice Program (GULP) [66] software, while the defect chemistry solver was developed based on the Newton-Raphson optimization algorithm [67].

LAMMPS is an open-source code which is written in C++ and originally developed at Sandia National Labs [65]. LAMMPS can evaluate the particles up to millions or billions in liquid, solid and gaseous state. In addition, it can simulate atomic, polymeric, biological, solid-state (metals, ceramics), granular, coarse-grained systems using the interatomic potentials and boundary conditions [65].

GULP is originally developed at Curtin university to fit interatomic potentials to both energy surfaces and empirical data, which is written in FORTRAN [66]. The earliest versions focus on solids, clusters, and embedded defects, while the current version can model surfaces, interfaces, and polymers etc., [66].

### 3.1. Empirical potentials in ionic crystal

In the EP based atomic scale calculations it is important to accurately define interatomic forces in order to reproduce material properties. There are two types of interatomic potentials being used in fuel material calculations, namely core-shell and rigid ion model. The former considers the polarization effects by describing atoms as a core, which are connected to the shell by an imaginary spring. In the latter model, each atom is described as a rigid point object. Throughout the study a rigid ion description was used for the calculations.

A typical form of the potential energy between two ions  $i$  and  $j$  at a distance apart  $r_{ij}$  is expressed by Eq. (3-1).

$$V(r_{ij}) = V(r_{ij})_{\text{long-range}} + V(r_{ij})_{\text{short-range}} \quad (3-1)$$

and

$$V(r_{ij})_{\text{long-range}} = \frac{(\xi e)^2 Z_i Z_j}{4\pi\epsilon_0 r_{ij}} \quad (3-2)$$

The  $V(r_{ij})_{\text{long-range}}$  term stands for the electrostatic interaction between point charges with  $\epsilon_0$ , the vacuum permittivity.  $\xi$  is the degree of covalence, or ionicity with ( $0 < \xi \leq 1$ ) and  $e$  is the magnitude of charge. For  $\text{UO}_2$ , one considers full ionicity:  $Z(\text{U}^{4+}) = +4$  and  $Z(\text{O}^{2-}) = -2$ . Although the equation as shown by Eq. (3-2) seems quite simple, the calculation of the system coulomb energy under periodic boundary conditions is challenging. In this study, Ewald summation techniques were used to handle long-range electrostatic interactions in three dimensions [68].

The second term of Eq. (3-1)  $V(r_{ij})_{\text{short-range}}$  expresses the short-range interactions. The Buckingham form is widely used to address such interactions in oxide materials, which is shown in Eq. (3-3) [69].

$$V(r_{ij})_{\text{short-range}} = A \exp\left(-\frac{r_{ij}}{\rho}\right) - \frac{C}{r_{ij}^6} \quad (3-3)$$

Where A,  $\rho$  and C are potential parameters. The exponential term ( $e^{-r}$ ) expresses the repulsion of overlapping electronic shells and the inverse power function ( $-1/r^6$ ) expresses the van der Waals attraction. Other types of potentials used in ionic crystals are the following:

Buckingham-4 ranges potential in Eq. (3-4) is proposed to overcome the non-physical attraction of Buckingham potential at very short interatomic distances [70–74].

$$V(r_{ij})_{\text{short-range}} = \begin{cases} A \exp\left(-\frac{r_{ij}}{\rho}\right), & \text{if } r_{ij} \leq r_1 \\ 5^{\text{th}} \text{ order polynomial,} & \text{if } r_1 < r_{ij} \leq r_{\min} \\ 3^{\text{rd}} \text{ order polynomial,} & \text{if } r_{\min} < r_{ij} \leq r_2 \\ -\frac{C}{r_{ij}^6}, & \text{if } r_{ij} > r_2 \end{cases} \quad (3-4)$$

Born-Mayer-Huggins (BMH) potential function in Eq. (3-5) is commonly used to describe the ionic interactions in oxides. The  $a_i$  or  $a_j$ ,  $b_i$  or  $b_j$ ,  $c_i$  or  $c_j$  and  $f_0$  appearing in the interatomic potential are the parameters [32,37,38].

$$V(r_{ij})_{\text{short-range}} = f_0(b_i + b_j) \exp\left(\frac{a_i + a_j - r_{ij}}{b_i + b_j}\right) - \frac{c_i c_j}{r_{ij}^6} \quad (3-5)$$

Morse potential in Eq. (3-6) represents the covalent bonding of the cation-anion pairs. In the morse function model  $D_0$ ,  $\gamma_{ij}$  and  $r_{ij}^*$  are potential coefficients [29,75].

$$V(r_{ij})_{\text{short-range}} = D_0 \left[ \exp\left(-2\gamma_{ij}(r_{ij} - r_{ij}^*)\right) - 2 \exp\left(-\gamma_{ij}(r_{ij} - r_{ij}^*)\right) \right] \quad (3-6)$$

The adopted expression Embedded atom method (EAM) potential in Eq. (3-7) for the ionic crystal with the potential energy ( $E_i$ ) of the atom i surrounded by atom j is in the following form [30,31].



$$E_i = \frac{1}{2} \sum_j V_{\alpha\beta}(r_{ij}) - G_\alpha \sqrt{\left( \sum_j \sigma_\beta(r_{ij}) \right)} \quad (3-7)$$

Where  $\alpha$  and  $\beta$  are the elements of atoms  $i$  and  $j$ . The first term  $V_{\alpha\beta}(r_{ij})$  simulates the pairwise interactions that includes both short  $V_{\alpha\beta}(r_{ij})_{\text{short-range}}$  –a combination of Buckingham in Eq. (3-3) and Morse potentials in Eq. (3-6) and a long range  $V_{\alpha\beta}(r_{ij})_{\text{long-range}}$  electrostatic descriptions. The second term in Eq. (3-7) expresses the many-body dependence on the surrounding ions. The term includes the summation of set of pairwise functions ( $\sigma_\beta$ ) and the embedding energy  $G_\alpha$  parameters.

There are also other empirical potential descriptions for oxide systems, such as tabulated potentials, charge optimized many-body (COMB) potentials, second-moment tight-binding variable-charge (SMTB-Q) interatomic potentials etc., [76–79]. In the present work, the widely used Yakub (Buckingham + Morse) [29], CRG (EAM potential) [30,31] and Arima (BMH) potentials were selected [32,37,38].

### 3.2. Static calculations

Static calculations are performed for two main reasons, namely, to compute the lattice energy (or cohesive energy) of a perfect crystal, and the energy to create a defect within that crystal. The defect energy calculation was the main focus due to its fundamental importance to obtain deeper knowledge on the thermodynamic and transport properties of nuclear fuel. The static energy calculations were performed based on a concept of energy minimization or relaxation techniques.

#### The concept of energy minimization

Energy minimization is a widely used iterative technique in atomic scale calculations [80]. In this approach, the energy function  $E(r_i)$  is minimized with respect to atomic coordinates  $r_i$  of

an N atoms system. In general, the minimum of the function  $E(r_i)$  must be satisfied, as shown in Eq. (3-8).

$$\frac{\partial E_{r_i}}{\partial r_i} = 0 \text{ and } \frac{\partial^2 E_{r_i}}{\partial r_i^2} > 0 \quad (3-8)$$

Energy minimization starts with an initial atomic configuration, which is, in this case, a crystal structure and its corresponding edge distances. The straightforward application of consecutive iterative steps would probably make the system locate at the nearest local minimum. The main issue is that the energy minimization can never be guaranteed to find the global minimum. Especially for the defective systems different initial configurations must be sampled to ensure true minima to be obtained. Figure 3-1 shows the 2D analogous of energy landscape as a function of conformation space.

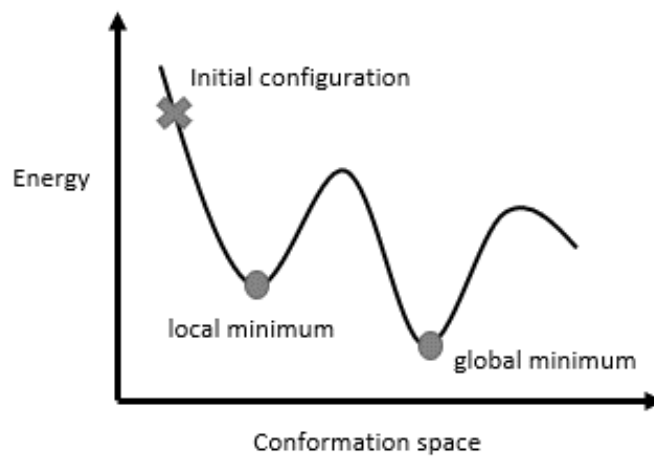


Figure 3-1 The energy landscape as a function of conformation space.

Although a variety of numerical algorithms can be used to perform energy minimization in atomic scale simulations, the present work mainly applied the conjugate gradient and Newton Raphson for minimization [65,66]. The minimizations were performed under constant volume or constant pressure conditions (i.e., with volume relaxation as well).

### Defect energy calculations:

Defect energy calculations were performed using the LAMMPS and GULP software because of their ability to use different methods, namely in this study the Mott-Littleton and supercell method [65,66]. To maintain coherence, both codes used the same interatomic potentials to perform the system defect energy calculations.

- The Mott-Littleton method divides the space around the defect into three regions as shown in Figure 3-2. In region I, atoms are fully relaxed, while in region IIa, only harmonic relaxation due to the defect charge is assumed. In region IIb, an infinite purely dielectric medium is assumed [66]. In this work, radii of 1.4 nm for region I and 2.8 nm for region IIa were used.
- In the supercell method a neutral system needs to be recovered, by adding a uniform background charge to the system. This background charge does not affect interatomic forces and simply results into an additional term to the system total energy. In LAMMPS [65], the system energy is not corrected for background charge; at post-processing, defect energies are then corrected for the charge's Madelung energy to the infinite dilution limit according to the potential predictions:  $f^\infty = f^L + \frac{q^2\alpha}{2\epsilon L}$ , where  $f^\infty$  and  $f^L$  are the formation energies of the defect at infinite dilution and under periodic boundary conditions with total system size L (=0.544 x 4 nm after relaxation of the pristine system), q is the total charge on the solid,  $\alpha$  (=2.84) is the cubic system Madelung constant and  $\epsilon$  (=3.28, i.e., for Yakub potential [29]) is the static dielectric constant.

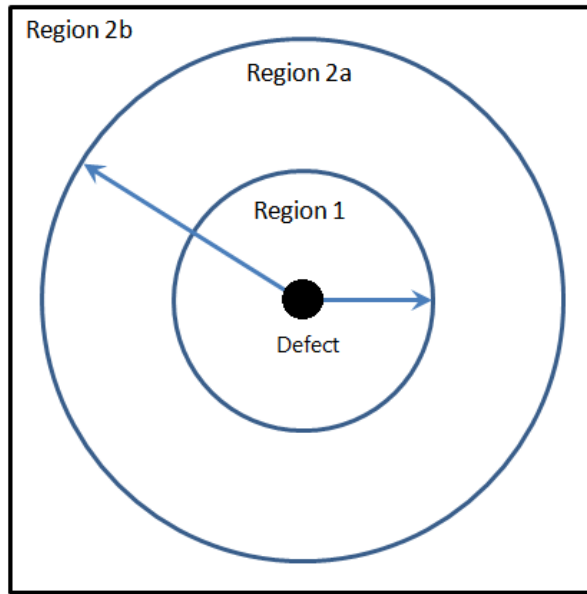


Figure 3-2 Mott-Littleton method: division of space into three regions.

### 3.3. Molecular dynamics simulations

Molecular dynamic (MD) simulations reproduce the time evolution of the collective behaviour of  $N$  particles by integrating Newton's law of motion within specified boundary conditions [81]. For an  $N$  particle system with  $U$  being the potential energy and  $m$  the particle mass, the equations are

$$m \frac{d^2 r_i}{dt^2} = -\nabla U(r^{3N}), i = 1, 2, \dots, N \quad (3-9)$$

The exact solution of this  $N$ -body problem is not possible. Therefore, in MD simulations the main focus is on the numerical solutions, given that the force calculations are the most computationally demanding. A typical flowchart for an MD code would then be like,

- i. Assign initial particle positions and velocities
- ii. Calculate the total force on each particle
- iii. Update particle positions and velocities according to Eq. (3-9)
- iv. Compute properties (energy, temperature, pressure etc.)
- v. Repeat from (ii) until the system reaches the desired conditions.

### 3.4. Monte Carlo simulations

The Monte Carlo particle swapping method was used to investigate first the anion-hole cluster formation in  $\text{UO}_{2+x}$ , and second to find the structure of the solid solution of  $\text{AnO}_2$  ( $\text{An} = \text{U}, \text{Pu}, \text{Am}$  or  $\text{Np}$ ) systems. The Monte Carlo swap functionality, which is implemented in LAMMPS, was used [65]. The method can be summarised as follows [81]:

- i. The particles of interest were initially randomly distributed within the simulation system.
- ii. The Monte Carlo swap functionality was used, allowing only for one swap in each run step.
- iii. For each run step, the energy difference between two states right after the swap is calculated, expressed as  $\Delta E = E_{n+1} - E_n$  where  $n$  is the configuration.
- iv. The swap is accepted or rejected based on the Metropolis acceptance criterion ( $p_{\text{acc}}$ ) (see Eq. 3-10 and Figure 3-3).
- v. Iteration of steps ii – iv until the system reaches convergence.

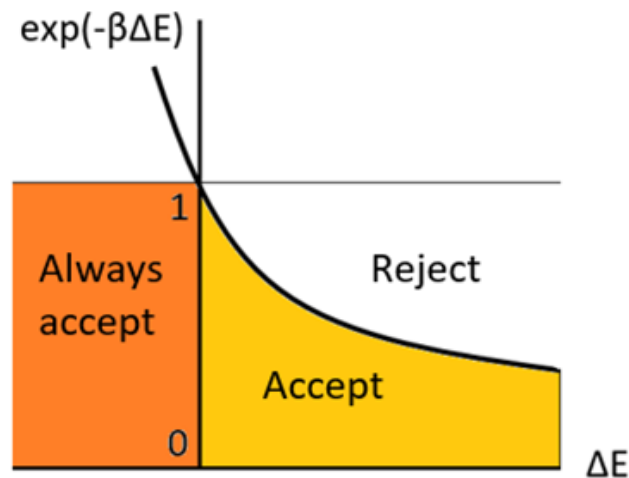


Figure 3-3 Metropolis criterion of acceptance.

$$p_{\text{acc}} = \begin{cases} 1, & \Delta E \leq 0 \\ \exp(-\beta\Delta E), & \Delta E > 0 \end{cases} \quad (3-10)$$

where  $\beta$  is inverse temperature or  $\frac{1}{k_B T}$ ,  $T$  is temperature in Kelvin and  $k_B$  is Boltzmann constant in  $\text{eV} \cdot \text{K}^{-1}$ .

### 3.5. Defect chemistry

Cluster defect energies are not, as such, sufficient to know which defect will dominate, as the configurational entropy, and possibly the vibrational entropy, should also be taken into account. The equilibrium defect concentrations may be expressed as a point defect model, which expresses the equilibrium of the defect reactions at play. In  $\text{UO}_{2+x}$ , the simplest model needs to account for:

- Small polaron equilibrium, i.e., the dissociation of  $2\text{U}^{4+}$  into a  $\text{U}^{3+} - \text{U}^{5+}$  pair (electron-hole pair)
- Oxygen Frenkel equilibrium, i.e., the spontaneous formation of an oxygen interstitial – vacancy pair
- An oxidation reaction of the crystal with an  $\text{O}_2$  molecule
- Electroneutrality of the system, considering the presence of all defect species.

Although conceptually simple, this system was proven not to be sufficient to reproduce the complex behavior of  $\text{UO}_{2+x}$ . It has been evidenced that a better picture is provided if the clustering of oxygen interstitials is accounted for in the model [47,50]. Therefore, oxygen interstitial clusters with varying effective charges are introduced in the model. Changes in the defect cluster charge were modelled in this work through the presence of localized holes on the uranium site. Assuming that a single individual oxygen interstitial cluster species dominates, in the form of  $\{n\text{O}_i'' : p\text{U}_U^\bullet\}^{(2n-p)'} -$  with  $n$ , the number of oxygen interstitials and  $p$ , the number of holes in the cluster.

#### Point defect model:

A point defect model (PDM) expresses interactions (or reactions) between defects in a similar way as one treats chemical reaction equilibria. It links, for each defect reaction, the concentrations at equilibrium of species involved. Although virtually any defect and defect reaction could be considered, the point defect model will solely provide a good representation of a material if the dominant defects are included in the picture. In uranium dioxide, it is commonly accepted that the dominant defects relate to electronic and oxygen disorder [47,82]. The simplest description of  $\text{UO}_2$ , close to stoichiometry, expresses the polaron (electron-hole

pair creation) and the oxygen Frenkel (oxygen vacancy – interstitial pair) equilibria. Using Kröger-Vink notations [83], these reactions can be expressed, respectively as



A relation between defect concentrations may then be expressed according to mass action law which involves the change in free energy of the system  $\Delta f$

$$K_{\text{D}} = \frac{[U_{\text{U}}^{\prime}][U_{\text{U}}^{\bullet}]}{[U_{\text{U}}^{\times}]^2} = \exp\left(-\frac{\Delta f^{\text{D}}}{k_{\text{B}}T}\right) \quad (3-13)$$

$$K_{\text{F}} = \frac{[O_{\text{i}}^{\prime\prime}][v_{\text{o}}^{\bullet\bullet}]}{[O_{\text{o}}^{\times}][v_{\text{i}}^{\times}]} = \exp\left(-\frac{\Delta f^{\text{F}}}{k_{\text{B}}T}\right) \quad (3-14)$$

Where  $[U_{\text{U}}^{\bullet}]$  and  $[U_{\text{U}}^{\prime}]$  are the concentration of holes and electrons assumed in the valence and conduction band, respectively. The  $[O_{\text{i}}^{\prime\prime}]$  represents the oxygen interstitial concentration while  $[v_{\text{o}}^{\bullet\bullet}]$  is the vacancy oxygen concentration. Above the simple system contains seven unknowns and needs to be closed by other relations that express, for example, conservation of the site occupancy and of the system charge neutrality. In the infinite dilution limit, one may approximate regular atom concentrations by their value in a perfect crystal  $[U_{\text{U}}^{\times}] \approx [v_{\text{i}}^{\times}] \approx \frac{1}{2}[O_{\text{o}}^{\times}] \approx 1$  otherwise the relative contribution of each defect to uranium, oxygen and interstitial lattices should be summed up. The charge neutrality condition for any kind of defect (i) with a concentration  $C_i$  and net charge  $q_i$  must be maintained

$$\sum_{\text{i}} q_i C_i = 0 \quad (3-15)$$

One last relation is required, which links the system to the constraints imposed by the environment. For  $\text{UO}_2$ , we consider that the oxidation reaction from the atmosphere surrounding the system dominates. The point defect reaction is expressed as



Or, in mass action law form

$$K_o = \frac{[O_i''] [U_U^\bullet]^2}{[U_U^x]^2 [v_i^x] \sqrt{p_{O_2}}} = \exp\left(-\frac{\Delta f^0}{k_B T}\right) \quad (3-17)$$

Where  $p_{O_2}$  stands for the surrounding oxygen partial pressure. The deviation from stoichiometry  $x$ , in a regime dominated by isolated oxygen interstitials and holes, follows  $\propto p_{O_2}^{1/6}$ . The simple description of defects in  $\text{UO}_2$ , however, does not correspond to what is experimentally observed at larger deviation from stoichiometry: it has been evidenced that a better picture is provided if the clustering of oxygen interstitials is accounted in the model, as the observed relation rather obeys  $x \propto p_{O_2}^{1/2}$  [44,46,84]. One therefore introduces oxygen interstitial clusters with varying effective charges in the point defect model. Changes in the defect cluster charge were modelled in this work through the presence of localised holes on the uranium site. Assuming that a single individual oxygen interstitial cluster species dominates, in the form of  $\{nO_i'' : pU_U^\bullet\}^{(2n-p) \cdot}$  – with  $n$ , the number of oxygen interstitials and  $p$ , the number of holes in the cluster – the corresponding power dependency for the charge neutral system could be generalised as  $x \propto p_{O_2}^m$ , with the exponent  $m = \frac{n}{2(2n-p+1)}$ . For example, in the case of isolated  $O_i''$  ( $n=1, p=0$ ) one comes back to the first case and  $m = \frac{1}{6}$ ; this situation is expected to dominate close to perfect stoichiometry when clustering is not favourable for configurational entropy reasons. Experimentally, one observes a domain where the power dependency of  $x$  goes as  $p_{O_2}^{1/2}$ ; this observation would be compatible with two clusters of limited size:  $\{O_i'' : 2U_U^\bullet\}''$  ( $n=1, p=2$ ) or  $\{2O_i'' : 3U_U^\bullet\}'$  ( $n=2, p=3$ ). A distinction between both types cannot be



gained from stoichiometry measurements, but could be obtained from electrical conductivity data, as the second defect cluster type should be, for charge neutrality reasons, compensated by isolated holes, which are mobile defect species. Several authors have proposed to consider singly charged di-interstitial clusters as the dominant defect at moderate departures from stoichiometry [44,46,84]. This leads to

$$nO_i'' + p U_U^\bullet \rightleftharpoons \{nO_i'' : pU_U^\bullet\}^{(2n-p)'} \quad (3-18)$$

$$K_{\text{Cls.}} = \frac{[\{nO_i'' : pU_U^\bullet\}^{(2n-p)'}]}{[O_i'']^n [U_U^\bullet]^p} = \exp\left(-\frac{\Delta f^{\text{Cls.}}}{k_B T}\right) \quad (3-19)$$

If one assumes that next to isolated point defects, only Willis clusters with charge -1 are formed, the site balances may be expressed as:

$$[U_U^\times] + [U_U^\bullet] + [U_U'] = 1 \quad (3-20)$$

$$[O_o^\times] + [v_o^{\bullet\bullet}] = 2 \quad (3-21)$$

$$[v_i^\times] + [O_i''] + (2 + a)[\{2O_i'' : 3U_U^\bullet\}'] = 1 \quad (3-22)$$

The parameter  $a$  is used here for  $\{2O_i'' : 3U_U^\bullet\}'$  or Willis clusters to restrict access to neighbour interstitial sites. Using  $a = 6$  also enables to reproduce  $UO_{2+x}$  saturation at  $x = 0.25$ , i.e., a stoichiometry corresponding to  $U_4O_9$ . The PDM system of equations is solved with a Newton-Raphson iterative technique, ensuring numerical convergence is obtained. The deviation from stoichiometry is then evaluated from the various defect concentrations, considering that defects on the uranium sub-lattice play a negligible role

$$x = |\sum n[\{nO_i'' : pU_U^\bullet\}^{(2n-p)'}] - [v_o^{\bullet\bullet}]| \quad (3-23)$$

### Numerical solution scheme: Newton-Raphson method

The system of equations (3-13), (3-14), (3-15), (3-19), (3-20), (3-21) and (3-22) is solved with a Newton-Raphson iterative technique [67]. The point defect equations are in the functional form of

$$\begin{aligned} f_1(x_1, x_2, \dots, x_N) &= C_1 \\ f_2(x_1, x_2, \dots, x_N) &= C_2 \\ &\vdots \\ f_N(x_1, x_2, \dots, x_N) &= C_N \end{aligned} \quad (3-24)$$

Where  $x_i$  and  $C_i$  are the point defect concentrations and arbitrary constants, respectively. When above the N functional relation rearranged as  $F(x)=0$  as such

$$F_i = f_i(x_1, x_2, \dots, x_N) - C_i = 0 \text{ for } i=1, 2, \dots, N \quad (3-25)$$

Where  $F = [F_1 \ F_2 \ \dots \ F_N]^T$  and  $x = [x_1 \ x_2 \ \dots \ x_N]^T$ .  $F(x)$  and  $x \in \mathbb{R}^N$  being a vector,  $F(x)$  can be expanded in Taylor series in the neighbourhood of  $x$ .  $F_i(x + \delta x) = F_i(x) + \sum_{j=1}^N \frac{\partial F_i}{\partial x_j} \delta x_j + hot$ , where “hot” is higher order terms. In the matrix form:

$$F(x + \delta x) = F(x) + J \cdot \delta x + hot, \text{ where } J \text{ is Jacobian matrix} \quad (3-26)$$

By neglecting the hot and by setting  $F(x + \delta x) = 0$ . To linearize the set of equations, the equation below is solved until the system converges.

$$-F(x) = J \cdot \delta x, \text{ where } \delta x = x_{new} - x_{old} \quad (3-27)$$

## 4. Proposed approach: configurational space exploration

Configurational space exploration was performed to investigate first the anion cluster formation in  $\text{UO}_{2+x}$  and second to find the structure of the solid solution of  $\text{AnO}_2$  ( $\text{An} = \text{U}, \text{Pu}, \text{Am}$  or  $\text{Np}$ ) systems. Exploration of such arrangements are a demanding task, given that the number of cases increases in a combinatorial way for the composition considered. For example:

- The number of the arrangement of holes around a single oxygen interstitial defect, or an oxygen interstitial cluster is  $\frac{N!}{(N-n)! \times n!}$ , with  $N$ , the number of accessible sites (256) for  $4 \times 4 \times 4$  unit-cell, and  $n$ , the number of  $\text{U}^{5+}$  inserted in the system.
- The number of lattice configurations of a solid solution of  $\text{AnO}_2$  ( $\text{An} = \text{U}, \text{Pu}, \text{Am}$  or  $\text{Np}$ ), in case of a binary oxide system  $\text{U}_{1-y}\text{Pu}_y\text{O}_2$ , is expressed as  $[\frac{N!}{(N-n)! \times n!}]$ , with  $N$  being the number of accessible sites (256) for  $4 \times 4 \times 4$  unit-cell, and  $n = (y \times 256)$ , the number of Pu replaced by the U lattice position. Similarly, if the system of interest is  $\text{U}_{1-y}\text{Pu}_y\text{Am}_m\text{O}_2$ , the number of possible combinations becomes  $[\frac{N!}{(N-n)! \times n!}][\frac{(N-n)!}{(N-n-m)! \times m!}]$  with  $m = (y' \times 256)$ , the number of Am atoms distributed in the simulation box etc.

To optimize the calculation time, several methods were tested.

### 4.1. Monte Carlo (MC) – Molecular Dynamics (MD) method

A Monte-Carlo approach was tested to investigate oxygen cluster configurations in  $\text{UO}_{2+x}$ , where  $\text{U}^{5+}$  are only displaced when the energy gain after the displacement obeys an acceptance (Metropolis) criterion. The major issue with this approach is that the point of departure usually is a relaxed configuration, where the permutation of an  $\text{U}^{5+}$  and an  $\text{U}^{4+}$  ion often results in a positive energy gain. Although well-thought criteria enable to progressively converge towards lower energy configurations, convergence to the energy minimum is slow and not guaranteed. Figure 4-1 shows Monte Carlo-Molecular dynamics (MC-MD) method [65] carried out at a swap temperature of 2000 K for a system of  $\{\text{O}_i'' : 2\text{U}_i^{\bullet}\}^{\times}$  using Yakub potential [29]. The method was validated with a conjugate gradient method. Figure 4-2 depicts the defective system energy calculated with MC-MD method compared to the results obtained by using a conjugate gradient method for a system of  $\{\text{O}_i'' : 2\text{U}_i^{\bullet}\}^{\times}$  using Yakub potential [29].

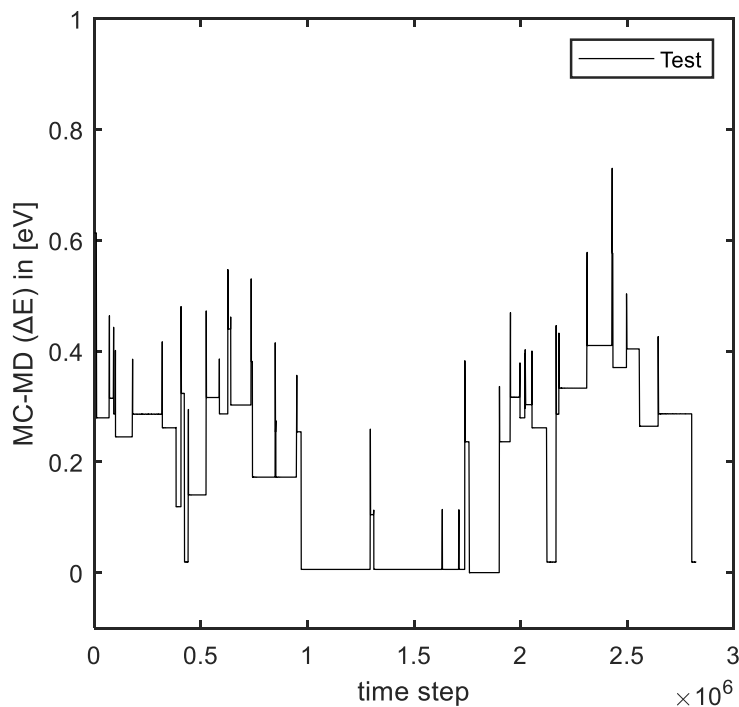


Figure 4-1 MC-MD method carried out at 2000 K swap temperature for a system of  $\{O_1'' : 2U_1^*\}^x$  using Yakub potential [29].

The MC-MD method could also be used to evaluate the lattice configuration of a solid solution of  $AnO_2$  ( $An = U, Pu, Am$  or  $Np$ ) system where  $An^{4+}$  are only displaced when the energy gain after the displacement obeys an acceptance (Metropolis) criterion [65,81]. In that case, the  $An^{4+}$  permutation could never result in a positive energy gain. However, the selection of the temperature of the thermodynamic ensemble would probably be challenging, as the atomic positions affect the acceptance (Metropolis) criterion of  $An^{4+}$  ions. Figure 2-3 depicts the calculated radial distribution function  $g(r)$  of  $An^{4+}-An^{4+}$  at 300 K and 3000 K. Although the mean value of  $An^{4+}-An^{4+}$  distance is the same for different temperatures, selecting different system temperatures will lead to the prediction of different lattice configurations of mixed actinide solid solutions.

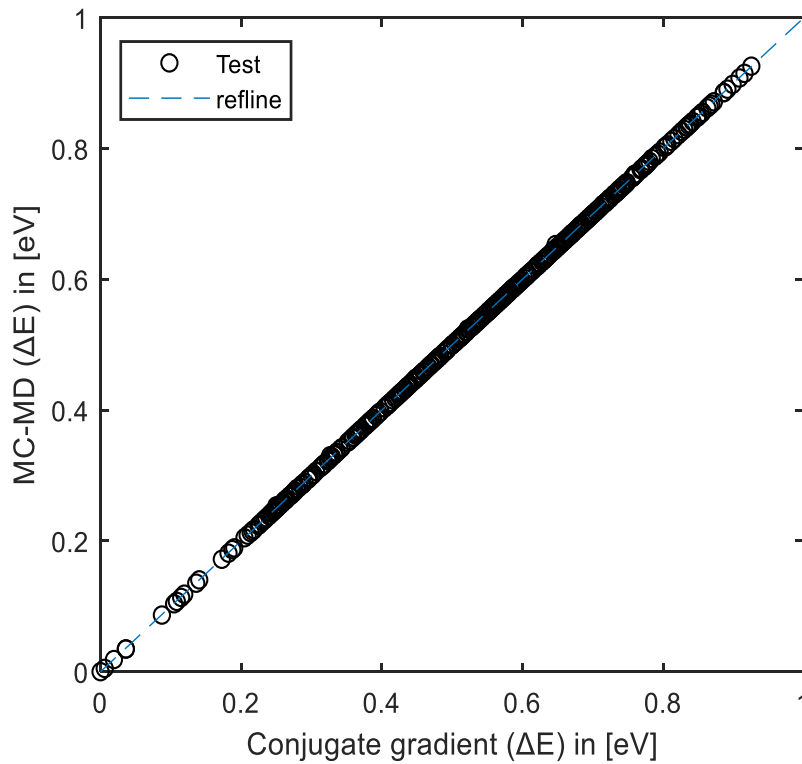


Figure 4-2 The energy comparison with MC-MD method and conjugate gradient method for a system of  $\{O_i'' : 2U_U^*\}^x$  using Yakub potential [29].

## 4.2.Rigid lattice approach

A rigid lattice approach considers the non-relaxed and the relaxed configuration maps to be qualitatively similar. The search for the optimal configuration is then performed in the non-relaxed scheme and avoids the systematic relaxation stage, which would require between 100 and 1000 calculation steps. The relaxed configuration energy is only calculated once, for the optimal configuration. Although the method could be used in a brute-force scheme, the interest also lies in coupling it to a Monte-Carlo algorithm. A typical rigid lattice method coupled with Monte Carlo metropolis algorithm is shown in Figure 4-3. The method is applied to the following two systems [65]:

- With regard to oxygen cluster configurations in  $\text{UO}_{2+x}$ , the fact that non-relaxed configurations are used eliminates the energy gain issue evoked previously when permuting an  $\text{U}^{5+}$  and an  $\text{U}^{4+}$  ions. Figure 4-4 depicts the configuration maps for a system of  $\{\text{O}_i'' : 2\text{U}_j^*\}^x$  using Yakub potential [29] a) conjugate gradient map b) rigid lattice map.

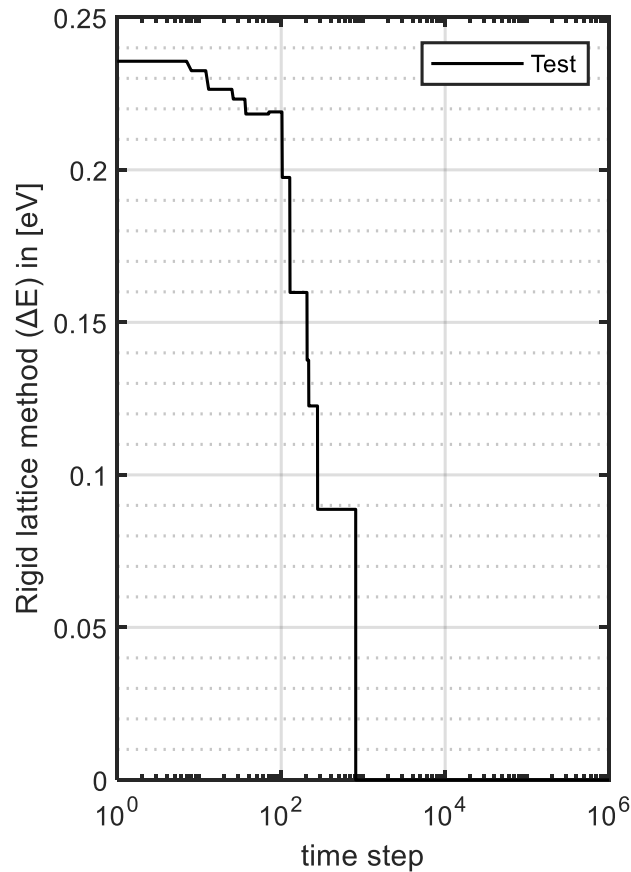


Figure 4-3 Rigid lattice method coupled with Monte Carlo metropolis algorithm for a system of  $\{\text{O}_i'' : 2\text{U}_j^*\}^x$  using Yakub potential [29].

- With respect to the lattice configuration of a solid solution of an  $\text{AnO}_2$  ( $\text{An} = \text{U}, \text{Pu}, \text{Am}$  or  $\text{Np}$ ) system, the fact that rigid lattice configurations are used eliminates the atomic vibration issue evoked previously for the Monte Carlo – Molecular dynamics system [65].

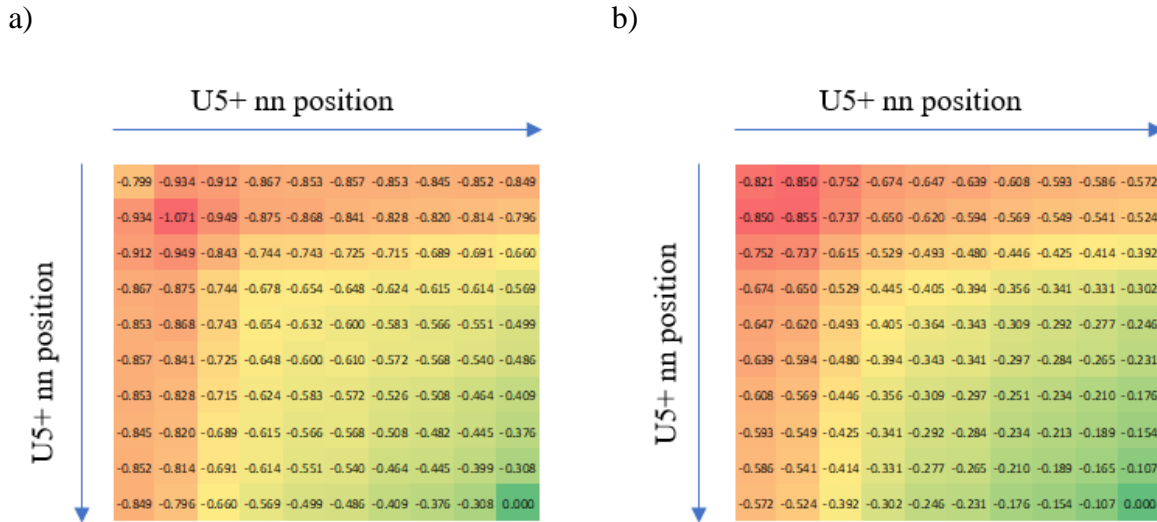


Figure 4-4 The configuration maps for a system of  $\{O_i^{\bullet\bullet}; 2U_U^{\bullet}\}^{\times}$  using Yakub potential a) Conjugate gradient method b) rigid lattice method. The contour map expresses the brute energy as a function of the distance of each hole to the oxygen interstitial atom. When different configurations correspond to the same distances, the minimum value over these configurations is retained. The most stable configuration is observed for both holes located in second nearest neighbour to the oxygen interstitial, in opposite direction (along  $\langle 1\ 1\ 1 \rangle$  direction) from each other.

### 4.3. Verification of methods

The clustering of a single oxygen interstitial with one and two holes is compared to a brute force approach. All developed methods converge towards the same geometrical arrangement. In the case of a single hole, the hole is predicted to occupy the first nearest neighbour relative to the oxygen interstitial. With two holes, the predicted configuration of minimum energy consists of the holes being located in second nearest neighbour positions to the oxygen interstitial, as illustrated in Figure 4-5. They are located in opposite direction from each other, as expected based on pure electrostatic considerations; this configuration is also in good agreement with recent DFT calculations [85].

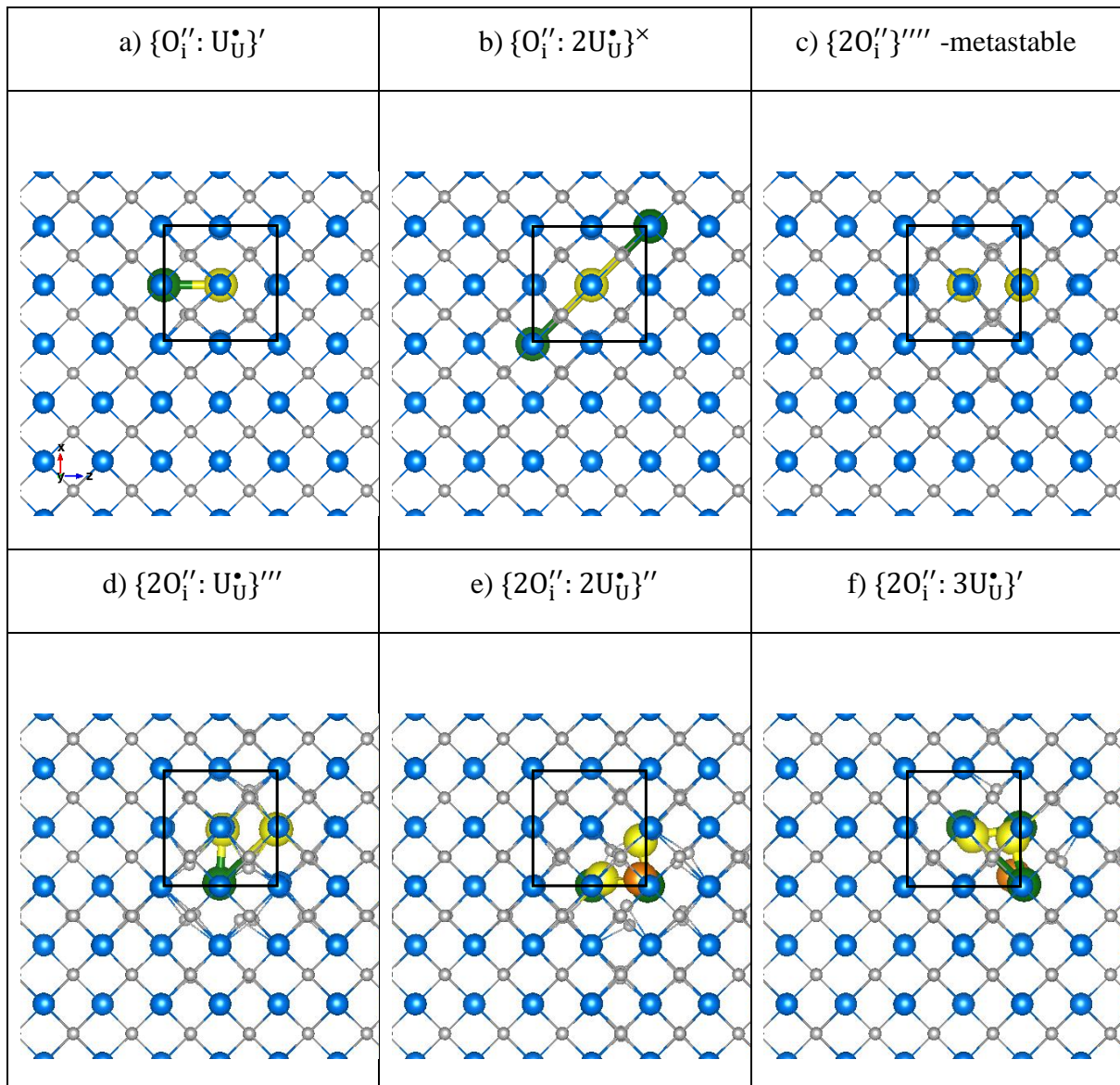


Figure 4-5 Yakub potential relaxed configurations of oxygen interstitial and interstitial clusters [29]. Blue and white spheres represent the regular uranium and oxygen ions in f.c.c  $UO_2$ . Yellow spheres stand for interstitial oxygen ions while the green ones for  $U^{5+}$  (holes) positions. For the case  $\{2O_i'' : 2U_U^\bullet\}''''$  and  $\{2O_i'' : 3U_U^\bullet\}'$  orange spheres are used to highlight oxygen ions displaced from their regular positions. For the sake of clarity, central vacancy sites are not emphasized.



Di-interstitial clusters were studied here as charge-compensated clusters, with one to four holes. The most stable arrangement of two oxygen interstitial atoms was first determined separately due to its metastable state; the presence of charge-compensating holes was considered in a second stage. Two oxygen interstitials were initially placed in the two nearest octahedral interstitial sites with a distance of  $\frac{\sqrt{2}}{2}$  times lattice parameter. The symmetric relaxation was observed to correspond to the optimal arrangement, i.e., the two closest neighbour oxygen interstitials as presented in Figure 4-5. The complex di-interstitial defect clusters with varying charges  $\{2O_i'' : pU_U^\bullet\}^{(4-p) \cdot}$  were then investigated. For a single charge-compensating hole  $\{2O_i'' : U_U^\bullet\}'''$ , the most stable configuration consists of the hole located on one of the closest neighbours of the oxygen interstitials. The structure of the  $\{2O_i'' : 2U_U^\bullet\}''$  and  $\{2O_i'' : 3U_U^\bullet\}'$  clusters, however, does not correspond to the traditional description from Willis, with two regular oxygen atoms displaced from their regular position [50]. While uranium ions are not displaced from their regular fluorite location, an alternative arrangement of the oxygen atoms was predicted here, with oxygen atoms stabilizing as a split di-interstitial  $\{3O_i'' : v_O^{\bullet\bullet}\}$ . In such a configuration, oxygen ions are arranged as a regular triangle, with positions along  $\langle 111 \rangle$  directions from a central oxygen vacancy. This structure, with a single oxygen atom displaced from its regular position, was also derived in DFT calculations [86,87]. Figure 4-5 depicts the predicted cluster configurations for  $UO_{2+x}$  using Yakub potential [29].

The present study predicts the progressive binding of the cluster  $\{2O_i''\}$  as it accumulates one, two and three holes, while the neutral cluster, with 4 holes, tends to be less stable. Figure 4-6 depicts the minimum energy configuration of a neutral di-interstitial cluster -  $\{2O_i'' : 4U_U^\bullet\}^x$  which was found in this study. The fourth hole  $\{U_U^\bullet\}$  is not bound to the cluster but stays far from the cluster of  $\{2O_i'' : 3U_U^\bullet\}'$ , behaving like a “free” hole. At this stage, this result already indicates that from a pure energy perspective, di-interstitial clusters of charge -1 could be encountered, as often suggested based on the interpretation of experimental data through point defect models. Further, the calculated higher order cluster configurations, such as  $3O_i$ ,  $4O_i$ ,  $5O_i$ , were not included in this study, being kept for future research (see section Conclusion & Outlook).

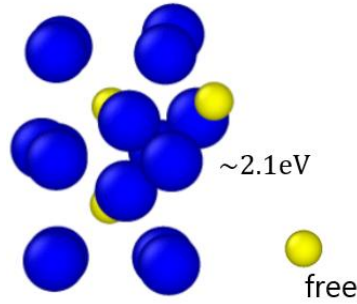


Figure 4-6 Minimum energy configuration of  $\{2O'' : 4U_U^\bullet\}^x$  cluster. Blue balls and yellow balls are oxygen and  $U^{5+}$  ( $U_U^\bullet$ ) atoms, respectively. For the sake of simplicity, ordinary uranium sites are not shown.  $\sim 2.1$  eV is the calculated cluster binding energy while free  $U_U^\bullet$  depicts the hole which is not bound to the cluster.

In a second phase, mixed oxide lattice configurations were predicted by the rigid lattice method [65]. Currently, two concise sets of interatomic potential were considered to investigate the material properties of a complex U-Pu-Am-Np-O system, namely the CRG potential set and the Arima potential set [30–32,37,38]. The method was validated for the case of  $U_{0.5}Pu_{0.5}O_2$  using the Arima potential set, for which an ideal, homogeneous mixture was observed, as shown in Figure 4-6. This finding is solely based on visual inspection. The predicted lattice configurations could be further validated by performing a series of additional calculations, e.g., by conducting a crystal structure analysis. The next steps will therefore include the performance of a series of calculations, such as computing the pair correlation function and the structure factor (Fourier transform) of such configurations. Besides, the current approach could be cross-checked with other approximations, which were developed to address solid solution configuration, e.g., SQS [88].

In contrast to the Arima set, a phase separation ( $UO_2$ - $PuO_2$ ) was observed by the CRG potential set, when the atomic interactions were defined [30–32,37,38]. This observation is also supported by the study of thermodynamic properties of  $U_{1-y}Pu_yO_2$  MOX fuel using classical molecular Monte Carlo simulations by Takoukam-Takoundjou et al. [89]. They confirm that the Pu clustering in MOX matrix is higher at 300 K than at 1000 K. This might ultimately lead to a phase separation at 0 K, which is in contradiction to recent experiments [63]. Due to the observed phase separation the CRG potential was eliminated for the following mixed oxide calculations [30,31]. Figure 4-7 a) shows the application of the rigid lattice method to the system of  $U_{0.5}Pu_{0.5}O_2$ .

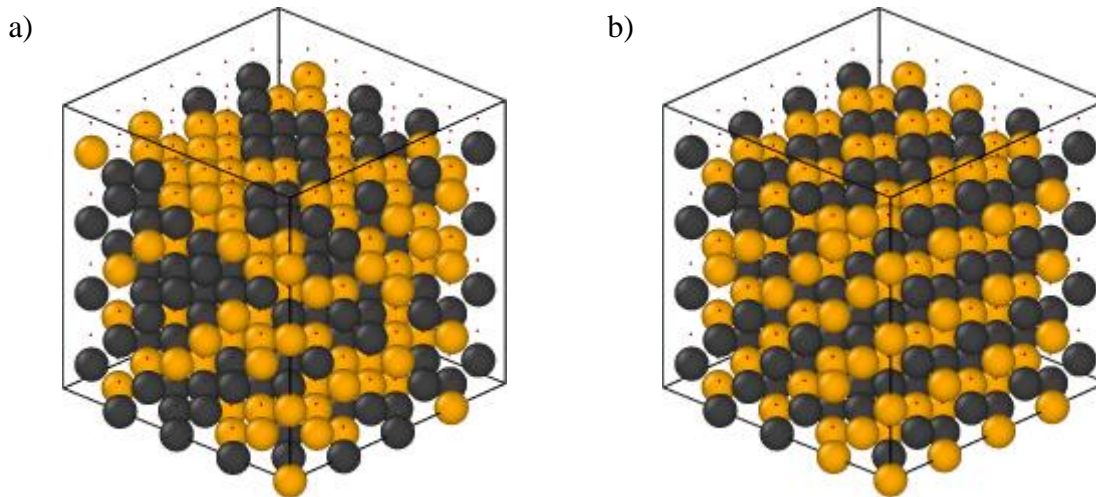


Figure 4-7 A  $4 \times 4 \times 4$  (768 atoms in total)  $U_{0.5}Pu_{0.5}O_2$  system. Black and yellow spheres represent the uranium and plutonium atoms, respectively. The small red dots represent regular oxygen ions. a) Initial (random) distribution of uranium and plutonium atoms in f.c.c. matrix b) Optimal configuration as predicted by the rigid lattice approach using Arima potential in this study [32].

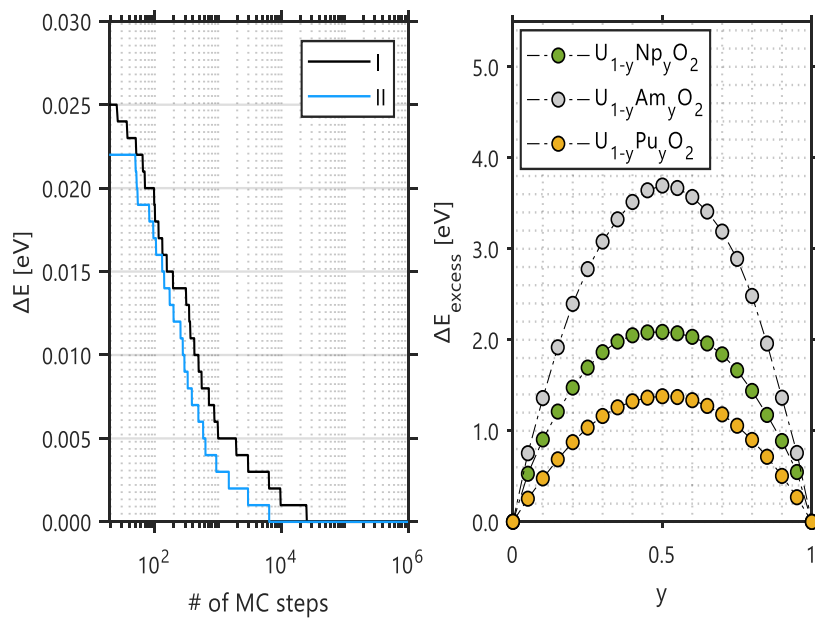


Figure 4-8 Left) Application of the rigid lattice method to the system of  $U_{0.5}Pu_{0.5}O_2$ , two random configurations were selected initially, I and II. Right) excess energy calculations for various system using CRG potential set:  $U_{1-y}Pu_yO_2$ ,  $U_{1-y}Am_yO_2$  and  $U_{1-y}Np_yO_2$  [30,31].

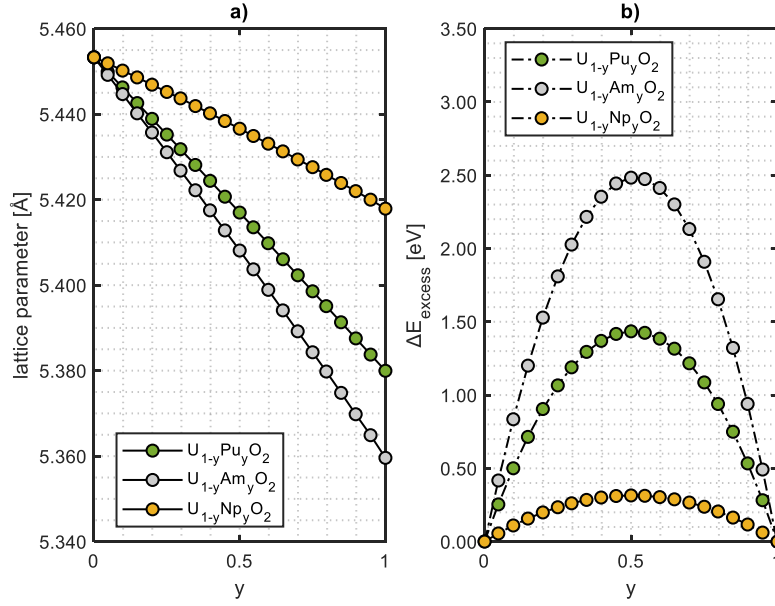


Figure 4-9 a) Calculated lattice parameter of the binary oxide system  $U_{1-y}Pu_yO_2$ ,  $U_{1-y}Am_yO_2$  and  $U_{1-y}Np_yO_2$  b) excess energy calculations for various system using Arima potential set [32,37,38]:  $U_{1-y}Pu_yO_2$ ,  $U_{1-y}Am_yO_2$  and  $U_{1-y}Np_yO_2$ .

In addition, to increase the reliability of the current research, the excess energy (or mixing enthalpy at 0 K) was calculated according to the following expression:

$$\Delta E_{\text{mix}} = E^{A+B} - (y_A E^A + y_B E^B) \quad (4-1)$$

Where  $E^{A+B}$  is the excess energy of A and B binary solid solution,  $E^A$  and  $E^B$  are the standard lattice energies of component A and B,  $y_A$  and  $y_B$  are the mole fractions of component A and B, respectively. The whole range of calculated excess energies as a function of atomic fractions for a binary oxide system are shown in Figure 4-7 b) using the CRG potential set and Figure 4-8 b) using the Arima potential set [30–32,37,38]. For both cases, the excess energies for  $U_{1-y}Pu_yO_2$ ,  $U_{1-y}Am_yO_2$  and  $U_{1-y}Np_yO_2$  fit well with a polynomial shape that corresponds to the minimum energy configuration as found by the rigid lattice method. Furthermore, the observed trend in  $\Delta E_{\text{mix}}$  corresponds to the  $\Delta E_{\text{mix}}^{U_{1-y}Np_yO_2} < \Delta E_{\text{mix}}^{U_{1-y}Pu_yO_2} < \Delta E_{\text{mix}}^{U_{1-y}Am_yO_2}$  relation observed with the Arima potential set, while  $\Delta E_{\text{mix}}^{U_{1-y}Pu_yO_2} < \Delta E_{\text{mix}}^{U_{1-y}Np_yO_2} < \Delta E_{\text{mix}}^{U_{1-y}Am_yO_2}$  is found with the CRG potential set. Figure 4-8 a) shows the lattice parameter for  $U_{1-y}Pu_yO_2$ ,  $U_{1-y}Am_yO_2$ ,  $U_{1-y}Np_yO_2$  system.

#### 4.4. Performance assessment

Table 4-1 The performance assessment for different methods.

$\{O_i'' : 2U_U\}^x$	<b>Conjugate Gradient</b>	<b>Rigid lattice</b>
<b>Full exploration</b>	~7 CPU-day	~15 CPU-min
<b>Monte Carlo (Metropolis acceptance)</b>	~30 CPU-day 100 M time-step	~2 CPU-min

The developed methods were compared with regard to their computational time. The performance assessment was carried out on the basis of  $\{O_i'' : 2U_U\}^x$  defective system and default LAMMPS input file while the system size was  $4 \times 4 \times 4$  [65]. In case of full configurational space exploration with rigid lattice method, the simulation time decreases by a factor 1000 compared to the conjugate gradient method as shown in Table 4-1. The rigid lattice method coupled with Monte Carlo Metropolis acceptance decreases the exploration time further by another factor 10. This coupled rigid lattice approach was thus observed to rapidly converge towards the optimal configuration, namely 10,000 times faster than with the brute approach (conjugate gradient) method. Based on the computing time gain and efficiency performance – convergence to the energy minimum is observed after about 5000 Monte-Carlo swaps.

The rigid lattice method was validated for the case of  $U_{0.5}Pu_{0.5}O_2$  for  $4 \times 4 \times 4$  unit-cell; the convergence to the energy minimum was observed after about 20,000 Monte-Carlo swaps which corresponds to ~8 CPU-min computational time.

## 5. Validation of the proposed approach: application to defect chemistry in $\text{UO}_{2+x}$

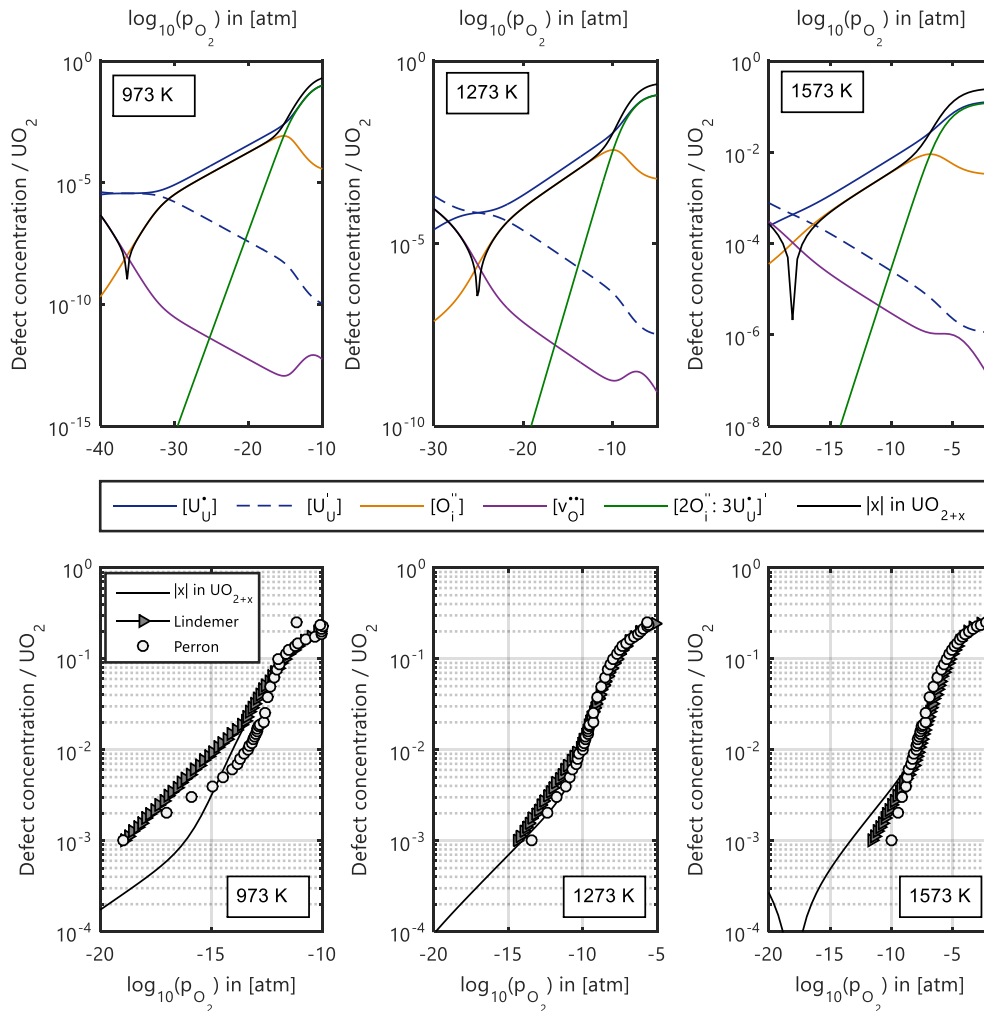


Figure 5-1 The deviation from stoichiometry  $x$  in  $\text{UO}_{2+x}$  (bottom row) is calculated from the defect concentrations over a range of temperatures (top row). Comparison is made with the correlations published by Lindemer and Besmann, and Perron's thermodynamic data [20,21].

The clustering behaviour of oxygen interstitials and holes was addressed by an empirical potential, based on atomic scale simulations. The defect energies were then interpreted by means of a PDM to derive the concentration of defects and defect clusters as a function of temperature and oxygen partial pressure as shown in Figure 5-1. The top row shows the individual defect concentrations over a range of temperatures (973 K - 1573 K). At low partial pressure, oxygen interstitials  $\text{O}'_{\text{i}}$  are dominating the non-stoichiometry in  $\text{UO}_{2+x}$ , the hole

concentrations  $U_U^\bullet$  follow the same slope of  $O_i''$  while the electron  $U_U'$  and vacancy oxygen  $v_o^{\bullet\bullet}$  concentration decreases sharply. At higher partial pressure, the oxygen cluster configuration  $\{2O_i'':3U_U^\bullet\}'$ , which was found in this study, starts to dominate the non-stoichiometry in  $UO_{2+x}$  and finally reaches the hole concentration  $U_U^\bullet$ . The bottom row depicts the comparison of calculated deviation from stoichiometry with experimental data taken from Lindemer and Besmann, and Perron [20,21]. At 1273 K and 1573 K good agreement between our model and experiments was achieved. This confirms that the proposed dominant defect-Willis with minus one charge- corresponds to those derived from experiments. At 973 K, both the experiments and the proposed model show slight inconsistencies. One should also consider that at low temperature (<600 K)  $UO_2$  exhibits a solid solution with  $U_4O_9$  in which the excess oxygen ions agglomerate into a cuboctahedron (CoT) structure [22,25,26,90]. Such a clustering configuration beyond the Willis might dominate the deviation from stoichiometry in  $UO_{2+x}$  at low temperatures. This statement, however, is based solely on theoretical considerations and is therefore not included in the current study but kept for future work (see Conclusion and Outlook). Details can be found in [91].

## 6. Application to Gen-IV fuels

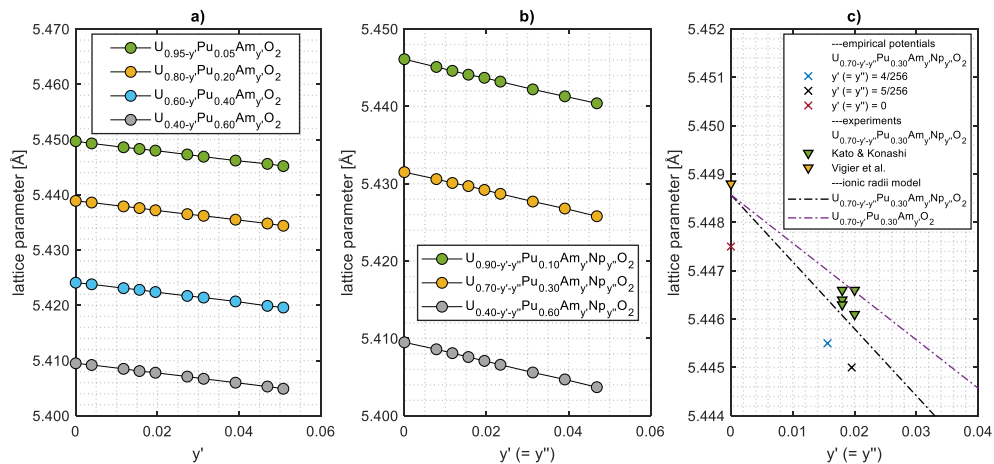


Figure 6-1 Relationship between lattice parameter and MA concentration for a complex a)  $U_{1-y-y'}Pu_yAm_{y'}O_2$  and b)  $U_{1-y-y'-y''}Pu_yAm_{y'}Np_{y''}O_2$  system as predicted by Arima et al. at 0 K. c) Comparison of this study's EP results to the experimental data, and the ionic radii model.

### Lattice parameter of Am, Np bearing MOX fuel

The lattice parameters of MOX fuel containing up to 5at% MA with maximum 60at% Pu were addressed by empirical potential based atomic scale simulations (see Figure 6-1). Lattice configurations were predicted by means of the Metropolis-Monte-Carlo method. The following results were found: Details can be found in [39]:

- Configurational space exploration of the arrangement of Pu, Am, Np in the host  $UO_2$  matrix was shown to be most effective with a rigid lattice approach – where no relaxation is performed in a first stage – in combination with a Monte Carlo-Metropolis particle swapping method.
- The lattice parameter of the binary oxide system  $U_{1-y}Pu_yO_2$ ,  $U_{1-y}Am_yO_2$ ,  $U_{1-y}Np_yO_2$  obeys a linear relation that corresponds to  $a_0^{mix} = (y_A - 1)a_0^{UO_2} + y_A a_0^{AO_2}$ .
- The lattice parameter of a complex  $U_{1-y-y'}Pu_yAm_{y'}O_2$  b)  $U_{1-y-y'-y''}Pu_yAm_{y'}Np_{y''}O_2$  system decreases linearly with an increasing amount of MA dissolved in the MOX fuel matrix.



### Melting point of Am, Np bearing MOX fuel (preliminary results)

Determining the melting point of nuclear fuel is of high importance as it indicates the stability of the material during accidental conditions. Experiments face difficulties at high temperature measurements, which is why trustable models need to be developed. In this part of the thesis, atomic scale tools will be used to predict the melting point of Am, Np bearing MOX fuel. Three ways of finding the melting point of such complex mixtures will, eventually be compared, namely from experimental data as published in the literature, by calculating it by means of the co-existence method and via free energy calculations that corresponds to  $F_{\text{solid}} = F_{\text{liquid}}$  where  $F$  is the system free energy.

- Melting temperature based on literature data and predicted by thermodynamic relations

Table 6-1 The melting temperature values of simple oxides.

	UO <sub>2</sub>	PuO <sub>2</sub>	AmO <sub>2</sub>	NpO <sub>2</sub>
T <sub>mAnO<sub>2</sub></sub> (K)	3120±30 [92]	2701±35 [92]	2448 [93]	3070±62 [94]

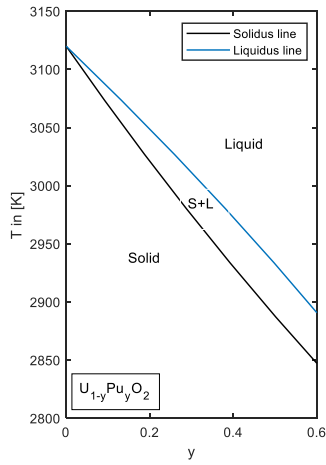
Assuming that the (U-Pu-Am-Np)O<sub>2</sub> mixture is ideal, as confirmed by the previous work [39], the thermodynamic relations for such complex mixture takes the form of Eq. (6-1) and Eq. (6-2) [95].

$$\Delta H_{\text{AnO}_2}^{\text{fus}} \left( \frac{T}{T_{\text{mAnO}_2}} - 1 \right) = RT \ln \left( \frac{c_{\text{AnO}_2}^{\text{sol.}}}{c_{\text{AnO}_2}^{\text{liq.}}} \right), \quad \text{An} = \text{U, Pu, Am or Np} \quad (6-1)$$

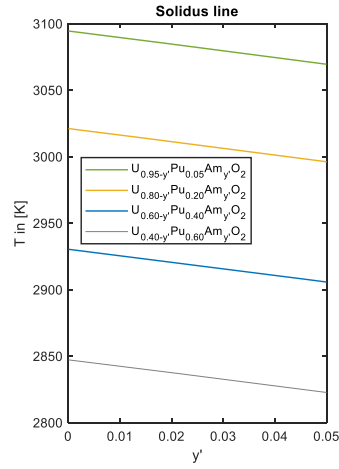
$$\sum_{\text{An}} c_{\text{AnO}_2}^{\text{sol.}} = 1 \quad \text{and} \quad \sum_{\text{An}} c_{\text{AnO}_2}^{\text{liq.}} = 1 \quad (6-2)$$

Where  $\Delta H_{\text{AnO}_2}^{\text{fus}}$  is heat of fusion (kJmol<sup>-1</sup>),  $c_{\text{AnO}_2}^{\text{sol.}}$  And  $c_{\text{AnO}_2}^{\text{sol.}}$  refer to the concentration of solid and liquid phase, respectively and  $T_{\text{mAnO}_2}$  is the melting temperature in Kelvin and  $R$  is gas constant. For the sake of simplicity,  $\Delta H_{\text{AnO}_2}^{\text{fus}} = 3RT_{\text{mAnO}_2}$  was assumed with the corresponding  $T_{\text{mAnO}_2}$  values simply taken from the literature, as tabulated in Table 6-1. Figure 6-2 shows the melting temperature of Am, Np bearing MOX fuel as predicted by thermodynamic relations e.g., numerical solution of Eq. (6-1) and Eq. (6-2).

a) Binary system



b) Ternary system



c) Quaternary system

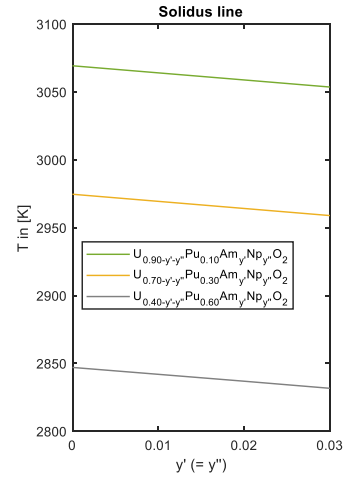


Figure 6-2 The melting temperature of Am, Np bearing MOX fuel as predicted by thermodynamic calculations of Eq. (6-1) and Eq. (6-2) based on literature data in Table 6-1. a) binary system b) ternary system c) quaternary system.

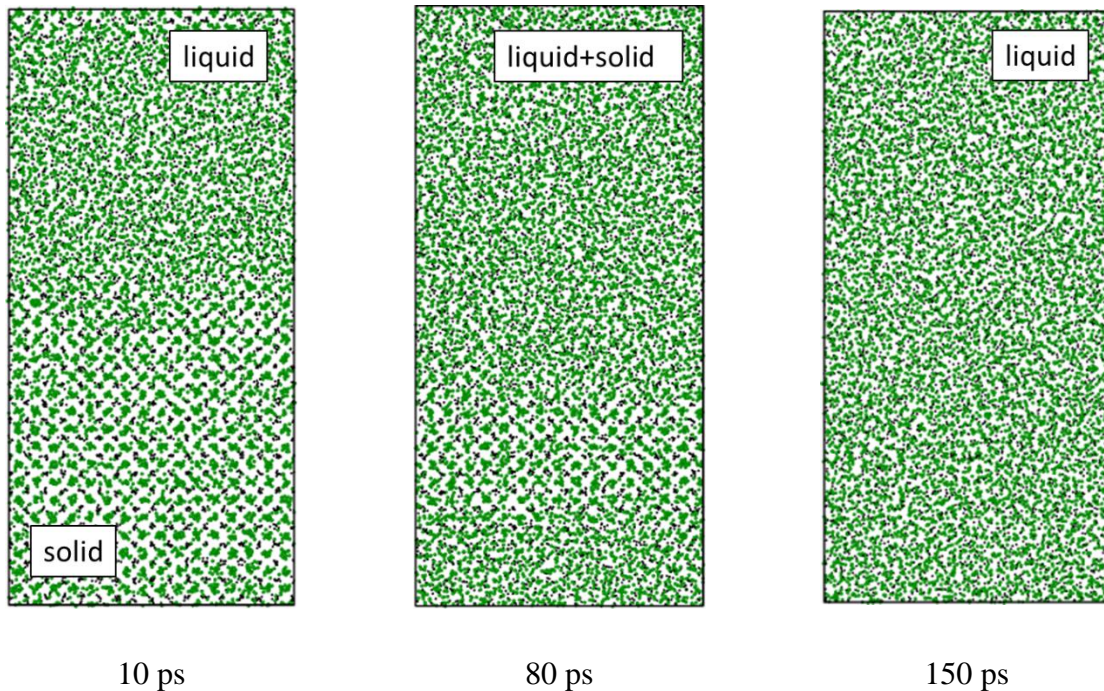


Figure 6-3 The time evaluation of the coexistence phases for a simple  $UO_2$  system using CRG potential at 3200 K. Black and green spheres represent the uranium and oxygen atoms, respectively [30,31].

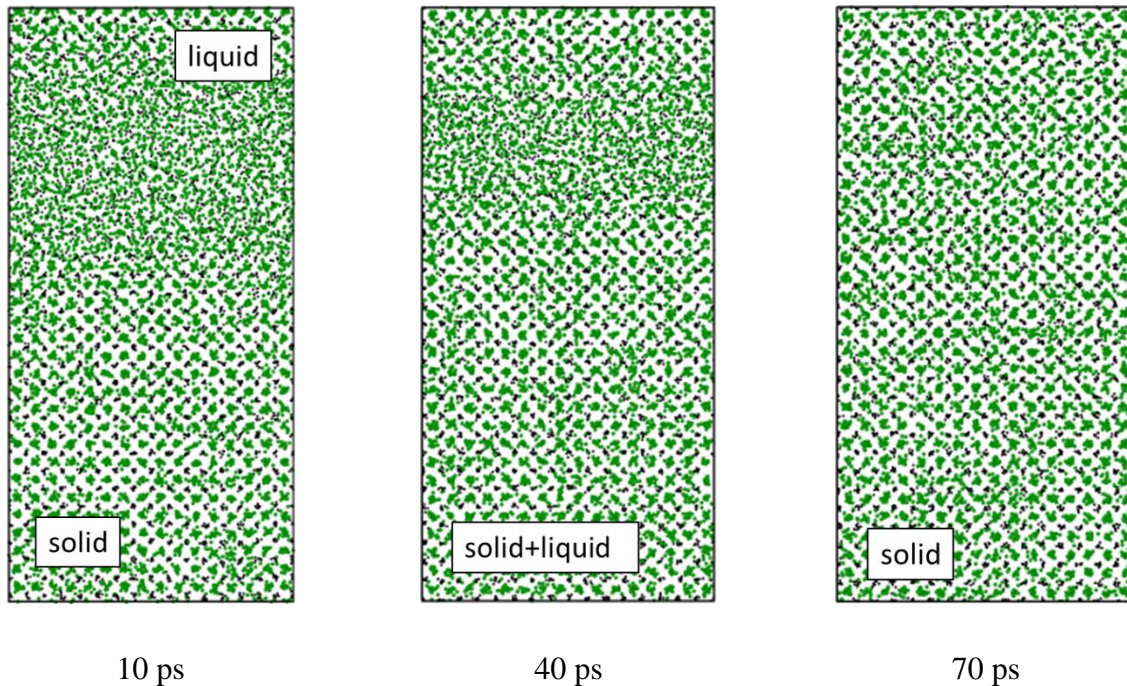


Figure 6-4 The time evaluation of the coexistence phases for a simple  $\text{UO}_2$  system using CRG potential at 2900 K. Black and green spheres represent the uranium and oxygen atoms, respectively [30,31].

- Coexistence method: Empirical potential study (ongoing research)

The melting temperature of Am, Np bearing MOX fuel will be performed using the concept of coexistence method where each phase is represented by the pristine  $8 \times 8 \times 8$  (total system is  $16 \times 8 \times 8$ ) cells system [96]. NPT (constant particle, pressure and temperature) simulations will be used to observe the system's evolution over time [96]. Figure 6-2 and Figure 6-3 depict the coexistence method for a simple  $\text{UO}_2$  system using CRG potential; the solid phase was created for half of the system at 300 K, while the other half was completely liquefied at a temperature of 4000 K. At 3200 K the system was observed to be totally liquid after about 150 ps, while at 2900 K the system was totally solid after about 70 ps. This confirms that the system's melting temperature, for which the solid-liquid phases are in equilibrium, would probably be in between those temperatures, however, somehow closer to 3200 K than to 2900 K because of the time period [97].

Currently, the developed coexistence method is being used to discover the melting temperatures of all simple actinide oxides, such as  $AnO_2$  where  $An = U, Pu, Am$  or  $Np$ . The method will be further extended to reproduce the melting temperatures of their binary, ternary, and quaternary mixtures. Finally, a comparative study will be carried out between available experimental data and empirical potential simulation results.

- Free energy calculations and melting point determination (ongoing research)

The melting temperature of the solid mixed oxide is found by means of free energy calculations, where the free energy of  $F_{solid} = F_{liquid}$ . In a MD perspective the free energy is taking the form of the following equation

$$F_1 - F_0 = \int_0^1 \left\langle -\frac{\partial H(\lambda)}{\partial \lambda} \right\rangle d\lambda \quad (6-3)$$

Where,  $F_1$  is the Helmholtz free energy of the system of interest and  $F_0$  is the Helmholtz free energy of the system, which is already known (e.g., Einstein solid or ideal gas). The lambda ( $\lambda$ ) is the coupling parameter of the thermodynamic integration and “ $\langle \rangle$ ” is the canonical ensemble average. Non-equilibrium approaches could be used to evaluate the thermodynamic integral shown in Eq. (6-3), namely adiabatic switching and reversible scaling [98,99]. The adiabatic switching method assumes that the  $\lambda(t)$  is a function of time, such that  $H(\lambda(t)) = \lambda(t)H_0 + [1 - \lambda(t)]H_1$  and the system of interest  $F_1$ , in the final form of  $F_1 - F_0 = \frac{1}{2} [W_{forward}^{irreversible} - W_{backward}^{irreversible}]$ , where  $W^{irreversible}$  is the irreversible work [98,99]. Figure 6-5 depicts the system’s Hamiltonian changes in the forward and backward direction with respect to  $\lambda$  parameter for  $UO_2$  using CRG potential at 300 K [30,31]. The reversible scaling method assumes that each value of  $\lambda_{new}$  corresponds to a particular temperature. Changing the  $\lambda_{new}$  will allow to predict the broad temperature of the Helmholtz free energy of the system of interest. The melting point will be the point where the free energy of solid and liquid is equal,  $F_{solid} = F_{liquid}$  [98,99]

Similarly, the free energy method will be used to compute melting temperatures of all simple oxides in a first step. The method will be further extended to reproduce the melting temperatures of their binary, ternary, and quaternary mixtures. Finally, a comparative study will be carried out between available experimental data, the coexistence method, and the free energy method.

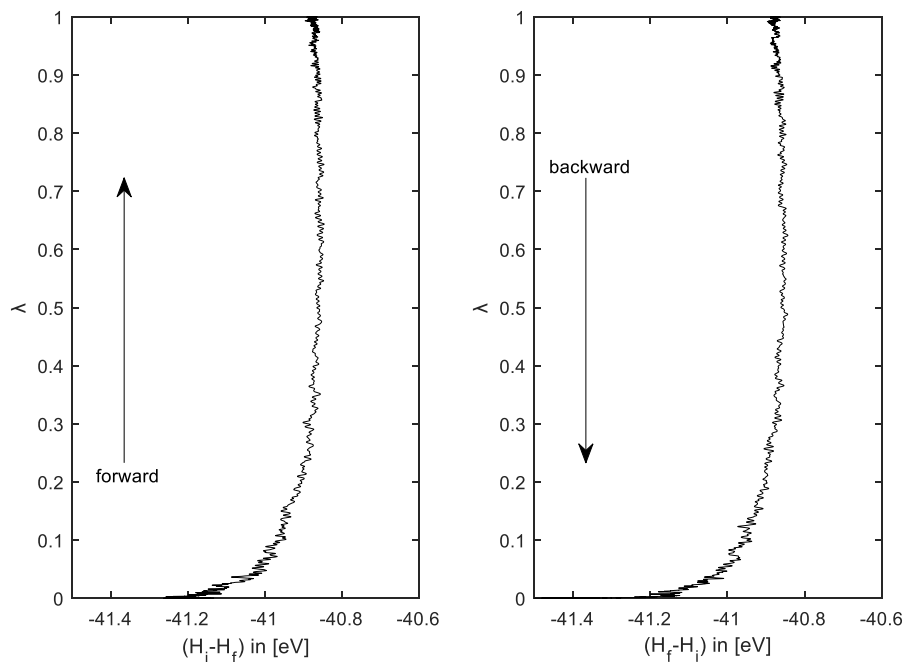


Figure 6-5 The system's Hamiltonian ( $H$ ) changes in the forward and backward direction with respect to  $\lambda$  parameter for  $\text{UO}_2$  using CRG potential at 300 K. The subscript  $i$  and  $f$  depict the initial and final system stage, respectively.

#### Contribution to the current literature (ongoing research)

- The melting temperature of actinide oxides, estimated so far, is in the error limit of  $\pm 25\text{-}20$  K when using the coexistence method. One of the advantages of the suggested free energy method is the fact that it will allow to decrease the error on the melting temperature.
- The coexistence method is generally very CPU demanding and requires large systems, while the free energy approach is considered to be hard to establish in a first step, but less CPU demanding for further studies.
- Changing the reference system in Eq. (6-3) will allow to also capture the defective system's melting temperature in future research efforts.

## 7. Conclusions & Outlook

A fundamental understanding of the physics is of paramount importance to design, develop and safely operate nuclear facilities. The overall goal of this thesis was therefore to comprehend the impact of atomic interactions on the nuclear fuel material properties. For this purpose, atomic scale simulations were performed for the nuclear fuels,  $\text{UO}_2$  and Gen-IV fuels. This research mainly focused on the atomic arrangement of defects and defect clustering inside the fuel matrix and on the lattice configuration of Gen-IV oxide fuels. Two sampling methods were used, namely energy minimization (batch sampling) and Metropolis-Monte Carlo method (continuous sampling).

Apart from that, a user friendly -Newton Raphson base- point defect model solver was developed, which is intended to be used also in further studies. The following sections give a detailed outlook for future research work potentially to be conducted building on this thesis' outcomes.

- An atomic scale analysis of defect clustering and predictions of their concentrations in  $\text{UO}_{2+x}$

In this research, the charge state of oxygen interstitial and interstitial clustering in  $\text{UO}_{2+x}$  was performed using a Buckingham type empirical potential [69]. As a first step, cluster involving a single oxygen interstitial and two holes  $\{O_i'' : 2U_U^\bullet\}^x$  was addressed. The most stable defect arrangement with two holes consists of these holes being located in the second nearest neighbour positions to the oxygen interstitial, in opposite directions to each other; this configuration agrees with DFT calculations [85]. Then complex di-interstitial defect clusters with varying charges  $\{2O_i'' : pU_U^\bullet\}^{(4-p)'}$  were investigated. For the case of  $\{2O_i'' : 3U_U^\bullet\}'$ , the split di-interstitial  $\{3O_i'' : v_O^{\bullet\bullet} : 3U_U^\bullet\}'$  form was observed to be the most stable arrangement. In such a configuration, oxygen ions are arranged as a regular triangle, with positions along  $\langle 111 \rangle$  directions from a central oxygen vacancy,  $v_O^{\bullet\bullet}$ . Similarly, the DFT calculations performed by Andersson et al. and Wang et al. also proved that the split di-interstitial configuration is the most stable form of two oxygen interstitials cluster (or Willis cluster) [86,87]. For future studies it would be interesting to perform the same DFT calculations e.g., for the  $\{3O_i'' : v_O^{\bullet\bullet} : 3U_U^\bullet\}'$  configuration, with the hole positions explicitly predicted by this study.

Moreover, the oxygen clusters up to di-interstitial were investigated, being the only experimentally proven defect configuration, by using EP simulations. Higher order oxygen

defect arrangements, such as 3Oi, 4Oi, 5Oi and their corresponding energy calculations, must be performed in order to give better conclusions about the dominant defects in  $UO_{2+x}$  [51,100].

Experimentally, one observes a domain where the power dependency of  $x$  goes as  $p_{O_2}^{\frac{1}{2}} = \frac{n}{p_{O_2}^{2(2n-p+1)}}$ , where  $n$  is the number of oxygen interstitial (Oi<sup>''</sup>) and  $p$  is the number of the holes ( $U_U^\bullet$ ) bound to the anion cluster [20,21,45]. This observation would be compatible with the clusters of limited size: {Oi<sup>''</sup>: 2 $U_U^\bullet$ }<sub>x</sub> ( $n=1$ ,  $p=2$ ), {2Oi<sup>''</sup>: 3 $U_U^\bullet$ }<sup>'</sup> ( $n=2$ ,  $p=3$ ), {3Oi<sup>''</sup>: 4 $U_U^\bullet$ }<sup>2'</sup> ( $n=3$ ,  $p=4$ ), {4Oi<sup>''</sup>: 5 $U_U^\bullet$ }<sup>3'</sup> ( $n=4$ ,  $p=5$ ) and {5Oi<sup>''</sup>: 6 $U_U^\bullet$ }<sup>4'</sup> ( $n=5$ ,  $p=6$ ). Figure 7-1 depicts the possible (dominant) anion cluster configurations predicted by EP based atomic scale simulations using Yakub potential. Cluster energy calculations are part of ongoing research [29,35]. In addition to that, future research could also be extended to the hypo stoichiometric  $UO_2$  domain. Park and Olander [46] or Crocombette et al. [101], for example, suggested various charge states of vacancy oxygen and vacancy oxygen clustering in  $UO_{2-x}$  using experimental data fitting and DFT modelling, respectively. As an alternative to these methods, performing the simulation with an empirical potential study would be of added value.

The clustering behaviour of oxygen interstitials and holes was investigated by empirical potential based atomic scale simulations. The defect energies were then interpreted by means of a PDM to derive the concentration of defects and defect clusters as a function of temperature and oxygen partial pressure. A validation of the methodology and the results is then conducted based on deviation from stoichiometry in  $UO_{2+x}$ . The study could be further validated through the lattice parameter data as a function of stoichiometry which can be used as a test of the defect concentration predictions. Also, electrical conductivity data could be added to the picture to cross-check the results.

Further, this thesis' results can potentially be extended to  $U_4O_9$  and  $U_3O_7$  [102]. Experiments found that uranium exhibits  $U^{4+}$  and  $U^{5+}$  charge states in  $U_4O_9$  and  $U_3O_7$  super-cells. To support the available experimental data, it would be interesting to perform an empirical potential study and a structure analysis for those phases.

In the future, this thesis' results will also allow to discuss the solubility of different fission products and dopants such as Cr, Gd etc., in the  $UO_2$  matrix at EP level.

- Lattice parameter of Am, Np bearing MOX fuel: an empirical potential study

The lattice parameters of MA containing MOX fuel at various atomic fractions were addressed by empirical potential based atomic scale simulations. Lattice configurations were predicted by a systematic Metropolis-Monte Carlo method [65]. A very simple empirical interatomic potential was used to describe the interactions of systems with electrons *f*. For future studies it is recommended to repeat this approach by using other available pair potentials, which have been developed so far to address actinide oxide systems [33,103].

In addition, further empirical potential studies of minor-actinide containing MOX should also include the valence state modifications, e.g., Am and U cations ( $\text{Am}^{3+}$  and  $\text{U}^{5+}$ ) as suggested by experiments Lebreton et al. [104] and DFT calculations Talla Noutack et al. [105].

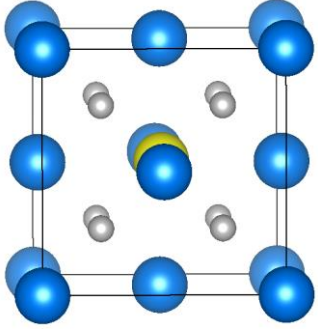
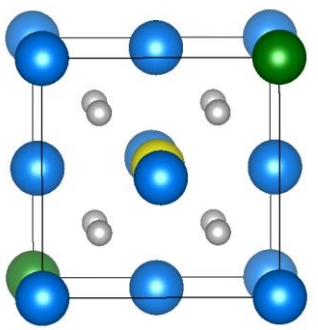
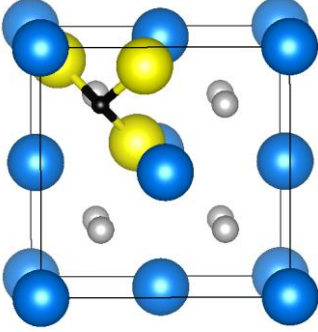
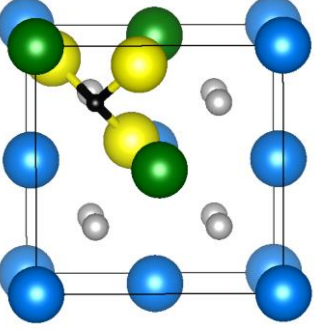
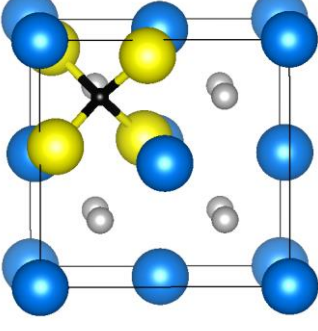
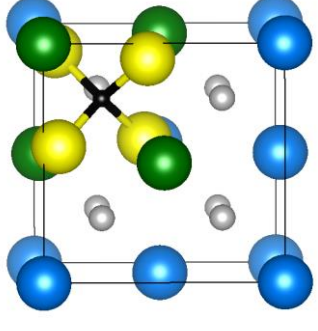
The predicted lattice configurations could be further validated by performing a series of additional calculations e.g., by conducting a crystal structure analysis. The next steps will therefore include the performance of a series of calculations, such as computing the pair correlation function and the structure factor (Fourier transform) of such configurations. Besides, the current approach could be cross-checked with other approximations, which were developed to address solid solution configuration e.g., SQS [88].

The work which has been carried out for the lattice parameter of Am, Np bearing MOX fuel is considered to be only the start of an upcoming series building on this work. In the second stage complex melting point and thermal conductivity calculations will be tackled.

The first part of this thesis covered the non-stoichiometry in  $\text{UO}_2$ ; these calculations will be stepwise extended to binary, ternary and quaternary oxide systems which were discussed within the Gen IV fuel concept. The preliminary results of the free energy calculations will be used, ultimately, to construct phase diagrams of oxide-materials at EP level as a long-term project.

Finally, to satisfy the author's intellectual curiosity, the knowledge gained from using the LAMMPS software will be used to understand the molecular mechanisms involved in the PUREX solvent extraction process, e.g., for the system of uranyl (nitrate) and/or plutonyl (nitrate)-TBP-diluent (nDD)- $\text{HNO}_3$ -  $\text{H}_2\text{O}$ .



$O_i''$	$\{O_i'' : 2U_{ij}^*\}^x$
	
$\{2O_i''\}^{4'}$	$\{2O_i'' : 3U_{ij}^*\}^1$
	
$\{3O_i''\}^{6'}$	$\{3O_i'' : 4U_{ij}^*\}^{2'}$
	

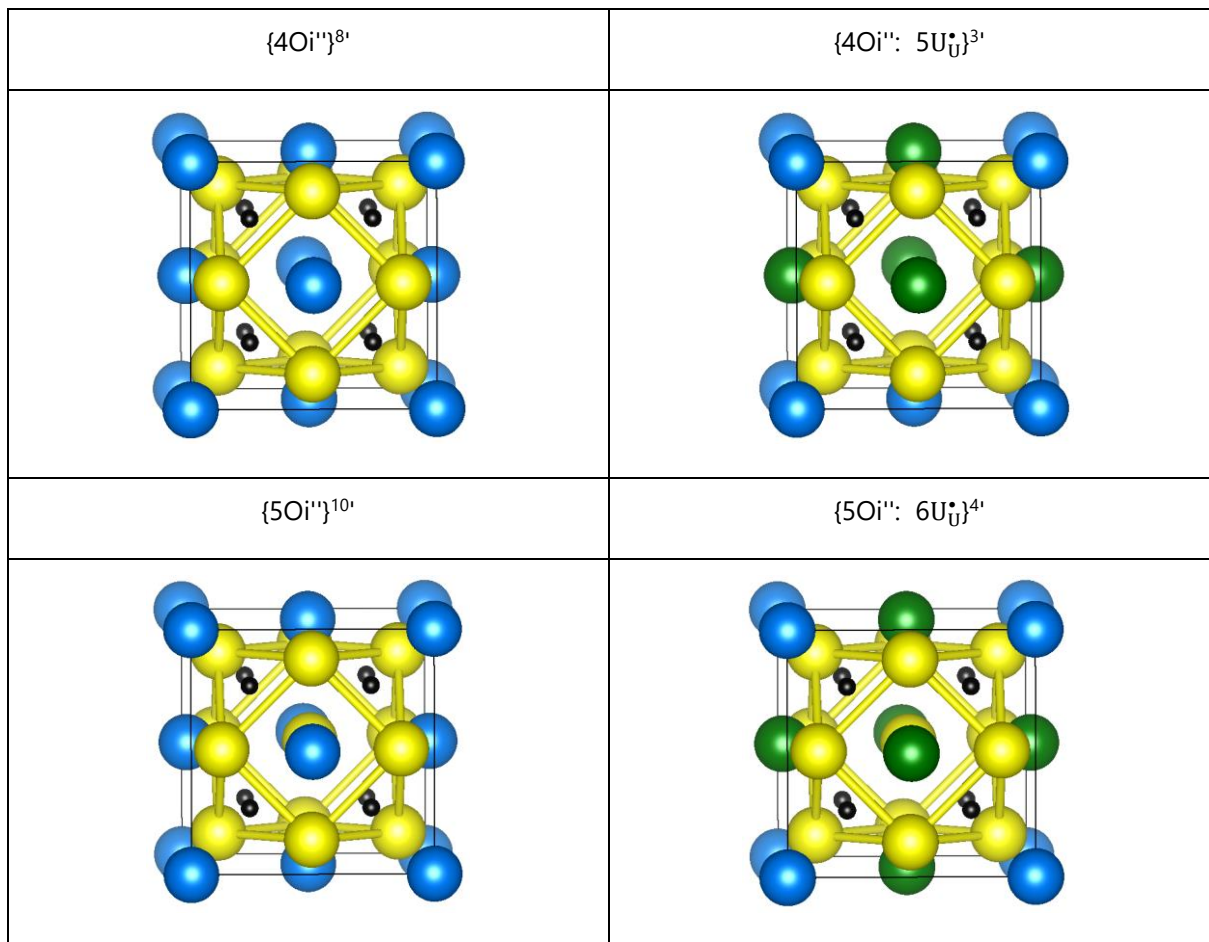


Figure 7-1 Yakub potential prediction to the possible anion cluster configurations in  $UO_2$  unit-cell [29,35]. Blue balls represent ordinary uranium atoms, white balls oxygen atoms. Yellow balls represent the excess oxygen atoms ( $O_i^{\bullet\bullet}$ ) in the unit-cell of  $UO_2$ , while green and black balls are localised  $U^{5+}$  ( $U_U^{\bullet}$ ) and vacancy oxygen positions ( $v_o^{\bullet\bullet}$ ), respectively. The graphs in the left column show the non-neutral anion clustering configurations, while the graphs in the right column show the charge compensated clustering configurations, which correspond to the power dependency of  $1/2$ .

## 8. List of Figures

Figure 1-1 $^{235}\text{U}$ fission yield (FY) as a function of fragment mass. $E_i$ is the incoming neutron energy. ENDF stands for US Evaluated Nuclear Data File / version B-VIII.0. (From [5].) .....	2
Figure 1-2 Comparison of total fission cross-sections of $^{235}\text{U}$ , $^{238}\text{U}$ and $^{239}\text{Pu}$ . ENDF stands for US Evaluated Nuclear Data File / version B-VIII.0. (From [5].) .....	3
Figure 1-3 Schematic view of a) double dish chamfered fuel pellet, b) nuclear fuel element, and c) nuclear fuel assembly. (From [11].).....	5
Figure 1-4 Schematic diagram of nuclear fuel cycle (NFC). RepU stands for reprocessed uranium. ....	6
Figure 1-5 A typical pressurised water reactor (PWR) nuclear steam supply system (NSSS). (From [13].).....	8
Figure 1-6 The molecular structure of tri butyl phosphate (TBP) and hydrocarbon: n-dodecane (nDD). ....	11
Figure 1-7 Effect of nitric acid concentration on distribution coefficients in 30% v/o TBP 80% uranium saturation at room temperature. (From [12].) .....	13
Figure 1-8 Uranium spot price in USD per pound from 1990 to 2021.....	14
Figure 1-9 Radiotoxicity (Sv/tHM) of 1t of SF from a PWR (initial enrichment 4.2 wt% $^{235}\text{U}$ , burn-up 50 GWd/tHM) as a function of time after discharge (year). a) Contribution of fission products (FP), plutonium (Pu) and minor actinides (MA) to radiotoxicity. b) Modification of radiotoxicity due to separation of U, Pu or U, Pu and MA. (From [17].).....	16
Figure 2-1 Uranium-oxygen phase diagram. (From [19].) .....	17
Figure 2-2 a) and b) Various perspectives of the unit cell of uranium dioxide. The black balls represent uranium cations, the red balls stand for oxygen anions and the green balls signify (c) the interstitial sites. The (110) plane of the unit cell, which has 4 oxygen ions, contains octahedral sites at the mid-point of the plane as well as at the centers of two edges. ....	19
Figure 2-3 The radial distribution function $g(r)$ of O-O, U-O and U-U within a $r=10 \text{ \AA}$ (cut-off) distance at 300 K and 3000 K calculated in this thesis using Yakub potential [29]......	20

Figure 2-4 Temperature dependence of  $\text{UO}_2$  properties as predicted by CRG potential [30,31]  
a) lattice parameter [L] b) thermal expansion coefficient [ $\alpha_L = \frac{1}{L} \frac{\partial L}{\partial T}$ ] c) change in system enthalpy [ $\Delta H$ ] and d) specific heat  $c_p = \frac{\partial H}{\partial T}$ . Experimental data were taken from [40]. 21

Figure 2-5 The deviation from stoichiometry  $x$  in  $\text{UO}_{2+x}$ . The left graph is taken from Lindemer and Besmann's work, the right graph is the comparison of Blackburn et al.'s, Perron and Lindemer's and Besman's work [20,21,53]. 23

Figure 2-6 The crystalline structure of  $\beta\text{-U}_4\text{O}_{9-y}$  proposed by Cooper and Willis [22]. The grey balls represent uranium atoms, the blue balls stand for regular oxygen atoms and the green balls signify the cuboctahedron arrangement of oxygen ions. a) shows the whole lattice arrangement, b) is the cuboctahedron arrangement with a central oxygen and c) is the corresponding atomic coordinates with  $a_1$ - $a_4$  and  $b_1$ - $b_8$  positional parameters. 24

Figure 3-1 The energy landscape as a function of conformation space. 31

Figure 3-2 Mott-Littleton method: division of space into three regions. 33

Figure 3-3 Metropolis criterion of acceptance. 34

Figure 4-1 MC-MD method carried out at 2000 K swap temperature for a system of  $\{\text{O}_i'' : 2\text{UU} \bullet\} \times$  using Yakub potential [29]. 41

Figure 4-2 The energy comparison with MC-MD method and conjugate gradient method for a system of  $\{\text{O}_i'' : 2\text{UU} \bullet\} \times$  using Yakub potential [29]. 42

Figure 4-3 Rigid lattice method coupled with Monte Carlo metropolis algorithm for a system of  $\{\text{O}_i'' : 2\text{UU} \bullet\} \times$  using Yakub potential [29]. 43

Figure 4-4 The configuration maps for a system of  $\{\text{O}_i'' : 2\text{UU} \bullet\} \times$  using Yakub potential a) Conjugate gradient method b) rigid lattice method. The contour map expresses the brute energy as a function of the distance of each hole to the oxygen interstitial atom. When different configurations correspond to the same distances, the minimum value over these configurations is retained. The most stable configuration is observed for both holes located in second nearest neighbour to the oxygen interstitial, in opposite direction (along  $\langle 1\ 1\ 1 \rangle$  direction) from each other. 44

Figure 4-5 Yakub potential relaxed configurations of oxygen interstitial and interstitial clusters [29]. Blue and white spheres represent the regular uranium and oxygen ions in f.c.c  $\text{UO}_2$ . Yellow spheres stand for interstitial oxygen ions while the green ones for  $\text{U}^{5+}$  (holes) positions. For the case  $\{2\text{O}_i'' : 2\text{UU} \bullet\}''$  and  $\{2\text{O}_i'' : 3\text{UU} \bullet\}'$  orange spheres are used to highlight oxygen

ions displaced from their regular positions. For the sake of clarity, central vacancy sites are not emphasized.....45

Figure 4-6 Minimum energy configuration of  $20i'' : 4UU \bullet x$  cluster. Blue balls and yellow balls are oxygen and  $U^{5+} UU \bullet$  atoms, respectively. For the sake of simplicity, ordinary uranium sites are not shown.  $\sim 2.1$  eV is the calculated cluster binding energy while free  $UU \bullet$  depicts the hole which is not bound to the cluster.....47

Figure 4-7 A  $4 \times 4 \times 4$  (768 atoms in total)  $U_{0.5}Pu_{0.5}O_2$  system. Black and yellow spheres represent the uranium and plutonium atoms, respectively. The small red dots represent regular oxygen ions. a) Initial (random) distribution of uranium and plutonium atoms in f.c.c. matrix b) Optimal configuration as predicted by the rigid lattice approach using Arima potential in this study [32]. .....48

Figure 4-8 Left) Application of the rigid lattice method to the system of  $U_{0.5}Pu_{0.5}O_2$ , two random configurations were selected initially, I and II. Right) excess energy calculations for various system using CRG potential set:  $U_{1-y}Pu_yO_2$ ,  $U_{1-y}Am_yO_2$  and  $U_{1-y}Np_yO_2$  [30,31].....48

Figure 4-9 a) Calculated lattice parameter of the binary oxide system  $U_{1-y}Pu_yO_2$ ,  $U_{1-y}Am_yO_2$  and  $U_{1-y}Np_yO_2$  b) excess energy calculations for various system using Arima potential set [32,37,38]:  $U_{1-y}Pu_yO_2$ ,  $U_{1-y}Am_yO_2$  and  $U_{1-y}Np_yO_2$ . .....49

Figure 5-1 The deviation from stoichiometry  $x$  in  $UO_{2+x}$  (bottom row) is calculated from the defect concentrations over a range of temperatures (top row). Comparison is made with the correlations published by Lindemer and Besmann, and Perron's thermodynamic data [20,21]. .....51

Figure 6-1 Relationship between lattice parameter and MA concentration for a complex a)  $U_{1-y-y'}Pu_yAm_{y'}O_2$  and b)  $U_{1-y-y'-y''}Pu_yAm_{y'}Np_{y''}O_2$  system as predicted by Arima et al. at 0 K. c) Comparison of this study's EP results to the experimental data, and the ionic radii model....53

Figure 6-2 The melting temperature of Am, Np bearing MOX fuel as predicted by thermodynamic retaliations of Eq. (6-1) and Eq. (6-2) based on literature data in Table 6-1. a) binary system b) ternary system c) quaternary system. ....55

Figure 6-3 The time evaluation of the coexistence phases for a simple  $UO_2$  system using CRG potential at 3200 K. Black and green spheres represent the uranium and oxygen atoms, respectively [30,31].....55

Figure 6-4 The time evaluation of the coexistence phases for a simple  $\text{UO}_2$  system using CRG potential at 2900 K. Black and green spheres represent the uranium and oxygen atoms, respectively [30,31].....56

Figure 6-5 The system's Hamiltonian (H) changes in the forward and backward direction with respect to  $\lambda$  parameter for  $\text{UO}_2$  using CRG potential at 300 K. The subscript i and f depict the initial and final system stage, respectively. ....58

Figure 7-1 Yakub potential prediction to the possible anion cluster configurations in  $\text{UO}_2$  unit-cell [29,35]. Blue balls represent ordinary uranium atoms, white balls oxygen atoms. Yellow balls represent the excess oxygen atoms ( $\text{O}_i$ ) in the unit-cell of  $\text{UO}_2$ , while green and black balls are localised  $\text{U}^{5+}$  ( $\text{UU} \bullet$ ) and vacancy oxygen positions ( $\text{VO} \bullet\bullet$ ), respectively. The graphs in the left column show the non-neutral anion clustering configurations, while the graphs in the right column show the charge compensated clustering configurations, which correspond to the power dependency of  $1/2$ . ....63

## 9. List of Tables

Table 1-1 A typical nuclear power reactor data (From [6].).....	9
Table 2-1 Comparison of bulk properties of UO <sub>2</sub> .....	22
Table 4-1 The performance assessment for different methods.....	50
Table 6-1 The melting temperature values of simple oxides.....	54

## 10. List of Abbreviations / Acronyms

UA	:	University of Antwerp
ULB	:	Université Libre de Bruxelles
SCK CEN	:	Studiecentrum voor de Toepassingen van de Kernenergie (The Belgian Nuclear Research Centre)
CEA	:	Commissariat à l’Energie Atomique et aux Energies Alternatives (The French Alternative Energies and Atomic Energy Commission)
UO <sub>2</sub>	:	Uranium dioxide
U <sub>4</sub> O <sub>9</sub>	:	Tetrauranium nonaoxide
U <sub>3</sub> O <sub>7</sub>	:	Triuranium heptaoxide
U <sub>3</sub> O <sub>8</sub>	:	Triuranium octoxide
UO <sub>3</sub>	:	Uranium trioxide
Ep	:	Empirical potential
FP	:	Fission product
ENDF/B-VIII.0	:	US evaluated nuclear data File / version B-VIII.0
MOX	:	Mixed oxide
GEN II-III-IV	:	Generation II-III-IV
MA	:	Minor actinide
CERCER	:	Ceramic-ceramic combinations
CERMET	:	Ceramic-metal composites



NFC	:	Nuclear fuel cycle
RePU	:	Reprocessed uranium
PWR	:	Pressurized water reactor
LWR	:	Light water reactor
IDR	:	Integrated dry route
NSSS	:	Nuclear steam supply system
W	:	Westinghouse
B&W	:	Babcock and Wilcox
CE	:	ABB combustion engineering
BWR	:	Boiling water reactor
HTGR	:	High temperature gas reactor
LMFBR	:	Liquid metal fast breeder reactor
GCFR	:	Gas cooled fast reactor
CANDU	:	Canada deuterium uranium
PHWR	:	Pressurized heavy water reactor
nDD	:	n-dodecane
SF	:	Spent fuel
PUREX	:	Plutonium uranium extraction
NFC	:	Nuclear fuel cycle
USD	:	United states dollar
HLW	:	High level waste

P&T	:	Partitioning and transmutation
FNR	:	Fast neutron reactor
ADS	:	Accelerator driven system
CRG	:	Cooper, Rushton and Grimes
DFT	:	Density functional theory
LAMMPS	:	Large-scale Atomic/Molecular Massively Parallel Simulator
GULP	:	General Utility Lattice Program
FORTTRAN	:	Formula translating system
C++	:	C class programming language
COMB	:	Charge optimized many-body potentials
SMTB-Q	:	Second-moment tight-binding variable-charge interatomic potentials
EAM	:	Embedded atom method potential
BMH	:	Born-Mayer-Huggins
Buckingham-4	:	Buckingham 4 ranges
MD	:	Molecular dynamics
MC	:	Monte carlo
PDM	:	Point defect model
J	:	Jacobian matrix
f.c.c	:	face centred cubic
SQS	:	Special Quasi-random Structure

CPU : Central processing unit

NPT : Constant Number of particles, Pressure and Temperature  
(ensemble)

## 11. Bibliography

- [1] O. Hahn, F. Strassmann, Über den Nachweis und das Verhalten der bei der Bestrahlung des Urans mittels Neutronen entstehenden Erdalkalimetalle, *Naturwissenschaften*. 27 (1939) 11–15.
- [2] L. Meitner, O.R. Frisch, Disintegration of uranium by neutrons: a new type of nuclear reaction, *Nature*. 143 (1939) 239–240.
- [3] O.R. Frisch, Physical evidence for the division of heavy nuclei under neutron bombardment, *Nature*. 143 (1939) 276.
- [4] T.R. England, B.F. Rider, Evaluation and compilation of fission product yields 1993, Los Alamos National Lab., 1995.
- [5] D.A. Brown, M.B. Chadwick, R. Capote, A.C. Kahler, A. Trkov, M.W. Herman, A.A. Sonzogni, Y. Danon, A.D. Carlson, M. Dunn, ENDF/B-VIII. 0: The 8th major release of the nuclear reaction data library with CIELO-project cross sections, new standards and thermal scattering data, *Nucl. Data Sheets*. 148 (2018) 1–142.
- [6] J.J. Duderstadt, *Nuclear reactor analysis*, Wiley, 1976.
- [7] L. Grancea, A. Hanly, *Uranium 2018: Resources, Production and Demand*, Organisation for Economic Co-Operation and Development, 2018.
- [8] D.R. Olander, *Fundamental aspects of nuclear reactor fuel elements: solutions to problems*, California Univ., Berkeley (USA). Dept. of Nuclear Engineering, 1976.
- [9] I.I. Konovalov, Y.S. Stetsky, *Development status of metallic, dispersion and non-oxide advanced and alternative fuels for power and research reactors*, IAEA-TECDOC-1374, International Atomic Agency, Vienna (Austria), 2003.
- [10] C. V Sundaram, S.L. Mannan, *Nuclear fuels and development of nuclear fuel elements*, *Sadhana*. 14 (1989) 21–57.
- [11] W. Doerr A., Hoff, W. Jentzen, D. Curran, A. Chotard, P. Deydier, *Nuclear reactor green and sintered fuel pellets, corresponding fuel rod and fuel assembly*, United States Pat. Appl. US 2011/01 (2011).
- [12] P.D. Manson Benedict, P.D. Thomas H. Pigford, P.D.H.W. Levi, *Nuclear Chemical Engineering, Second Edition*, 2nd editio, McGraw-Hill Education, New York, 1981.

- [13] Y.A. Hassan, R.A. Chaplin, Nuclear Energy Materials and Reactors-Volume I, EOLSS Publications, 2010.
- [14] IAEA, Advanced Fuel Pellet Materials and Designs for Water Cooled Reactors / TECDOC-1416, 2004.
- [15] M.J. Driscoll, T.J. Downar, E.E. Pilat, The linear reactivity model for nuclear fuel management, American Nuclear Society La Grange Park, Illinois, 1990.
- [16] EASAC (European Academies Science Advisory Council), Management of Spent Nuclear Fuel and Its Waste, 2014. <https://ec.europa.eu/jrc/sites/jrcsh/files/jrc-report-anagement-spent-fuel-and-waste.pdf>.
- [17] H. Freiersleben, Endlagerung von radioaktivem Abfall in Deutschland, TU Dresden, Dez. (2011).
- [18] M. Salvatores, Nuclear fuel cycle strategies including partitioning and transmutation, Nucl. Eng. Des. 235 (2005) 805–816.
- [19] C. Guéneau, M. Baichi, D. a al Labroche, C. Chatillon, B. Sundman, Thermodynamic assessment of the uranium–oxygen system, J. Nucl. Mater. 304 (2002) 161–175.
- [20] T.B. Lindemer, T.M. Besmann, Chemical thermodynamic representation of  $\text{UO}_{2+x}$ , J. Nucl. Mater. 130 (1985) 473–488.
- [21] P.O. Perron, THERMODYNAMICS OF NONSTOICHIOMETRIC URANIUM DIOXIDE., Atomic Energy of Canada Ltd., Chalk River (Ontario), 1968.
- [22] R.I. Cooper, B.T.M. Willis, Refinement of the structure of  $\beta\text{-U}_4\text{O}_9$ , Acta Crystallogr. Sect. A Found. Crystallogr. 60 (2004) 322–325.
- [23] R.J. McEachern, A review of kinetic data on the rate of  $\text{U}_3\text{O}_7$  formation on  $\text{UO}_2$ , J. Nucl. Mater. 245 (1997) 238–247.
- [24] R.J. McEachern, P. Taylor, A review of the oxidation of uranium dioxide at temperatures below 400 C, J. Nucl. Mater. 254 (1998) 87–121.
- [25] J.D. Higgs, B.J. Lewis, W.T. Thompson, Z. He, A conceptual model for the fuel oxidation of defective fuel, J. Nucl. Mater. 366 (2007) 99–128.
- [26] D.J.M. Bevan, I.E. Grey, B.T.M. Willis, The crystal structure of  $\beta\text{-U}_4\text{O}_9-y$ , J. Solid State Chem. 61 (1986) 1–7.

- [27] F. Grønvold, High-temperature X-ray study of uranium oxides in the  $\text{UO}_2$ – $\text{U}_3\text{O}_8$  region, *J. Inorg. Nucl. Chem.* 1 (1955) 357–370.
- [28] V. Trillaud, R. Podor, S. Gossé, A. Mesbah, N. Dacheux, N. Clavier, Early stages of  $\text{UO}_2+x$  sintering by in situ high-temperature environmental scanning electron microscopy, *J. Eur. Ceram. Soc.* 40 (2020) 5891–5899.
- [29] E. Yakub, C. Ronchi, D. Staicu, Computer simulation of defects formation and equilibrium in non-stoichiometric uranium dioxide, *J. Nucl. Mater.* 389 (2009) 119–126.
- [30] M.W.D. Cooper, M.J.D. Rushton, R.W. Grimes, A many-body potential approach to modelling the thermomechanical properties of actinide oxides, *J. Phys. Condens. Matter.* 26 (2014) 105401.
- [31] M.W.D. Cooper, S.T. Murphy, M.J.D. Rushton, R.W. Grimes, Thermophysical properties and oxygen transport in the  $(\text{U}_x, \text{Pu}_{1-x})\text{O}_2$  lattice, *J. Nucl. Mater.* 461 (2015) 206–214.
- [32] T. Arima, S. Yamasaki, Y. Inagaki, K. Idemitsu, Evaluation of thermal properties of  $\text{UO}_2$  and  $\text{PuO}_2$  by equilibrium molecular dynamics simulations from 300 to 2000 K, *J. Alloys Compd.* 400 (2005) 43–50.
- [33] S.I. Potashnikov, A.S. Boyarchenkov, K.A. Nekrasov, A.Y. Kupryazhkin, High-precision molecular dynamics simulation of  $\text{UO}_2$ – $\text{PuO}_2$ : Pair potentials comparison in  $\text{UO}_2$ , *J. Nucl. Mater.* 419 (2011) 217–225.
- [34] S.A. Taller, X.-M. Bai, Assessment of structures and stabilities of defect clusters and surface energies predicted by nine interatomic potentials for  $\text{UO}_2$ , *J. Nucl. Mater.* 443 (2013) 84–98.
- [35] E. Caglak, K. Govers, D. Lamoen, P.-E. Labeau, M. Verwerft, Atomic scale analysis of defect clustering and predictions of their concentrations in  $\text{UO}_2+x$ , *J. Nucl. Mater.* 541 (2020) 152403.
- [36] H. Balboa, L. Van Brutzel, A. Chartier, Y. Le Bouar, Assessment of empirical potential for MOX nuclear fuels and thermomechanical properties, *J. Nucl. Mater.* 495 (2017) 67–77.
- [37] T. Arima, K. Yoshida, T. Matsumoto, Y. Inagaki, K. Idemitsu, Thermal conductivities of  $\text{ThO}_2$ ,  $\text{NpO}_2$  and their related oxides: Molecular dynamics study, *J. Nucl. Mater.* 445 (2014) 175–180.

- [38] T. Uchida, T. Arima, K. Idemitsu, Y. Inagaki, Thermal conductivities of americium dioxide and sesquioxide by molecular dynamics simulations, *Comput. Mater. Sci.* 45 (2009) 229–234.
- [39] E. Caglak, P.E. Labeau, Lattice parameter of Am, Np bearing MOX fuel: An empirical potential study, *J. Phys. Commun.* 5 (2021).
- [40] J.K. Fink, Thermophysical properties of uranium dioxide, *J. Nucl. Mater.* 279 (2000) 1–18.
- [41] B.-T. Wang, P. Zhang, R. Lizárraga, I. Di Marco, O. Eriksson, Phonon spectrum, thermodynamic properties, and pressure-temperature phase diagram of uranium dioxide, *Phys. Rev. B.* 88 (2013) 104107.
- [42] I.J. Fritz, Elastic properties of UO<sub>2</sub> at high pressure, *J. Appl. Phys.* 47 (1976) 4353–4358.
- [43] J.B. Ainscough, Uranium Dioxide, in: R.J.B.T.-C.E. of A.C.M. BROOK (Ed.), Pergamon, Oxford, 1991: pp. 501–503.
- [44] P. Ruello, G. Petot-Ervas, C. Petot, L. Desgranges, Electrical conductivity and thermoelectric power of uranium dioxide, *J. Am. Ceram. Soc.* 88 (2005) 604–611.
- [45] P. Garcia, E. Pizzi, B. Dorado, D. Andersson, J.-P. Crocombette, C. Martial, G. Baldinozzi, D. Siméone, S. Maillard, G. Martin, A defect model for UO<sub>2+x</sub> based on electrical conductivity and deviation from stoichiometry measurements, *J. Nucl. Mater.* 494 (2017) 461–472.
- [46] K. Park, D.R. Olander, A defect model for the oxygen potential of urania, *High Temp. Sci.* 29 (1990) 203–222.
- [47] B.T.M. Willis, Crystallographic studies of anion-excess uranium oxides, *J. Chem. Soc. Faraday Trans. 2 Mol. Chem. Phys.* 83 (1987) 1073–1081.
- [48] D.A. Andersson, T. Watanabe, C. Deo, B.P. Uberuaga, Role of di-interstitial clusters in oxygen transport in UO<sub>2+x</sub> from first principles, *Phys. Rev. B.* 80 (2009) 60101.
- [49] D.A. Andersson, G. Baldinozzi, L. Desgranges, D.R. Conradson, S.D. Conradson, Density functional theory calculations of UO<sub>2</sub> oxidation: Evolution of UO<sub>2+x</sub>, U<sub>4</sub>O<sub>9–y</sub>, U<sub>3</sub>O<sub>7</sub>, and U<sub>3</sub>O<sub>8</sub>, *Inorg. Chem.* 52 (2013) 2769–2778.
- [50] B.T.M. Willis, The defect structure of hyper-stoichiometric uranium dioxide, *Acta*

- Crystallogr. Sect. A Cryst. Physics, Diffraction, Theor. Gen. Crystallogr. 34 (1978) 88–90.
- [51] A. Soulié, G. Baldinozzi, F. Garrido, J.-P. Crocombette, Clusters of Oxygen Interstitials in  $\text{UO}_{2+x}$  and  $\alpha\text{-U}_4\text{O}_9$ : Structure and Arrangements, *Inorg. Chem.* 58 (2019) 12678–12688.
- [52] L. Desgranges, G. Baldinozzi, D. Simeone, H.E. Fischer, Structural changes in the local environment of uranium atoms in the three Phases of  $\text{U}_4\text{O}_9$ , *Inorg. Chem.* 55 (2016) 7485–7491.
- [53] P.E. Blackburn, Oxygen dissociation pressures over uranium oxides, *J. Phys. Chem.* 62 (1958) 897–902.
- [54] S.A. Utlak, J.W. McMurray, Thermodynamic modeling of the  $\text{U}_3\text{O}_8\text{-x}$  solid solution phase, *J. Nucl. Mater.* 530 (2020) 151844.
- [55] S.T. Murphy, M.W.D. Cooper, R.W. Grimes, Point defects and non-stoichiometry in thorium, *Solid State Ionics.* 267 (2014) 80–87.
- [56] M.W.D. Cooper, S.T. Murphy, D.A. Andersson, The defect chemistry of  $\text{UO}_{2\pm x}$  from atomistic simulations, *J. Nucl. Mater.* 504 (2018) 251–260.
- [57] F. Bruneval, M. Freyss, J.-P. Crocombette, Lattice constant in nonstoichiometric uranium dioxide from first principles, *Phys. Rev. Mater.* 2 (2018) 23801.
- [58] A. Soulié, F. Bruneval, M.-C. Marinica, S. Murphy, J.-P. Crocombette, Influence of vibrational entropy on the concentrations of oxygen interstitial clusters and uranium vacancies in nonstoichiometric  $\text{UO}_2$ , *Phys. Rev. Mater.* 2 (2018) 83607.
- [59] J.M. Elorrieta, D. Manara, L.J. Bonales, J.F. Vigier, O. Dieste, M. Naji, R.C. Belin, V.G. Baonza, R.J.M. Konings, J. Cobos, Raman study of the oxidation in (U, Pu)  $\text{O}_2$  as a function of Pu content, *J. Nucl. Mater.* 495 (2017) 484–491.
- [60] D. Prieur, F. Lebreton, M. Caisso, P.M. Martin, A.C. Scheinost, T. Delahaye, D. Manara, Melting behaviour of americium-doped uranium dioxide, *J. Chem. Thermodyn.* 97 (2016) 244–252.
- [61] M. Chollet, R.C. Belin, J.-C. Richaud, M. Reynaud, Phase relationships in the U–Np–O system, *Procedia Chem.* 7 (2012) 472–476.
- [62] E. Epifano, O. Beneš, O.S. Vălu, J. Zappey, F. Lebreton, P.M. Martin, C. Guéneau,



- R.J.M. Konings, High temperature heat capacity of (U, Am)O<sub>2±x</sub>, *J. Nucl. Mater.* 494 (2017) 95–102.
- [63] J.-F. Vigier, P.M. Martin, L. Martel, D. Prieur, A.C. Scheinost, J. Somers, Structural investigation of (U<sub>0.7</sub>Pu<sub>0.3</sub>)O<sub>2-x</sub> mixed oxides, *Inorg. Chem.* 54 (2015) 5358–5365.
- [64] L. Martel, J.-F. Vigier, D. Prieur, S. Nourry, A. Guiot, K. Dardenne, J. Boshoven, J. Somers, Structural investigation of Uranium–Neptunium mixed oxides using XRD, XANES, and <sup>17</sup>O MAS NMR, *J. Phys. Chem. C.* 118 (2014) 27640–27647.
- [65] S. Plimpton, Fast parallel algorithms for short-range molecular dynamics, *J. Comput. Phys.* 117 (1995) 1–19.
- [66] J.D. Gale, GULP: A computer program for the symmetry-adapted simulation of solids, *J. Chem. Soc. Faraday Trans.* 93 (1997) 629–637.
- [67] K. Chen, P.J. Giblin, A. Irving, *Mathematical explorations with MATLAB*, Cambridge University Press, 1999.
- [68] P. Ewald, Evaluation of optical and electrostatic lattice potentials, *Ann. Phys.* 64 (1921) 253–287.
- [69] R.A. Buckingham, The classical equation of state of gaseous helium, neon and argon, *Proc. R. Soc. London. Ser. A. Math. Phys. Sci.* 168 (1938) 264–283.
- [70] N.-D. Morelon, D. Ghaleb, J.-M. Delaye, L. Van Brutzel, A new empirical potential for simulating the formation of defects and their mobility in uranium dioxide, *Philos. Mag.* 83 (2003) 1533–1555.
- [71] M.S.D. Read, S.R. Walker, R.A. Jackson, Derivation of enhanced potentials for plutonium dioxide and the calculation of lattice and intrinsic defect properties, *J. Nucl. Mater.* 448 (2014) 20–25.
- [72] P. Sindzingre, M.J. Gillan, A molecular dynamics study of solid and liquid UO<sub>2</sub>, *J. Phys. C Solid State Phys.* 21 (1988) 4017–4031.
- [73] T. Karakasidis, P. Lindan, A comment on a rigid-ion potential for UO<sub>2</sub>, *J. Phys. Condens. Matter.* 6 (1994) 2965.
- [74] R.A. Jackson, A.D. Murray, J.H. Harding, C.R.A. Catlow, The calculation of defect parameters in UO<sub>2</sub>, *Philos. Mag. A.* 53 (1986) 27–50.
- [75] C.B. Basak, A.K. Sengupta, H.S. Kamath, Classical molecular dynamics simulation of

- UO<sub>2</sub> to predict thermophysical properties, *J. Alloys Compd.* 360 (2003) 210–216.
- [76] Y. Li, T. Liang, S.B. Sinnott, S.R. Phillpot, A charge-optimized many-body potential for the U–UO<sub>2</sub>–O<sub>2</sub> system, *J. Phys. Condens. Matter.* 25 (2013) 505401.
- [77] D. Mbongo, R. Tétot, R. Ducher, R. Dubourg, N. Salles, Improved SMTB-Q model applied to oxygen migration and pressure phase transitions in UO<sub>2</sub>, *J. Phys. Condens. Matter.* 32 (2019) 95701.
- [78] P. Tiwary, A. Van De Walle, N. Grønbech-Jensen, Ab initio construction of interatomic potentials for uranium dioxide across all interatomic distances, *Phys. Rev. B - Condens. Matter Mater. Phys.* 80 (2009).
- [79] P. Tiwary, A. van de Walle, B. Jeon, N. Grønbech-Jensen, Interatomic potentials for mixed oxide and advanced nuclear fuels, *Phys. Rev. B.* 83 (2011) 94104.
- [80] C.R.A. Catlow, Energy Minimization Techniques in Materials Modeling, in: *Handb. Mater. Model.*, Springer, 2005: pp. 547–564.
- [81] M.P. Allen, D.J. Tildesley, *Computer simulation of liquids*, Oxford university press, 2017.
- [82] Y. Ma, P. Garcia, J. Lechelle, A. Miard, L. Desgranges, G. Baldinozzi, D. Simeone, H.E. Fischer, Characterization of Oxygen Defect Clusters in UO<sub>2+x</sub> Using Neutron Scattering and PDF Analysis, *Inorg. Chem.* 57 (2018) 7064–7076.
- [83] F.A. Kröger, H.J. Vink, Relations between the concentrations of imperfections in crystalline solids, in: *Solid State Phys.*, Elsevier, 1956: pp. 307–435.
- [84] S.-H. Kang, J.-H. Lee, H.-I. Yoo, H.S. Kim, Y.W. Lee, Non-stoichiometry, electrical conductivity and defect structure of hyper-stoichiometric UO<sub>2+x</sub> at 1000° C, *J. Nucl. Mater.* 277 (2000) 339–345.
- [85] B. Dorado, P. Garcia, G. Carlot, C. Davoisne, M. Fraczkiewicz, B. Pasquet, M. Freyss, C. Valot, G. Baldinozzi, D. Siméone, First-principles calculation and experimental study of oxygen diffusion in uranium dioxide, *Phys. Rev. B.* 83 (2011) 35126.
- [86] J. Wang, R.C. Ewing, U. Becker, Electronic structure and stability of hyperstoichiometric UO<sub>2+x</sub> under pressure, *Phys. Rev. B.* 88 (2013) 24109.
- [87] D.A. Andersson, J. Lezama, B.P. Uberuaga, C. Deo, S.D. Conradson, Cooperativity among defect sites in AO<sub>2+x</sub> and A<sub>4</sub>O<sub>9</sub> (A=U,Np,Pu): Density functional calculations,

- Phys. Rev. B - Condens. Matter Mater. Phys. 79 (2009) 1–12.
- [88] A. Zunger, S.-H. Wei, L.G. Ferreira, J.E. Bernard, Special quasirandom structures, *Phys. Rev. Lett.* 65 (1990) 353.
- [89] C. Takoukam-Takoundjou, E. Bourasseau, V. Lachet, Study of thermodynamic properties of U<sub>1-y</sub>Pu<sub>y</sub>O<sub>2</sub> MOX fuel using classical molecular Monte Carlo simulations, *J. Nucl. Mater.* 534 (2020) 152125.
- [90] B. Belbeoch, J.C. Boivineau, P. Perio, Changements de structure de l'oxyde U<sub>4</sub>O<sub>9</sub>, *J. Phys. Chem. Solids.* 28 (1967) 1267–1275.
- [91] E. Caglak, K. Govers, D. Lamoen, P.-E. Labeau, M. Verwerft, Atomic scale analysis of defect clustering and predictions of their concentrations in UO<sub>2+x</sub>, *J. Nucl. Mater.* 541 (2020). <https://doi.org/10.1016/j.jnucmat.2020.152403>.
- [92] S.G. Popov, J.J. Carbajo, G. Yoder, Thermophysical properties of MOX and UO<sub>2</sub> fuels including the effects of irradiation, *ORNL.* 27 (2000) 0–4.
- [93] H. Zhang, M.E. Huntelaar, R.J.M. Konings, E.H.P. Cordfunke, Melting behaviour of oxide systems for heterogeneous transmutation of actinides. II. The system MgO-Al<sub>2</sub>O<sub>3</sub>-PuO<sub>2</sub>, *J. Nucl. Mater.* 250 (1997) 83–87.
- [94] R. Böhler, M.J. Welland, F. De Bruycker, K. Boboridis, A. Janssen, R. Eloirdi, R.J.M. Konings, D. Manara, Revisiting the melting temperature of NpO<sub>2</sub> and the challenges associated with high temperature actinide compound measurements, *J. Appl. Phys.* 111 (2012) 113501.
- [95] A.D. Pelton, *Thermodynamics and phase diagrams of materials*, Mater. Sci. Technol. (2006).
- [96] T. Arima, K. Idemitsu, Y. Inagaki, Y. Tsujita, M. Kinoshita, E. Yakub, Evaluation of melting point of UO<sub>2</sub> by molecular dynamics simulation, *J. Nucl. Mater.* 389 (2009) 149–154.
- [97] M.W.D. Cooper, *Atomic scale simulation of irradiated nuclear fuel*, Imperial College London, 2015.
- [98] R. Freitas, M. Asta, M. De Koning, Nonequilibrium free-energy calculation of solids using LAMMPS, *Comput. Mater. Sci.* 112 (2016) 333–341.
- [99] R.P. Leite, M. de Koning, Nonequilibrium free-energy calculations of fluids using

- LAMMPS, *Comput. Mater. Sci.* 159 (2019) 316–326.
- [100] Y. Li, A fundamental understanding of the structures of oxygen defect clusters in  $\text{UO}_{2+x}$ ,  $\text{U}_4\text{O}_9$  and  $\text{U}_3\text{O}_7$ : from the perspective of Tetris cubes, *Acta Mater.* 194 (2020) 482–495.
- [101] J.-P. Crocombette, D. Torumba, A. Chartier, Charge states of point defects in uranium oxide calculated with a local hybrid functional for correlated electrons, *Phys. Rev. B.* 83 (2011) 184107.
- [102] S.D. Conradson, T. Durakiewicz, F.J. Espinosa-Faller, Y.Q. An, D.A. Andersson, A.R. Bishop, K.S. Boland, J.A. Bradley, D.D. Byler, D.L. Clark, Possible Bose-condensate behavior in a quantum phase originating in a collective excitation in the chemically and optically doped Mott-Hubbard system  $\text{UO}_{2+x}$ , *Phys. Rev. B.* 88 (2013) 115135.
- [103] S.I. Potashnikov, A.S. Boyarchenkov, K.A. Nekrasov, A.Y. Kupryazhkin, High-precision molecular dynamics simulation of  $\text{UO}_2\text{-PuO}_2$ : Anion self-diffusion in  $\text{UO}_2$ , *J. Nucl. Mater.* 433 (2013) 215–226.
- [104] F. Lebreton, D. Horlait, T. Delahaye, P. Blanchart, Fabrication and characterization of  $\text{U}_{1-x}\text{Am}_x\text{O}_{2\pm\delta}$  compounds with high americium contents ( $x=0.3, 0.4$  and  $0.5$ ), *J. Nucl. Mater.* 439 (2013) 99–102.
- [105] M.S. Talla Noutack, G. Jomard, M. Freyss, G. Geneste, Structural, electronic and energetic properties of uranium–americium mixed oxides  $\text{U}_{1-y}\text{Am}_y\text{O}_2$   $\text{U}_{1-y}\text{Am}_y\text{O}_2$  using DFT+ $\{\text{U}\}$ +U calculations, *J. Phys. Condens. Matter.* 31 (2019) 485501.

## 12. Annex (Paper I & II)

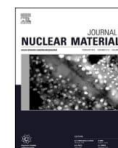
Journal of Nuclear Materials 541 (2020) 152403



Contents lists available at ScienceDirect

Journal of Nuclear Materials

journal homepage: [www.elsevier.com/locate/jnucmat](http://www.elsevier.com/locate/jnucmat)



### Atomic scale analysis of defect clustering and predictions of their concentrations in $\text{UO}_{2+x}$



Emre Caglak<sup>a, b, \*</sup>, Kevin Govers<sup>b, 1</sup>, Dirk Lamoen<sup>c</sup>, Pierre-Etienne Labeau<sup>a</sup>, Marc Verwerft<sup>b</sup>

<sup>a</sup> Université Libre de Bruxelles, Service de Métrologie Nucléaire, CP 165/84, 50 Av. F.D. Roosevelt, 1050, Brussels, Belgium

<sup>b</sup> Belgian Nuclear Research Centre, SCK CEN, Nuclear Materials Science Institute, Boeretang 200, 2400, Mol, Belgium

<sup>c</sup> EMAT, Department of Physics, Universiteit Antwerpen, Groenenborgerlaan 171, 2020, Antwerpen, Belgium

#### HIGHLIGHTS

- Oxygen interstitials ( $\text{O}_i$ ) and  $\text{O}_i$  clusters configurations in  $\text{UO}_{2+x}$  were predicted at EP level.
- Willis type split-di interstitial cluster configuration with effective charge –minus one– was found.
- Defect concentrations were evaluated through a Point Defect Model (PDM).
- PDM established from EP results shows good agreement with experimental data.

#### ARTICLE INFO

**Article history:**  
Received 6 March 2020  
Received in revised form 8 June 2020  
Accepted 14 July 2020  
Available online 6 August 2020

**Keywords:**  
Uranium dioxide  
Point defects  
Defect clustering  
Defect chemistry  
Deviation from stoichiometry

#### ABSTRACT

The physical properties of uranium dioxide vary greatly with stoichiometry. Oxidation towards hyperstoichiometric  $\text{UO}_2 - \text{UO}_{2+x}$  – might be encountered at various stages of the nuclear fuel cycle if oxidative conditions are met; the impact of stoichiometry changes upon physical properties should therefore be properly assessed to ensure safe and reliable operations. These physical properties are intimately linked to the arrangement of atomic defects in the crystalline structure. The evolution of the defect concentration with environmental parameters – oxygen partial pressure and temperature – were evaluated by means of a point defect model where the reaction energies are derived from atomic-scale simulations. To this end, various configurations and net charge states of oxygen interstitial clusters in  $\text{UO}_2$  have been calculated. Various methodologies have been tested to determine the optimum cluster configurations and a rigid lattice approach turned out to be the most useful strategy to optimize defect configuration structures. Ultimately, results from the point defect model were discussed and compared to experimental measurements of stoichiometry dependence on oxygen partial pressure and temperature.

© 2020 Elsevier B.V. All rights reserved.

#### 1. Introduction

Over the past decades, uranium dioxide ( $\text{UO}_2$ ) has been the reference fuel for the current fleet of nuclear reactors (Gen-II and Gen-III); today it is also considered by the Gen-IV International Forum for the first cores of the future generation of nuclear reactors on the roadmap towards minor actinide (MA) based fuel

technology [1]. Thermodynamic and transport properties of  $\text{UO}_2$  are a strong function of non-stoichiometry. Although a remarkable number of studies has been performed to address the relationship between the material properties and oxygen defects in  $\text{UO}_{2+x}$ , the fascinating complexity of these defects calls for further investigations [2–7].

It is widely known that the  $\text{UO}_2$  lattice can host a large number of oxygen defects in various charge states and configurations, for example, by clustering with electronic defects, both electrons and holes; the only experimentally proven defect configuration is the di-interstitial cluster derived from neutron diffraction measurements by Willis [8]. Computer simulations techniques can help to get insight into these defect structures, considering that they can be

\* Corresponding author. Université Libre de Bruxelles, Service de Métrologie Nucléaire, CP 165/84, 50 av. F.D. Roosevelt, 1050, Brussels, Belgium.

E-mail addresses: [emre.caglak@ulb.ac.be](mailto:emre.caglak@ulb.ac.be), [emrecaglak@gmail.com](mailto:emrecaglak@gmail.com) (E. Caglak).

<sup>1</sup> Now at Federal Agency for Nuclear Control – FANC (Belgium).

addressed by density functional theory (DFT) or empirical potentials (EP) [9–14]. For such investigations it is of paramount importance to gain quantitative knowledge of the defect concentrations as a function of environmental conditions, that is, temperature and oxygen potential (or oxygen partial pressure). This knowledge is provided by a point defect model (PDM) in which the chemical defect reactions are evaluated via a mass action law [15,16]. From that model, deviation from stoichiometry  $x$  in  $\text{UO}_{2+x}$  can be derived, which is also experimentally accessible.

Recent theoretical works, for example, Murphy et al. evaluated point defect concentrations and non-stoichiometry in thoria using DFT to predict the defect formation energies [17]. A similar approach adopted for uranium oxide by Cooper et al. [9], Soulié et al. [18], and Bruneval et al. [19] extended the  $\text{UO}_2$  study by adding oxygen defect clusters in their model. Even though, their results qualitatively provide a comparable defect concentration trend, the quantitative understanding still suffers from inconsistencies. This is mainly because of the various approximations used for the descriptions of the strong correlation between uranium  $f$  electrons, which in turn affects the defect formation energies. Unlike the above mentioned studies, we investigated the oxygen clusters up to di-interstitial by means of empirical potential simulations in expectation of qualitative agreement between DFT and EP. The positive results then further motivated us to go through a qualitative validation against measurements of stoichiometry dependence on oxygen partial pressure and temperature. In the future this will also allow us to discuss the solubility of different fission products and dopants in the  $\text{UO}_2$  matrix at EP level.

## 2. Methods

### 2.1. Atomic scale simulations

Atomic scale simulations were performed using the LAMMPS software, version 2017 [20]. Calculations consider atoms as point-wise charged particles interacting with each other through interatomic potentials. These calculations were complemented with the GULP software in view of its ability to compute defect energies with different methods [21]. In order to maintain coherence, the system defect energy calculations were performed using the same interatomic potentials with both codes.

Several sets of parameters have been derived in the open literature to describe atom interactions for the  $\text{UO}_2$  system [22,23]. They differ in the degree of covalence, or ionicity  $\xi$ , with ( $0 < \xi \leq 1$ ), attributed to ions and the analytical expression used for the short-range atom interactions. Most potentials are variants of the Buckingham potential form [24], sometimes coupled to a Morse term [25] to describe covalent bounds. The commonly adopted expression for the pair potential between ions  $i$  and  $j$  separated by distance  $r_{ij}$  takes the following form:

$$V(r_{ij}) = \frac{(\xi e)^2 Z_i Z_j}{4\pi\epsilon_0 r_{ij}} + A_{ij} \exp\left(-\frac{r_{ij}}{\rho_{ij}}\right) - \frac{C_{ij}}{r_{ij}^6} + D_{ij} \left[ \exp\left(-2\gamma_{ij}\left(r_{ij}^* - r_{ij}\right)\right) - 2 \exp\left(-\gamma_{ij}\left(r_{ij}^* - r_{ij}\right)\right) \right] \quad (1)$$

The first term stands for the electrostatic interaction between point charges with  $\epsilon_0$ , the vacuum permittivity. For  $\text{UO}_2$ , one considers full ionicity:  $Z(\text{U}^{4+}) = +4$  and  $Z(\text{O}^{2-}) = -2$ . Classical Ewald summation techniques were used to handle long-range electrostatic interactions in three dimensions. The second term of Eq. (1) expresses the short-range repulsion of overlapping electronic shells and the third term expresses the van der Waals attraction as a simple inverse power function. The last term is a Morse function

that represents the covalent bond of the uranium-oxygen pairs. Pairwise interactions were evaluated up to a cut-off distance of 1.1 nm. The system configuration was relaxed at constant volume until a convergence of  $10^{-4}$  eV is reached (total energy difference between consecutive minimisation steps).

Earlier studies revealed that the predictive character of empirical interatomic potentials for mechanical, thermal or defect properties of  $\text{UO}_2$  are quite challenging, as there is no universal set of parameters [23,26–28]. While these studies generally addressed absolute values, the present work rather focuses on relative values, such as defect binding energies, for which better agreement was observed between interatomic potential parameter sets [29]. The Yakub potential has been extensively tested in literature for both static and dynamic calculations, and reproduces reasonably well defect and thermo-mechanical properties of  $\text{UO}_2$  [12,30,31]. This potential was therefore selected for this study; its short range parametrization is reported in Table 1.

In  $\text{UO}_2$ , hole electronic defects are generally thought to maintain the system charge neutral [32]. In the present study, holes were described as localised on the uranium sublattice as uranium atoms with a (5+) charge. For the description of interactions involving those particles the atom charge ( $Z$ ) is simply modified while respecting the ionicity proposed in the original model – see Eq (1). Modifications of the short-range interactions were considered as a second order effect and were not applied for this study [29,33,34].

### 2.2. Defect calculations

Defect calculations were performed according to the supercell method, with LAMMPS [20], where a pristine system of  $4 \times 4 \times 4$  conventional  $\text{UO}_2$  unit-cells under periodic boundary conditions was considered as a starting structure [22]. The lattice parameter was set to the experimental value for  $\text{UO}_2$ , 0.547 nm [35], before relaxation. Defects were introduced in the system, which is then relaxed to find the energy minimum, and the corresponding atomic configuration.

Reaction energies are based on the system energy difference between the individual products and reactants. One must remain careful when interpreting the as-calculated energies in empirical potential calculations, as only energy differences between systems having an identical set of particles have a straightforward, physical, meaning. For the defect calculations that do not preserve the stoichiometry of the pristine material – where particles of one or several species<sup>1</sup> appear in or disappear from the system – the calculated defect energy implicitly takes, as a reference state for that particle, the non-interacting, charged, particle in vacuum. For example, in the case of an oxygen interstitial defect, the reference states consist of the pristine  $\text{UO}_2$  crystal on the one hand, and a charged  $\text{O}^{2-}$  in vacuum on the other hand. The latter configuration is purely conceptual in the empirical potential method, as the second electron captured actually remains unbound in vacuum.

To overcome this issue, one focuses here on stoichiometric defect reactions (that conserve the species), so that the corrections for particle addition and removal cancel out. Coming back to our example, neither the as-calculated oxygen interstitial energy, neither the opposite defect – the oxygen vacancy – energy, have a physical meaning. However, when combining the results, one obtains the oxygen Frenkel pair energy. In order to facilitate the construction of a point defect model from empirical potential calculations, one privileges defect reactions expressing the formation of defect clusters from their individual components, i.e. evaluating the free energy change.

<sup>1</sup> one also considers here atoms with different charges as different species.

**Table 1**  
Short range parametrization of Yakub et al. [12], and  $\xi = 0.5552$

ion pairs	$A_{ij}$ (eV)	$\rho_{ij} \times 10^{-10}$ (m)	$C_{ij} \times 10^{-60}$ (eV m <sup>6</sup> )	$D_{ij}$ (eV)	$\gamma_{ij} \times 10^{10}$ (m <sup>-1</sup> )	$r_{ij}^* \times 10^{-10}$ (m)
U <sup>4+</sup> – O <sup>2-</sup>	432.18	0.3422	0.0	0.5055	1.864	2.378
U <sup>4+</sup> – U <sup>4+</sup>	187.03	0.3422	0.0	0.0	–	–
O <sup>2-</sup> – O <sup>2-</sup>	883.12	0.3422	3.996	0.0	–	–

At EP level, issues remain for some of the reactions considered in the PDM, (see § 2.4); for example the formation of an electron-hole pair, for which the electron and hole tend to be localised on the uranium sublattice. The creation of the pair implies the disappearance of two regular U<sup>4+</sup> atoms, and the apparition of one U<sup>3+</sup> and one U<sup>5+</sup> atom and, hence, a species change from empirical potential simulation perspectives. Empirical pair-potentials results need to be corrected for the difference in ionization energy between U<sup>3+</sup> and U<sup>5+</sup>, for example following a Born-Haber cycle [36]. Alternatively, a value derived from experiment [37] or *ab initio* calculations [38] could be used for the defect reaction energy.

For the system oxidation reaction, no proper correction scheme exists, as it would involve the calculation of an O<sub>2</sub> molecule. The latter state is far from the validation domain of the empirical potentials used, considering that they were developed to address ceramic crystals. For that reaction, energies derived from experiment [39] or *ab initio* calculations would be a better alternative [14].

The supercell method can be applied to a charged system, such as for defect calculations. A neutral system is recovered by adding a uniform background charge to the system [40], whereas this correction is not implemented in LAMMPS. This background charge does not affect interatomic forces and simply results into an additional term to the system total energy. At post-processing, defect energies are then corrected for the charge's Madelung energy to the infinite dilution limit according to the potential predictions:  $f^\infty = f^L + \frac{q^2\alpha}{2\epsilon L}$  where  $f^\infty$  and  $f^L$  is a formation energy of the defect at infinite dilution and under periodic boundary conditions with total system size  $L$  ( $=0.544 \times 4$  nm after relaxation of the pristine system),  $q$  is the total charge on the solid,  $\alpha$  ( $=2.84$ ) is the cubic system Madelung constant and  $\epsilon$  ( $=3.28$ , for Yakub [12] potential) is the static dielectric constant.

### 2.3. Exploration of configuration space

The charge state of oxygen interstitials (O<sub>i</sub>) and O<sub>i</sub> clusters is evaluated in this empirical potential study. One also considers the presence of charge-compensating holes that would be bound to the defect. The exploration of the arrangement of holes around a single oxygen interstitial defect, or an oxygen interstitials cluster, is a difficult task, considering that the number of cases to be addressed increases in a combinatorial way with the number of holes considered:  $\frac{N!}{(N-n)!n!}$  with  $N$ , the number of accessible sites (256) for a  $4 \times 4 \times 4$  unit-cell system, and  $n$ , the number of U<sup>5+</sup> inserted in the system. In order to optimize the calculation time, several methods were tested.

- The brute force approach, used as a reference, where all possible combinations are relaxed and compared in terms of energy. The method only performs in a reasonable amount of time for up to three U<sup>5+</sup> in the system ( $\sim 2.7 \times 10^6$  combinations).
- A Monte-Carlo approach was then tested, similar to former works [41–43], where U<sup>5+</sup> are only displaced when the energy gain after the displacement obeys an acceptance (Metropolis) criterion. The major issue with this approach is that one generally starts from a relaxed configuration, so that the permutation of an U<sup>5+</sup> and an U<sup>4+</sup> ions most often results in a

positive energy gain. Although well-thought criteria enable to progressively converge towards lower energy configurations, convergence to the energy minimum is slow and not guaranteed.

- A rigid lattice approach, where one considers that the non-relaxed and the relaxed configuration maps are qualitatively similar. The search for the optimal configuration is performed in the non-relaxed system (1st stage) and the optimal configuration is relaxed (2nd stage). By doing so, one avoids repeated relaxation stages, which each necessitate of the order of 100–1000 calculation steps. The relaxed configuration energy is only calculated once, for the optimal configuration. Although the method could be used in brute-force scheme, the interest also lies in coupling it to a Monte-Carlo algorithm; the fact that non-relaxed configurations are used eliminates the energy gain issue evoked previously when permuting U<sup>5+</sup> with U<sup>4+</sup> ions.

The latter approach was validated for the clustering of a single oxygen interstitial with one and two holes and compared to a brute force approach. Both methods converged towards the same geometrical arrangement. In the case of a single hole, the hole is predicted to occupy a first nearest neighbour position relative to the oxygen interstitial. With two holes, the predicted configuration of minimum energy consisted of the holes located in second nearest neighbour positions to the oxygen interstitial, as illustrated by the mapping in Fig. 1. They were located in opposite directions from each other, as could be expected from pure electrostatic considerations; that configuration is also in good agreement with recent DFT calculations [44].

The systematic configuration space exploration confirmed that

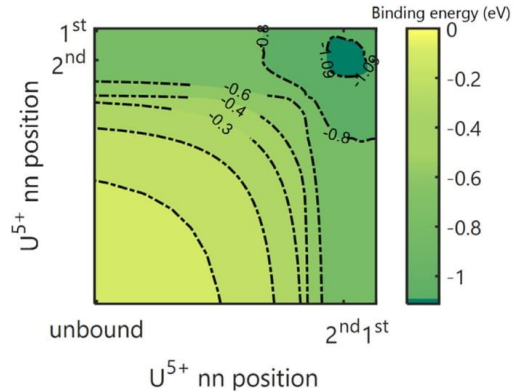


**Fig. 1.** Binding energy of two holes and an oxygen interstitial atom as predicted with Yakub potential [12]. The contour map expresses the binding energy as a function of the distance of each hole to the oxygen interstitial atom. When different configurations correspond to the same distances, the minimum value over these configurations is retained. The most stable configuration is observed for both holes located in second nearest neighbour to the oxygen interstitial, in opposite direction (along  $\langle 111 \rangle$  direction) from each other as it is shown in Fig. 2.

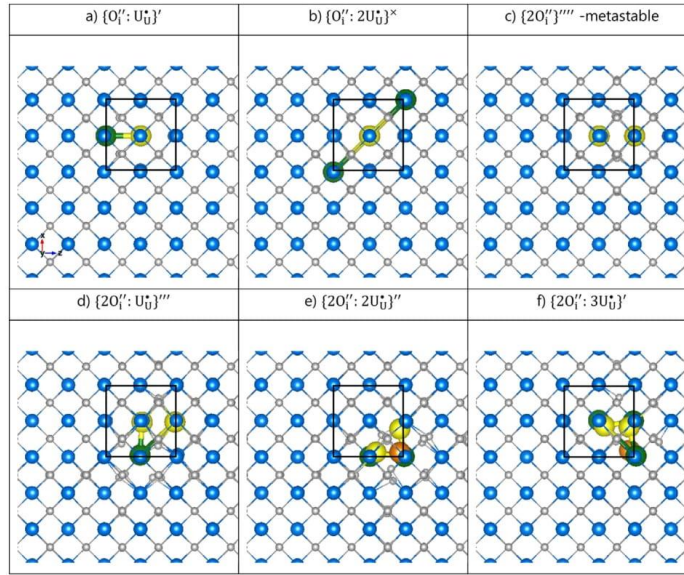


**Fig. 2.** Yakub potential relaxed configurations of oxygen interstitial and interstitial clusters [12]. Blue and white spheres represent the regular uranium and oxygen ions in *f.c.c.*  $\text{UO}_2$ . Yellow spheres stand for interstitial oxygen ions while the green ones for  $\text{U}^{5+}$  (holes) positions. For the case  $\{2\text{O}_i^{\bullet}; 2\text{U}_i^{\bullet}\}$  and  $\{2\text{O}_i^{\bullet}; 3\text{U}_i^{\bullet}\}$  orange spheres are used to highlight oxygen ions displaced from their regular positions. For the sake of clarity, central vacancy sites are not emphasized. (For interpretation of the references to colour in this figure legend, the reader is referred to the Web version of this article.)

the minimum energy configuration was indeed reached. The rigid lattice approach was thus observed to rapidly converge towards the optimal configuration found with the brute approach method. Based on the computing time gain and efficiency performance – convergence to the energy minimum is observed after about 5000 Monte-Carlo swaps –, the method is expected to facilitate the search for optimum configurations when a larger number of defects are at play.

#### 2.4. Point defect model

A point defect model (PDM) expresses interactions (or reactions) between defects in a similar way as one treats chemical reaction equilibria. It links, for each reaction, the concentrations at equilibrium of the species involved. Although virtually any defect and defect reaction could be considered, the point defect model will only provide a good representation of a material if the dominant defects are included in the picture. In uranium dioxide, it is commonly accepted that the dominant defects relate to electronic and oxygen disorder [45,46]. The simplest description of  $\text{UO}_2$ , close to stoichiometry, expresses the polaron (electron-hole pair creation) and the oxygen Frenkel (oxygen vacancy – interstitial pair) equilibria. Using Kröger-Vink notations [15], these reactions can be expressed, respectively as:



A relation between defect concentrations may then be expressed according to the mass action law which involves the

change in free energy of the system  $\Delta f$ :

$$K_D = \frac{[\text{U}_i^{\bullet}][\text{U}_i^{\bullet}]}{[\text{U}_i^{\bullet}]^2} = \exp\left(-\frac{\Delta f^D}{k_B T}\right) \quad (4)$$

$$K_F = \frac{[\text{O}_i^{\bullet}][v_o^{\bullet\bullet}]}{[\text{O}_o^{\times}][v_i^{\times}]} = \exp\left(-\frac{\Delta f^F}{k_B T}\right) \quad (5)$$

where  $[\text{U}_i^{\bullet}]$  and  $[\text{U}_i]$  are the concentration of holes and electrons assumed in the valence and conduction band, respectively [47].  $[\text{O}_i^{\bullet}]$  represents the interstitial oxygen concentration while  $[v_o^{\bullet\bullet}]$  is the oxygen vacancy concentration. This simple system expressed by Eqs. (2) and (3) contains seven unknowns and needs to be closed by other relations that express, for example, conservation of the site occupancy and of the system charge neutrality. In the infinite dilution limit, one may approximate regular atom concentrations by their value in a perfect crystal  $[\text{U}_i^{\bullet}] \approx [v_i^{\times}] \approx \frac{1}{2}[\text{O}_o^{\times}] \approx 1$  otherwise the relative contribution of each defect to uranium, oxygen and interstitial lattices should be summed up. The charge neutrality condition for defects (i) with a concentration  $C_i$  and net charge  $q_i$  must be maintained:

$$\sum_i q_i C_i = 0 \quad (6)$$

One last relation is required, which links the system to the constraints imposed by the environment. For  $\text{UO}_2$ , we consider that the oxidation reaction from the atmosphere surrounding the system dominates. The point defect reaction is expressed as:

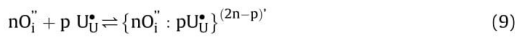




Or, in mass action law form:

$$K_O = \frac{[O_i''] [U_{ij}^*]^2}{[U_{ij}^*]^2 [v_i^x] \sqrt{p_{O_2}}} = \exp\left(-\frac{\Delta f^O}{k_B T}\right) \quad (8)$$

where  $p_{O_2}$  stands for the surrounding oxygen partial pressure. The deviation from stoichiometry  $x$ , in a regime dominated by isolated oxygen interstitials and holes, follows  $\propto p_{O_2}^{1/6}$ . This simple description of defects in  $UO_2$ , however, does not correspond to what is experimentally observed at larger deviation from stoichiometry; it has been evidenced that a better picture is provided if the clustering of oxygen interstitials is accounted in the model, as the observed relation rather obeys  $x \propto p_{O_2}^{1/2}$  [48–50]. One therefore introduces oxygen interstitial clusters with varying effective charges in the point defect model. Changes in the defect cluster charge were modelled in this work through the presence of localised holes on the uranium site. Assuming that a single individual oxygen interstitial cluster species dominates, in the form of  $\{nO_i'' : pU_{ij}^*\}^{(2n-p)}$  – with  $n$ , the number of oxygen interstitials and  $p$ , the number of holes in the cluster – the corresponding power dependency for the charge neutral system could be generalised as  $x \propto p_{O_2}^m$ , with the exponent  $m = \frac{n}{2(2n-p+1)}$ . For example, in the case of isolated  $O_i''$  ( $n = 1, p = 0$ ) one comes back to the first case and  $m = \frac{1}{6}$ ; this situation is expected to dominate close to perfect stoichiometry when clustering is not favourable for configurational entropy reasons. Experimentally, one observes a domain where the power dependency of  $x$  goes as  $p_{O_2}^{1/2}$ ; this observation would be compatible with two clusters of limited size:  $\{O_i'' : 2U_{ij}^*\}^x$  ( $n = 1, p = 2$ ) or  $\{2O_i'' : 3U_{ij}^*\}^y$  ( $n = 2, p = 3$ ). Stoichiometry measurements can not distinguish between the two types of clusters. Electrical conductivity will, however, be sensitive to the type of defect, since the latter defect cluster type needs to be compensated by non-bound holes, which are mobile, while the former cluster type is fully charge compensated. Several authors have proposed to consider singly charged di-interstitial clusters as the dominant defect at moderate departures from stoichiometry [48–50]. This leads to:



$$K_{cls.} = \frac{[\{nO_i'' : pU_{ij}^*\}^{(2n-p)}]}{[O_i'']^n [U_{ij}^*]^p} = \exp\left(-\frac{\Delta f^{cls.}}{k_B T}\right) \quad (10)$$

If one assumes that next to isolated point defects, only di-interstitial clusters with charge  $-1$  are formed, the site balances may be expressed as:

$$[U_{ij}^x] + [U_{ij}^*] + [U_{ij}] = 1 \quad (11)$$

$$[O_i^x] + [v_o^{**}] = 2 \quad (12)$$

$$[v_i^x] + [O_i''] + (2+a)[\{2O_i'' : 3U_{ij}^*\}^1] = 1 \quad (13)$$

The parameter  $a$  is used here for  $\{2O_i'' : 3U_{ij}^*\}^1$  or Willis clusters to restrict access to neighbour interstitial sites. Using  $a \approx 6$  also enables to reproduce  $UO_{2+x}$  saturation at  $x = 0.25$ , i.e. a

stoichiometry corresponding to  $U_4O_{10}$ . The PDM system of equations is solved with a Newton-Raphson iterative technique, ensuring numerical convergence is obtained. The deviation from stoichiometry is then evaluated from the various defect concentrations, considering that defects on the uranium sub-lattice play a negligible role:

$$x = \left| \sum [n\{nO_i'' : pU_{ij}^*\}^{(2n-p)}] \right| - [v_o^{**}] \quad (14)$$

### 3. Results and discussions

#### 3.1. Oxygen interstitial clusters configuration and energy

The configuration and the defect energy was calculated for various cluster of oxygen interstitials and holes by means of the rigid lattice approach to determine the lowest energy structure (cf. §2.3). All the defect configurations were rendered in Fig. 2 and defect energies were listed in Table 2.

Clusters involving a single oxygen interstitial and one or two holes has already been addressed in § 2.3. While the single hole is predicted to bind as first nearest neighbour to the oxygen interstitial, the most stable defect arrangement with two holes consists of these holes located in second nearest neighbour positions to the oxygen interstitial, in opposite directions from each other. That configuration is in agreement with DFT calculations [44].

Di-interstitial clusters were studied here as charge-compensated clusters, with one to four holes. The most stable arrangement of two oxygen interstitial atoms was first determined separately due to it exhibiting a metastable state; the presence of charge-compensating holes was considered in a second stage; two oxygen interstitials were initially placed in two nearest octahedral interstitial site with a separation of  $\frac{\sqrt{2}}{2}$  times lattice parameter. Fig. 2 shows the optimal arrangement of two oxygen interstitials  $\{2O_i''\}^{**}$ , as predicted in this study. We then investigated complex di-interstitial defect clusters with varying charges  $\{2O_i'' : pU_{ij}^*\}^{(4-p)}$ .

For a single charge-compensating hole  $\{2O_i'' : U_{ij}^*\}^{**}$ , the most stable configuration consists of the hole located on one of the closest neighbours of the oxygen interstitials. The structure of the  $\{2O_i'' : 2U_{ij}^*\}$  and  $\{2O_i'' : 3U_{ij}^*\}$  clusters, however, do not correspond to the traditional description from Willis, with two regular oxygen atoms displaced from their regular position [8]. While uranium ions are not displaced from their regular fluorite location, an alternative arrangement of the oxygen atoms was predicted here, where oxygen atoms stabilize as a split di-interstitial  $\{3O_i'' : v_o^{**}\}$ . In such a configuration, oxygen ions are arranged as a regular triangle, with positions along  $\langle 111 \rangle$  directions from a central oxygen vacancy. This structure, with a single oxygen atom displaced from its regular position was also derived in DFT calculations [38].

Our study predicted the progressive binding of the cluster as it accumulates one, two and three holes, but the neutral cluster, with 4 holes, tended to be less stable. Without further interpretation through a point defect model at this stage, this result already suggests that from pure energy perspectives, di-interstitial clusters of charge  $-1$  could be encountered, as often suggested from interpretation of experimental data through point defect models. The results also suggest a low probability of forming neutral di-interstitial clusters.

Once the most stable defect cluster configurations were obtained with LAMMPS [20], they were further analysed in terms of their energies with GULP [4]. Using the GULP code, the supercell method results were cross-checked with values derived using the

**Table 2**

Prediction of the defect clustering binding energy  $\Delta f^{cls}$ , in uranium dioxide calculated with  $4 \times 4 \times 4$  unit-cell method using Yakub potential [12]. Negative binding energy indicates preference for the cluster over its individual components.

Binding Energy	$\{O_i^- : U_{ij}^+\}$	$\{O_i^- : 2U_{ij}^+\}^{\times}$	$\{2O_i^{\times} : U_{ij}^+\}$	$\{2O_i^{\times} : U_{ij}^+\}^{\times}$	$\{2O_i^{\times} : 2U_{ij}^+\}$	$\{2O_i^{\times} : 3U_{ij}^+\}$
$\Delta f^{cls}$ [eV]	-0.67	-1.09	1.26	-0.12	-1.40	-2.09

Mott and Littleton approach [51]. The latter method divides the space around the defect into three regions; in region I atoms are fully relaxed, while in region IIa, only harmonic relaxation due to the defect charge is assumed; in Region IIb, an infinite purely dielectric medium is assumed. In this work, we used radii of 1.4 nm for region I and 2.8 nm for region IIa; very good agreement between both methods is generally reported [52,53] and also observed here. Results of binding energy calculations in the supercell approach are reported in Table 2.

### 3.2. Deviation from stoichiometry

Point defects energies were evaluated for  $UO_{2+x}$  (see in Table 2). They were complemented with a PDM in which the defect concentrations were derived from the reaction energies. We assume that the system of Eqs. (4), (5) and (8) dominates at exact stoichiometric composition and they may be solved analytically under the following assumptions:  $[O_i^-] = [v_{O_i}^{\times}]$ ,  $[U_{ij}^+] = [U_{ij}^{\times}]$  and the  $[U_{ij}^{\times}] \approx [v_{ij}^{\times}] \approx \frac{1}{2} [O_i^{\times}] \approx 1$ . For such a case,  $K_O$  is expressed as:

$$K_O = K_D \sqrt{\frac{2 \times K_F}{p_{O_2}}} \quad (15)$$

The oxygen partial pressure at exact stoichiometry  $p_{O_2}^*$ , suffers from large discrepancies between laboratories [35,48,54,55]. One of the reasons might be that the samples exhibit different impurity contents. Measurements performed by Leinders et al. [35], concluded that the relation found by Lindemer and Besmann's [54] data analysis gives the best agreement with their observations. In spite of the inconsistencies, we used the Lindemer and Besmann

**Table 3**

Comparison of calculated Frenkel pair  $\Delta f^F$  and oxidation reaction energy  $\Delta f^O$  at 0 K.

Formation Energy	This study	Other works
$\Delta f^F$ [eV]	4.1 +/- 0.1	3.0 to 4.6 [2,56]
$\Delta f^O$ [eV]	-0.4 +/- 0.01	-0.2 to -0.8 [3,6]

predictions for both  $p_{O_2}^*$  vs temperature (T) and the x in  $UO_{2+x}$  vs  $p_{O_2}^*$  [54]. This allows us to implicitly handle the defect vibrational entropies as corrections to  $K_O$ .

Another parameter appearing in Eq. (15) is  $K_D$  which is related to the band gap energy. *Ab initio* calculations and experiments generally agree on the band gap width – the energy to form an electron in the conduction band and a hole in the valence band –, with  $\Delta f^D = 2.1 +/- 0.1$  eV [37,38].

It was observed that reaction constant  $K_O$  in Eq. (15) is ultimately linked to the precision of  $K_F$ ,  $p_{O_2}^*$  and  $K_D$ . Any changes in those parameters would significantly affect the overall defect concentrations. Two recent studies report and discuss inconsistencies between the Frenkel pair energy –related to  $K_F$  – derived from atomic scale simulations and experiments [22,31]. One reports an experimental range of 3–4.6 eV [2,56] while atomistic simulations (both *ab initio* and EP) generally predict slightly higher values, i.e. between 3 and 7 eV [22,31,57]. The Yakub potential provides a value of 5.7 eV [12].

In a first phase, the stoichiometric deviation of  $UO_2$  was qualitatively evaluated. Eq. (15) was used to calculate  $K_O$  with the normalised pressure at exact stoichiometry i.e.  $p_{O_2} / p_{O_2}^* = 1$ . Results presented in Fig. 3 show that isolated oxygen interstitials  $O_i^{\times}$

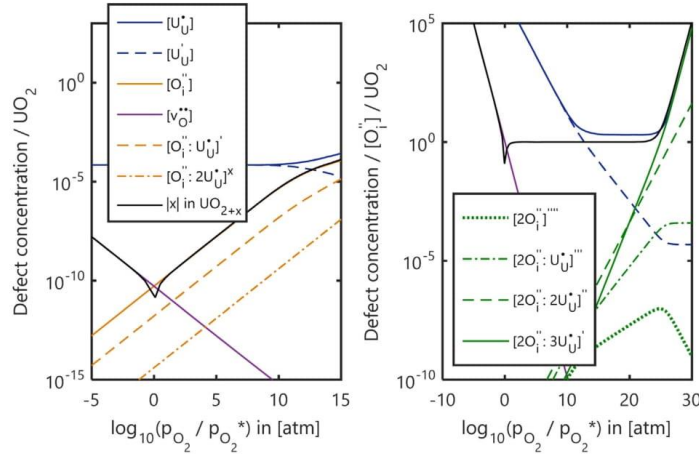


**Fig. 3.** Qualitative evaluation of defect concentrations in  $UO_{2+x}$  predicted by Yakub potential [12]. Left) represents the single interstitial clustering concentrations and Right) is di-interstitial clustering concentrations over the normalised oxygen pressure range at 1273 K.

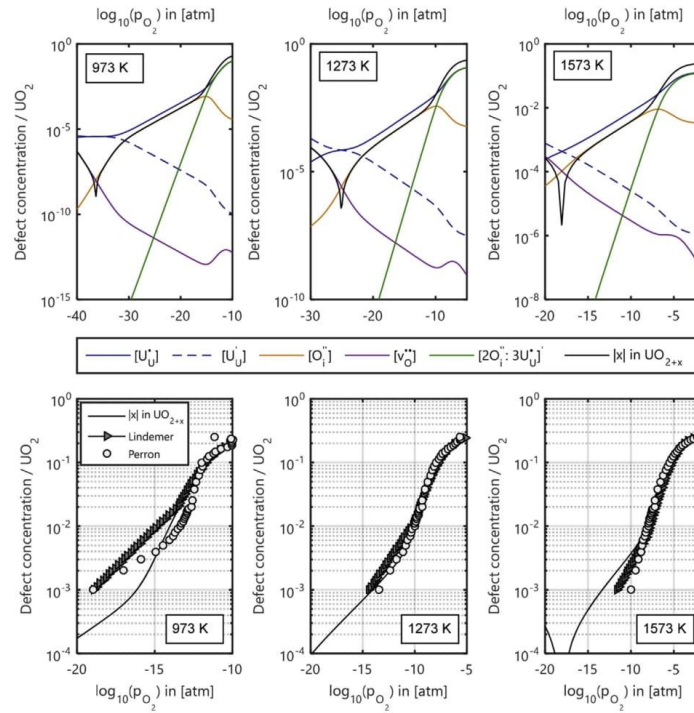


Fig. 4. The deviation from stoichiometry  $x$  in  $UO_{2+x}$  (bottom row) is calculated from the defect concentrations over a range of temperatures (top row). Comparison is made with the correlations published by Lindemer and Besmann [54], and Perron's thermodynamic data [55].

dominate at lower oxygen partial pressure region in  $UO_{2+x}$ . No significant contribution was observed from other types of single interstitial clusters, namely:  $\{O_i^+ : U_j^0\}$  and  $\{O_i^+ : 2U_j^0\}^x$ . The general concentration trend for single interstitial clusters at lower partial pressure  $[O_i^+] > \{O_i^+ : U_j^0\} > \{O_i^+ : 2U_j^0\}^x$  was determined which is also in line with the interpretation of DFT simulation results [9]. They all progressively saturate as one approaches  $x=0.07$ , considering that beyond that value, first neighbour sites would become populated; then oxygen interstitials cannot be considered as isolated anymore. In the case of di-interstitial clusters, the trend predicted at higher oxygen partial pressure is to observe single charge di-interstitial clusters dominating:  $\{2O_i^+ : 3U_j^0\} > \{2O_i^+ : 2U_j^0\} > \{2O_i^+ : U_j^0\} > \{2O_i^+\}$ . Therefore, once higher order clustering is a concern, non-formally charged defects were observed to dominate. Considering saturation of isolated oxygen interstitial clusters occurs at low departure from stoichiometry because of site exclusion – if a first neighbour site becomes occupied, a di-interstitial cluster is actually formed – one focuses on a relatively simple PDM made of isolated point defects and a single type of oxygen interstitials clusters  $\{2O_i^+ : 3U_j^0\}$ , which was predicted in this study to dominate at higher stoichiometry.

In a second phase, Eq. (15) was used to calculate  $K_O$  with the oxygen pressure at exact stoichiometry provided by Lindemer and Besmann [54]. We considered the general agreement on the band gap and on the overestimation of the Frenkel pair energy by

empirical potential simulations, which was described earlier. The dependence of  $K_O$  to  $K_F$  was also derived from the Lindemer and Besmann's work on the basis of Eq. (15) [54]. The calculated Frenkel pair energy  $\Delta f^F$ , and oxidation reaction energy  $\Delta f^O$  are reported in Table 3. These energies have been found to be in good agreement with literature values.

The defect concentrations as a function of oxygen partial pressure were computed at equilibrium for  $UO_{2+x}$  and presented at three different temperatures (see Fig. 4). The material stoichiometry was then derived from the oxygen defect balance. As illustrated in these Figures, the agreement for the departure from stoichiometry at approximately  $x \leq 0.01$  suffers from large uncertainties, which should be put into perspective with the large experimental uncertainty at these low values of  $x$ . At higher pressure, predictions on the  $x$  in  $UO_{2+x}$  fits well with the experimental data points show better agreement for the  $x$  in  $UO_{2+x}$ .

#### 4. Conclusions

The clustering behaviour of oxygen interstitials and holes is addressed by empirical potential based atomic scale simulations. The defect energies are then interpreted by mean of a PDM to derive the concentration of defects and defect clusters as a function of temperature and oxygen partial pressure.

A validation of the methodology and the results is conducted on the basis of the deviation from stoichiometry in  $UO_{2+x}$ .

The following results were achieved:

- Configurational space exploration of the arrangement of localised holes around isolated oxygen interstitials and oxygen interstitial clusters was shown to be most effective with a combination of a rigid lattice approach – where no relaxation is performed in a first stage – with a Metropolis Monte Carlo particle swapping method.
- The PDM established from EP results and experimental values which are not accessible to EP techniques shows good agreement with various sets of experimental data.
- With the proposed dominant defect type -  $\{2O_i^{\bullet} : 3U_{ij}^{\bullet}\}$ , di-interstitial with minus one charge-, the calculated relation between both stoichiometry and electrical conductivity evolution with oxygen partial pressure have a power dependence that corresponds to what was shown in experiments. Especially, at 1273 K and 1573 K good agreement between our model and experiments was achieved.
- At 973 K, both the experiments and the proposed model show slight inconsistencies. One might also consider that at low temperature  $UO_2$  exhibits a solid solution with  $U_4O_9$  in which the excess oxygen ions agglomerate into a cuboctahedron (CoT) structure [58–60]. Such a clustering configuration of higher order might dominate the deviation from stoichiometry in  $UO_{2+x}$  at low temperature. However, this statement is based solely on theoretical arguments and not supported by experimental data; it should therefore be addressed in future work.

#### CRedit authorship contribution statement

**Emre Caglak:** Conceptualization, Methodology, Software, Validation, Formal analysis, Investigation, Resources, Data curation, Writing - original draft, Writing - review & editing, Visualization.  
**Kevin Govers:** Conceptualization, Methodology, Writing - review & editing, Supervision.  
**Dirk Lamoen:** Conceptualization, Writing - review & editing, Supervision, Project administration, Funding acquisition.  
**Pierre-Etienne Labeau:** Conceptualization, Writing - review & editing, Supervision, Project administration, Funding acquisition.  
**Marc Verwerft:** Conceptualization, Writing - review & editing, Supervision, Project administration, Funding acquisition.

#### Declaration of competing interest

We certify that there are no financial, actual or potential conflicts of interest including any financial, personal or other relationships with other people or organizations within three years since beginning the submitted work that could inappropriately influence, or be perceived to influence, our work.

#### Acknowledgements

This work is dedicated to the memory of Prof. Alain Dubus, ULB, Bruxelles, Belgium. Financial support from the SCK CEN is gratefully acknowledged.

#### Appendix A. Supplementary data

Supplementary data to this article can be found online at <https://doi.org/10.1016/j.jnucmat.2020.152403>.

#### References

- [1] C. Behar, Technology Roadmap Update for Generation IV Nuclear Energy Systems, OECD Nucl. Energy Agency Gener. IV Int. Forum, 2014, pp. 2003–2014.
- [2] H. Matzke, Atomic transport properties in  $UO_2$  and mixed oxides (U, Pu)  $O_2$ ,

- J. Chem. Soc. Faraday Trans. 2 Mol. Chem. Phys. 83 (1987) 1121–1142.
- [3] A. Nakamura, T. Fujino, Thermodynamic analysis on point defects of  $UO_{2+x}$  at relatively small deviation from stoichiometry between 600 and 1400° C, J. Nucl. Mater. 140 (1986) 113–130.
- [4] IAEA, Thermodynamic and Transport Properties of Uranium Dioxide and Related Phases, 1965.
- [5] C. Guéneau, A. Chartier, L. Van Brutzel, Thermodynamic and Thermophysical Properties of the Actinide Oxides, 2012.
- [6] P. Garcia, E. Pizzi, B. Dorado, D. Andersson, J.-P. Crocombette, C. Martial, G. Baldinozzi, D. Siméone, S. Maillard, G. Martin, A defect model for  $UO_{2+x}$  based on electrical conductivity and deviation from stoichiometry measurements, J. Nucl. Mater. 494 (2017) 461–472.
- [7] D.A. Andersson, T. Watanabe, C. Deo, B.P. Uberuaga, Role of di-interstitial clusters in oxygen transport in  $UO_{2+x}$  from first principles, Phys. Rev. B 80 (2009) 60101.
- [8] B.T.M. Willis, The defect structure of hyper-stoichiometric uranium dioxide, Acta Crystallogr. Sect. A Cryst. Physics, Diffraction, Theor. Gen. Crystallogr. 34 (1978) 88–90.
- [9] M.W.D. Cooper, S.T. Murphy, D.A. Andersson, The defect chemistry of  $UO_{2+x}$  from atomistic simulations, J. Nucl. Mater. 504 (2018) 251–260.
- [10] P. Nerikar, T. Watanabe, J.S. Tulenko, S.R. Phillpot, S.B. Sinnott, Energetics of intrinsic point defects in uranium dioxide from electronic-structure calculations, J. Nucl. Mater. 384 (2009) 61–69.
- [11] R.A. Jackson, A.D. Murray, J.H. Harding, C.R.A. Catlow, The calculation of defect parameters in  $UO_2$ , Philos. Mag. A 53 (1986) 27–50.
- [12] E. Yakub, C. Ronchi, D. Staicu, Computer simulation of defects formation and equilibrium in non-stoichiometric uranium dioxide, J. Nucl. Mater. 389 (2009) 119–126.
- [13] C.R.A. Catlow, Point defect and electronic properties of uranium dioxide, Proc. R. Soc. London. A Math. Phys. Sci. 353 (1977) 533–561.
- [14] D.A. Andersson, G. Baldinozzi, L. Desgranges, D.R. Conradson, S.D. Conradson, Density functional theory calculations of  $UO_2$  oxidation: evolution of  $UO_{2+x}$ ,  $U_4O_9$ – $y$ ,  $U_3O_7$ , and  $U_3O_8$ , Inorg. Chem. 52 (2013) 2769–2778.
- [15] F.A. Kröger, H.J. Vink, Relations between the concentrations of imperfections in crystalline solids, in: Solid State Phys, Elsevier, 1956, pp. 307–435.
- [16] F.A. Kröger, The Chemistry of Imperfect Crystals, North-Holland Pub. Co., 1964.
- [17] S.T. Murphy, M.W.D. Cooper, R.W. Grimes, Point defects and non-stoichiometry in thoria, Solid State Ionics 267 (2014) 80–87.
- [18] A. Soulié, F. Bruneval, M.-C. Marinica, S. Murphy, J.-P. Crocombette, Influence of vibrational entropy on the concentrations of oxygen interstitial clusters and uranium vacancies in nonstoichiometric  $UO_2$ , Phys. Rev. Mater. 2 (2018) 83607.
- [19] F. Bruneval, M. Freyss, J.-P. Crocombette, Lattice constant in nonstoichiometric uranium dioxide from first principles, Phys. Rev. Mater. 2 (2018) 23801.
- [20] S. Plimpton, Fast parallel algorithms for short-range molecular dynamics, J. Comput. Phys. 117 (1995) 1–19.
- [21] J.D. Gale, GULP: a computer program for the symmetry-adapted simulation of solids, J. Chem. Soc. Faraday Trans. 93 (1997) 629–637.
- [22] K. Govers, S. Lemehov, M. Hou, M. Verwerft, Comparison of interatomic potentials for  $UO_2$ . Part I: static calculations, J. Nucl. Mater. 366 (2007) 161–177.
- [23] S.I. Potashnikov, A.S. Boyarchenkov, K.A. Nekrasov, A.Y. Kupryazhkin, High-precision molecular dynamics simulation of  $UO_2$ – $PuO_2$ : pair potentials comparison in  $UO_2$ , J. Nucl. Mater. 419 (2011) 217–225.
- [24] R.A. Buckingham, The classical equation of state of gaseous helium, neon and argon, Proc. R. Soc. London. Ser. A Math. Phys. Sci. 168 (1938) 264–283.
- [25] P.M. Morse, Diatomic molecules according to the wave mechanics. II. Vibrational levels, Phys. Rev. 34 (1929) 57.
- [26] K. Govers, S. Lemehov, M. Hou, M. Verwerft, Comparison of interatomic potentials for  $UO_2$ : Part II: molecular dynamics simulations, J. Nucl. Mater. 376 (2008) 66–77.
- [27] C.L. Bishop, R.W. Grimes, D.C. Parfitt, Establishing the isotropy of displacement cascades in  $UO_2$  through molecular dynamics simulation, Nucl. Instrum. Methods Phys. Res. Sect. B Beam Interact. Mater. Atoms 268 (2010) 2915–2917.
- [28] R. Devanathan, J. Yu, W.J. Weber, Energetic recoils in  $UO_2$  simulated using five different potentials, J. Chem. Phys. 130 (2009) 174502.
- [29] K. Govers, S.E. Lemehov, M. Verwerft, On the solution and migration of single Xe atoms in uranium dioxide—An interatomic potentials study, J. Nucl. Mater. 405 (2010) 252–260.
- [30] T. Arima, K. Idemitsu, Y. Inagaki, Y. Tsujita, M. Kinoshita, E. Yakub, Evaluation of melting point of  $UO_2$  by molecular dynamics simulation, J. Nucl. Mater. 389 (2009) 149–154.
- [31] S.I. Potashnikov, A.S. Boyarchenkov, K.A. Nekrasov, A.Y. Kupryazhkin, High-precision molecular dynamics simulation of  $UO_2$ – $PuO_2$ : anion self-diffusion in  $UO_2$ , J. Nucl. Mater. 433 (2013) 215–226.
- [32] A. Baena, T. Cardinaels, K. Govers, J. Pakarinen, K. Binnemans, M. Verwerft, Lattice contraction and lattice deformation of  $UO_2$  and  $ThO_2$  doped with  $Gd_2O_3$ , J. Nucl. Mater. 467 (2015) 135–143.
- [33] C.R.A. Catlow, Point defect and electronic properties of uranium dioxide, Proc. R. Soc. London A Math. Phys. Eng. Sci. 353 (1977) 533–561.
- [34] R. Ngayam-Happy, M. Krack, A. Pautz, Effects of stoichiometry on the defect clustering in uranium dioxide, J. Phys. Condens. Matter 27 (2015) 455401.
- [35] G. Leinders, T. Cardinaels, K. Binnemans, M. Verwerft, Accurate lattice parameter measurements of stoichiometric uranium dioxide, J. Nucl. Mater.

- 459 (2015) 135–142.
- [36] J.D. Lee, Concise Inorganic Chemistry, John Wiley & Sons, 2008.
- [37] J. Schoenes, Optical properties and electronic structure of  $\text{UO}_2$ , *J. Appl. Phys.* 49 (1978) 1463–1465.
- [38] J. Wang, R.C. Ewing, U. Becker, Average structure and local configuration of excess oxygen in  $\text{UO}_{2+x}$ , *Sci. Rep.* 4 (2014) 4216.
- [39] M.W. Finnis, A.Y. Lozovoi, A. Alavi, The oxidation of NiAl: what can we learn from ab initio calculations? *Annu. Rev. Mater. Res.* 35 (2005) 167–207.
- [40] M. Leslie, N.J. Gillan, The energy and elastic dipole tensor of defects in ionic crystals calculated by the supercell method, *J. Phys. C Solid State Phys.* 18 (1985) 973.
- [41] J.A. Ball, M. Pirzada, R.W. Grimes, M.O. Zacate, D.W. Price, B.P. Uberuaga, Predicting lattice parameter as a function of cation disorder in  $\text{MgAl}_2\text{O}_4$  spinel, *J. Phys. Condens. Matter* 17 (2005) 7621.
- [42] M.O. Zacate, R.W. Grimes, Combined Monte Carlo-energy minimization analysis of Al-Fe disorder in  $\text{Ca}_2\text{FeAlO}_5$  brownmillerite, *Philos. Mag. A* 80 (2000) 797–807.
- [43] M.O. Zacate, R.W. Grimes, Simulation of Al/Fe disorder in  $\text{Ca}_2\text{FeAl}_2-x\text{O}_5$ , *J. Phys. Chem. Solid.* 63 (2002) 675–683.
- [44] B. Dorado, P. Garcia, G. Carlot, C. Davoisne, M. Fraczkiewicz, B. Pasquet, M. Freyss, C. Valot, G. Baldinozzi, D. Siméone, First-principles calculation and experimental study of oxygen diffusion in uranium dioxide, *Phys. Rev. B* 83 (2011) 35126.
- [45] B.T.M. Willis, Crystallographic studies of anion-excess uranium oxides, *J. Chem. Soc. Faraday Trans. 2 Mol. Chem. Phys.* 83 (1987) 1073–1081.
- [46] Y. Ma, P. Garcia, J. Lechelle, A. Miard, L. Desgranges, G. Baldinozzi, D. Simeone, H.E. Fischer, Characterization of oxygen defect clusters in  $\text{UO}_{2+x}$  using neutron scattering and PDF analysis, *Inorg. Chem.* 57 (2018) 7064–7076.
- [47] A.R. Massih, Electronic transport in pure and doped  $\text{UO}_2$ , *J. Nucl. Mater.* 497 (2017) 166–182.
- [48] P. Ruello, G. Petot-Ervas, C. Petot, L. Desgranges, Electrical conductivity and thermoelectric power of uranium dioxide, *J. Am. Ceram. Soc.* 88 (2005) 604–611.
- [49] S.-H. Kang, J.-H. Lee, H.-I. Yoo, H.S. Kim, Y.W. Lee, Non-stoichiometry, electrical conductivity and defect structure of hyper-stoichiometric  $\text{UO}_{2+x}$  at  $1000^\circ\text{C}$ , *J. Nucl. Mater.* 277 (2000) 339–345.
- [50] K. Park, D.R. Olander, A defect model for the oxygen potential of urania, *High Temp. Sci.* 29 (1990) 203–222.
- [51] N.F. Mott, M.J. Littleton, Conduction in polar crystals. I. Electrolytic conduction in solid salts, *Trans. Faraday Soc.* 34 (1938) 485–499.
- [52] R.A. Jackson, J.E. Huntingdon, R.G.J. Ball, Defect calculations in solids beyond the dilute limit, *J. Mater. Chem.* 1 (1991) 1079–1080.
- [53] A. Walsh, A.A. Sokol, C.R.A. Catlow, Free energy of defect formation: thermodynamics of anion Frenkel pairs in indium oxide, *Phys. Rev. B* 83 (2011) 224105.
- [54] T.B. Lindemer, T.M. Besmann, Chemical thermodynamic representation of  $\text{UO}_{2+x}$ , *J. Nucl. Mater.* 130 (1985) 473–488.
- [55] P.O. Perron, THERMODYNAMICS OF NONSTOICHIOMETRIC URANIUM DIOXIDE, Atomic Energy of Canada Ltd., Chalk River (Ontario), 1968.
- [56] G.E. Murch, C.R.A. Catlow, Oxygen diffusion in  $\text{UO}_2$ ,  $\text{ThO}_2$  and  $\text{PuO}_2$ . A review, *J. Chem. Soc. Faraday Trans. 2 Mol. Chem. Phys.* 83 (1987) 1157–1169.
- [57] M. Bertolus, M. Freyss, M. Krack, R. Devanathan, Assessment of Current Atomic Scale Modelling Methods for the Investigation of Nuclear Fuels under Irradiation: Example of Uranium Dioxide, 2015.
- [58] J.D. Higgs, B.J. Lewis, W.T. Thompson, Z. He, A conceptual model for the fuel oxidation of defective fuel, *J. Nucl. Mater.* 366 (2007) 99–128.
- [59] D.J.M. Bevan, I.E. Grey, B.T.M. Willis, The crystal structure of  $\beta\text{-U}_4\text{O}_9$ , *J. Solid State Chem.* 61 (1986) 1–7.
- [60] R.I. Cooper, B.T.M. Willis, Refinement of the structure of  $\beta\text{-U}_4\text{O}_9$ , *Acta Crystallogr. Sect. A Found. Crystallogr.* 60 (2004) 322–325.



## PAPER

## OPEN ACCESS

## RECEIVED

29 November 2020

## REVISED

18 February 2021

## ACCEPTED FOR PUBLICATION

23 February 2021

## PUBLISHED

24 March 2021

Original content from this work may be used under the terms of the [Creative Commons Attribution 4.0 licence](https://creativecommons.org/licenses/by/4.0/).

Any further distribution of this work must maintain attribution to the author(s) and the title of the work, journal citation and DOI.



# Lattice parameter of Am, Np bearing MOX fuel: an empirical potential study

Emre Caglak<sup>1,2</sup> and Pierre-Etienne Labeau<sup>1</sup><sup>1</sup> Université Libre de Bruxelles, Service de Métrologie Nucléaire, CP 165/84, 50 av. F.D. Roosevelt, B-1050 Brussels, Belgium<sup>2</sup> Belgian Nuclear Research Centre, SCK CEN, Nuclear Materials Science Institute, Boeretang 200, B-2400 Mol, BelgiumE-mail: [emre.caglak@ulb.be](mailto:emre.caglak@ulb.be) and [emrecaglak@gmail.com](mailto:emrecaglak@gmail.com)**Keywords:** lattice parameter, MOX fuel, U- Pu -Am -Np -O system, rigid lattice method

## Abstract

An empirical potential study was performed for the americium (Am), neptunium (Np) containing uranium (U) and Plutonium (Pu) mixed oxides (MOX). The configurational space of a complex  $U_{1-y-y'-y''}Pu_yAm_{y'}Np_{y''}O_2$  system was predicted by the rigid lattice Monte Carlo method. Based on the computing time and efficiency performance, the method was found to rapidly converge towards the optimal configuration. From that configuration, the relaxed lattice parameter of Am, Np bearing MOX fuel was investigated and compared with available literature data. As a result, a linear behaviour of the lattice parameter as a function of Am, Np content was observed.

## 1. Introduction

Minor actinide [MA (Am, Np), mainly] bearing mixed oxide (MOX) is of interest for use as fuels for fast reactors (FR) and accelerator driven hybrid systems (ADS) [1]. The effect of MAs on the MOX properties, such as thermal conductivity, melting point and lattice parameter, is of paramount importance to the safe, reliable and sustainable operation. Among these material properties, lattice parameters are essential to obtain the theoretical density, which is used to ensure the quality of nuclear fuel during fabrication [2].

In recent studies, structural, elastic, thermodynamic and mechanical properties of actinide dioxides  $AnO_2$  ( $An = U, Pu, Am$  or  $Np$ ) and their binary mixtures have been treated extensively [3–14], concluding a linear relationship between lattice parameter and composition (Vegard's law) [15–22]. Compared to that, the availability of data on their complex ternary and quaternary oxide mixtures are, however, very limited. For the system U-Pu-Am-Np-O, for instance, it is reported that the stoichiometric complex  $U_{1-y-y'-y''}Pu_yAm_{y'}Np_{y''}O_2$  has a fluorite structure and that the lattice parameter exhibits a linear behaviour for a dilute (up to few at%) range of composition of MA, and maximum 60 at% Pu [23].

Atomic scale simulation techniques, both density functional theory (DFT) and empirical potentials (EP), are promising to evaluate complex oxide systems' properties. Although DFT-based models have been successfully applied to nuclear fuel, the first principles description of actinide f-electrons is a highly challenging and debated issue [24–26]. In contrast, empirical potentials are derived from fitting of the individual material's available properties, which can be used for the evaluation of mixed systems. Therefore, this study aims at investigating the lattice parameter of U, Pu, Am and Np mixed oxides as a function of atomic concentrations via EP methods.

The paper is organised based on the following steps: First, the lattice parameter of the simple oxides  $AnO_2$  ( $An = U, Pu, Am$  or  $Np$ ) was calculated as a pre-validation. Second, binary mixture oxides were modelled for various concentrations of actinides in the host  $UO_2$  matrix. The lattice configuration was predicted via a systematic optimization method called rigid lattice method [27]. From that configuration, relaxed system energies and lattice parameters were investigated as a function of composition. Then, the assessment was extended to complex  $U_{1-y-y'}Pu_yAm_{y'}O_2$  and  $U_{1-y-y'-y''}Pu_yAm_{y'}Np_{y''}O_2$  systems. Finally, the results of this study were compared to the available experimental data and as well as to the standard ionic radii model.

**Table 1.** Parameters for Busing-Ida type interatomic potential function, as parametrized by Arima *et al* [31–33].

Ion	$a_i$ (nm)	$b_i$ (nm)	$c_i$ ( $J^{-0.5}nm^3 mol^{-0.5}$ )	References
U <sup>4+</sup>	0.1318	0.0036	0.0	[32]
Pu <sup>4+</sup>	0.1272	0.00325	0.0	[32]
Am <sup>4+</sup>	0.1282	0.00373	0.0	[31]
Np <sup>4+</sup>	0.13148	0.0039	0.0	[33]
O <sup>2-</sup>	0.1847	0.0166	1.294	[36, 37]

## 2. Techniques

### 2.1. Atomic scale simulations

Atomic scale simulations were performed according to the supercell method, using the large-scale atomic/molecular massively parallel simulator (LAMMPS) version 2020 [28]. A  $4 \times 4 \times 4$  conventional (non-primitive)  $fm\bar{3}m$  cell under periodic boundary conditions was considered as a starting structure. The lattice parameter was set to the experimental value of the host matrix before relaxation (see table 2). The forces acting on each ion were obtained by the Busing-Ida type [29, 30] empirical potential fields by Arima *et al* [31–33]. We will further denote this as the Arima potential set.

The Arima potential set was developed to reproduce actinide oxide system properties, in particular lattice parameter, bulk modulus and thermal conductivity [31–33]; it has been extensively tested in the literature and was therefore selected for this study [31–34]. The consistent potential set covers the U, Pu, Am, Np and O ion descriptions, which could be used to define pairwise interactions in solids. The potential energy  $V(r_{ij})$ , between two ions  $i$  and  $j$  at a distance apart  $r_{ij}$  is expressed by the following form:

$$V(r_{ij}) = \frac{(\xi e)^2 Z_i Z_j}{4\pi \epsilon_0 r_{ij}} + f_o(b_i + b_j) \exp\left(\frac{a_i + a_j - r_{ij}}{b_i + b_j}\right) - \frac{c_i c_j}{r_{ij}^6} \quad (1)$$

The parameters  $a_i$ ,  $b_i$ ,  $c_i$  appearing in the interatomic potential function are given in table 1. The first term of equation (1) simulates the electrostatic interaction between point charges with  $\epsilon_0$ , the vacuum permittivity. The electric charge on each atom is assumed to be 67.5% ( $=\xi$ ) of the formal charge ( $Z_i$ ). Classical Ewald summation techniques were used to handle long-range electrostatic interactions in three dimensions [35]. The second term with  $f_o$ , adjustable parameter expresses the short-range repulsion of overlapping electronic shells, and the third term expresses the van der Waals attraction as a simple inverse power function. In this study the pairwise interactions were evaluated only up to a cut-off distance of 1.1 nm.

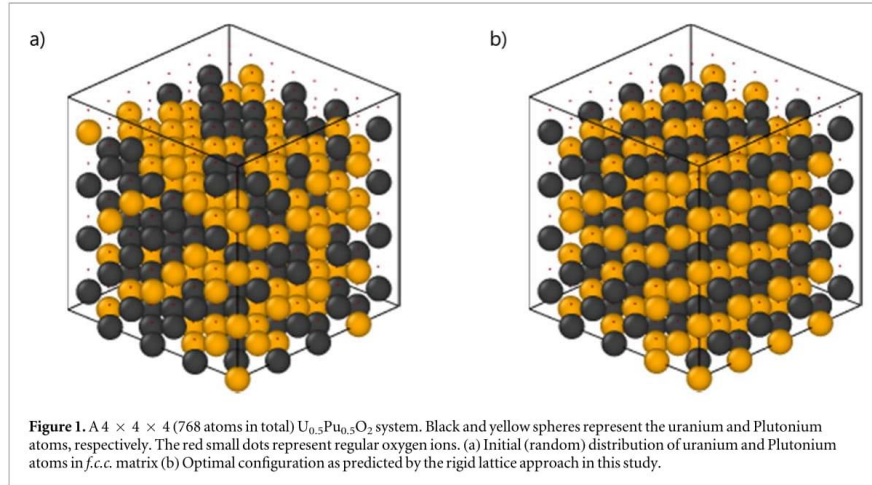
In the stoichiometric simple oxide  $AnO_2$  ( $An = U, Pu, Am$  or  $Np$ ), a stable  $An^{4+}$  is generally considered to maintain the system charge neutral [20–22]. In the present study, a perfect system was created, meaning that the oxygen to metal ratio will always remain 2 and the actinide atoms are always sitting in the unit cell of the fluorite-like cation sites. To describe the actinide charge state in a stoichiometric complex mixed oxide system, a common value of (4+) was considered, as confirmed by previous research conducted by Kato and Konichi [23]. However, combinations of other oxidation states e.g. (3+, 5+, 6+), which would also correspond to overall neutrality, were not applied for this study.

The lattice parameters were investigated via energy minimization techniques at 0 K. The atomic coordinates and lattice vectors were relaxed until the zero strain with the conjugate gradient algorithm implemented in LAMMPS [28]. There are two advantages for the calculation of system properties at 0 K for EP studies. The first one is to check whether the empirical potential is correctly implemented as a pre-validation. Second, a fundamental understanding of the system behaviour can be gained by ignoring the atomic vibrations. To address the relationship between lattice parameter of Am, Np bearing MOX fuel as a function of atomic fractions (at%), a static approach at 0 K was followed in this study.

However, for the experimental validation 300 K were used to simulate room temperature conditions, while neglecting standard atmospheric pressure of 0.1 MPa. The equation of motion was integrated with velocity-Verlet algorithm with the unit time step ( $\Delta t$ ) of 2 femto-second. The simulations were carried out under NPT (constant number of ions, temperature and pressure) conditions which were controlled by the canonical dissipative Nosé-Hoover thermostat and barostat with relaxation time of 0.1 ps and 0.5 ps, respectively. The time for the system to reach equilibrium was 10 ps and the measured lattice parameter were averaged over the next 10 ps.

### 2.2. Exploration of configuration space

The configurational space for the  $U_{1-y-y'-y''}Pu_yAm_{y'}Np_{y''}O_2$  system was explored in this empirical potential study, also considered as the lattice configuration of a solid solution. The exploration of such an arrangement is a



demanding task, given that the number of cases to be addressed increases in a combinatorial way for the composition considered. For example, in case of a binary oxide system  $U_{1-y}Pu_yO_2$ , the number of combinations is expressed as  $\left[ \frac{N!}{(N-n)! \times n!} \right]$ , with  $N$  being the number of accessible sites (256) for  $4 \times 4 \times 4$  unit-cell, and  $n = (y \times 256)$ , the number of Pu replaced by the U lattice position. Similarly, if the system of interest is  $U_{1-y-y'}Pu_yAm_{y'}O_2$ , the number of possible combinations becomes  $\left[ \frac{N!}{(N-n)! \times n!} \right] \left[ \frac{(N-n)!}{(N-n-m)! \times m!} \right]$  with  $m = (y' \times 256)$ , the number of Am atoms distributed in the simulation box, etc. In order to optimize the calculation time, the rigid lattice method was tested [27].

In the rigid lattice approach, the non-relaxed and the relaxed configuration maps were demonstrated to be qualitatively similar. To address the energy gain issue due to the permutation of the U, Pu, Am or Np ions the non-relaxed configurations were used. Initially, a host  $UO_2$  lattice was created according to the potential predictions of the atomic coordinates (cf table 3). The Pu, Am or Np ions were randomly distributed as substitutes in the uranium sublattice. The optimal configuration was found then, by coupling the simulation system with a Monte Carlo-Metropolis algorithm, which dictates the swap probabilities to be always in the direction of energy loss [28].

The method was validated for the case of  $U_{0.5}Pu_{0.5}O_2$ ; a homogeneous mixture was observed, as illustrated by figure 1; no clustering or separate  $UO_2$ - $PuO_2$  phases were predicted, which is in line with recent experiments [21]. The systematic configuration space exploration confirms that the minimum energy configuration is indeed reached. The convergence to the energy minimum was observed after about 20,000 montecarlo steps. Based on this computing time gain and efficiency performance, the method is expected to facilitate the search for optimum configurations when more complex oxides such as  $U_{1-y-y'}Pu_yAm_{y'}Np_{y''}O_2$  are at play.

### 3. Results and discussions

The lattice parameters for the solid solution of  $U_{1-y-y'}Pu_yAm_{y'}Np_{y''}O_2$  system in the range of  $y \leq 60\%$  and  $y' (=y'') \leq 5\%$  were investigated by this empirical potential study. In a first step, the single oxide simulations were performed as a pre-validation to check whether the selected potentials were used properly. Then, the assesment was extended to the binary and more complex oxides. The resulting lattice parameters from this study and the ionic radii model were eventually compared with the available experimental data.

The standard ionic radii model for the lattice parameter ( $a_0$ ) of the *f.c.c.* cell is expressed as;

$$a_0 = \frac{4}{\sqrt{3}}(r_c + r_a) \quad (2)$$

In equation (2) the body diagonal of the unit-cell is  $\sqrt{3} a_0$  and one-quarter of the body diagonal is the  $r_c$  and  $r_a$  distance. Where  $r_c$  and  $r_a$  are the ionic radius of cation and anion, respectively. In order to express the lattice parameter of the  $U_{1-y-y'}Pu_yAm_{y'}Np_{y''}O_2$  system based on ionic radii, equation (3) was derived from equation (2).



**Table 2.** The ionic radii corresponding to CNs 8 for cations and 4 for anions in a perfect f.c.c fluorite structure.

Ionic species	Ionic radius (Å)	
	Shannon [38]	Kato & Konashi [23]
U <sup>4+</sup>	1.00	0.9972
Np <sup>4+</sup>	0.98	0.9805
Pu <sup>4+</sup>	0.96	0.9642
Am <sup>4+</sup>	0.95	0.9539
O <sup>2-</sup>	1.38	1.3720

**Table 3.** Lattice parameters predicted by the consistent potential set of Arima *et al* [31–33]. Equation (2) was used to calculate the lattice parameter of actinide oxides together with the ionic radii provided by Shannon [38] and Kato & Konashi [23]. The two models' results were compared with available experimental data at 300 K.

	Lattice parameters (Å)				
	This work (0 K)	This work (300 K)	Shannon [38]	Kato & Konashi [23]	Experiment (300 K)
UO <sub>2</sub>	5.454	5.469	5.496	5.471	5.470 [40]
PuO <sub>2</sub>	5.380	5.395	5.404	5.395	5.398 [41]
AmO <sub>2</sub>	5.359	5.375	5.381	5.371	5.376 [42]
NpO <sub>2</sub>	5.419	5.433	5.450	5.433	5.434 [43]

$$a_0 = \frac{4}{\sqrt{3}} [(1 - y - y' - y'')r_{U^{4+}} + yr_{Pu^{4+}} + y'r_{Am^{4+}} + y''r_{Np^{4+}} + r_{O^{2-}}] \quad (3)$$

It is well known that the ionic radius varies significantly with valence and coordination number (CN) of the ions. In case of a stoichiometric *f.c.c.* fluorite structure, CNs are 8 for cations and 4 for anions. In this study, ionic radii were taken from the Shannon [38] and Kato and Konashi [23], which are shown in table 2. Although Shannon's set is most widely used, it was assembled in a rather generic way to reproduce the average interatomic distances in solids [38], which was revised and adjusted by Kato and Konashi for a specific AnO<sub>2</sub> (An = U, Pu, Am or Np) system [23].

### 3.1. Simple oxides

Table 3 shows the lattice parameters for the simple oxides which were predicted by the consistent empirical potential set of Arima *et al* [31–33]. For UO<sub>2</sub>, the calculated lattice parameter of 5.454 Å agrees with the critical assessment of the interatomic potential for nuclear fuel published by Bertolus *et al* [39]. This value is in good agreement with 5.455 Å, the 0 K extrapolation of experimental data [40]. At 300 K, both calculations and experiments prove to be in good agreement for all the actinide oxides, as shown in table 3.

The lattice parameters of AnO<sub>2</sub> (An = U, Pu, Am or Np) were calculated with the standard radii model. Equation (2) was used together with the ionic radii provided by Shannon [38] and Kato and Konashi [23] (cf table 3). The ionic radii provided by Shannon [38] generally overestimates the actinide oxide system lattice parameter, while Kato and Konashi [23] reproduces good results in the range of  $\pm 0.001$  Å. Therefore, Kato and Konashi data were selected for further investigation [23].

### 3.2. Binary oxide system

Binary oxide U<sub>1-y</sub>Pu<sub>y</sub>O<sub>2</sub>, U<sub>1-y</sub>Am<sub>y</sub>O<sub>2</sub>, U<sub>1-y</sub>Np<sub>y</sub>O<sub>2</sub> lattice configurations were predicted by the rigid lattice method [27]. From that configuration, system lattice parameters were calculated at 0 K. Figure 2(a) shows that the linear relation (also known as Vegard's law) between lattice parameter and content *y*, for the binary oxide system was observed. To increase the reliability of the current research, the excess energy (or mixing enthalpy at 0 K) was investigated additionally according to the following expression:

$$\Delta E_{mix} = E^{A+B} - (y_A E^A + y_B E^B) \quad (4)$$

Where E<sup>A+B</sup> is the energy of A and B binary solid solution, E<sup>A</sup> and E<sup>B</sup> are the standard lattice energies of component A and B, *y*<sub>A</sub> and *y*<sub>B</sub> are the mole fractions of component A and B, respectively. The whole range of calculated  $\Delta E_{excess}$  over the composition is presented in figure 2(b) The calculated excess energies for U<sub>1-y</sub>Pu<sub>y</sub>O<sub>2</sub>, U<sub>1-y</sub>Am<sub>y</sub>O<sub>2</sub> and U<sub>1-y</sub>Np<sub>y</sub>O<sub>2</sub> fit well with a polynomial shape that corresponds to the homogeneous cubic adjustment of the mixed oxide system as a function of composition. Furthermore, the observed trend in  $\Delta E_{mix}$  is considered to follow the same trends as the standard ionic radii as tabulated in table 2. In a fixed host matrix

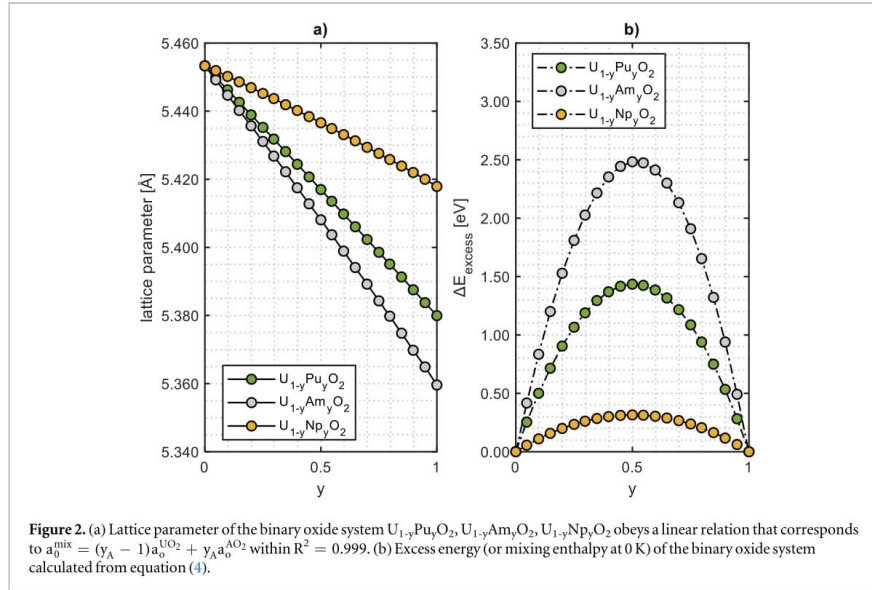


**Figure 2.** (a) Lattice parameter of the binary oxide system  $U_{1-y}Pu_yO_2$ ,  $U_{1-y}Am_yO_2$ ,  $U_{1-y}Np_yO_2$  obeys a linear relation that corresponds to  $a_0^{\text{mix}} = (y_A - 1)a_0^{UO_2} + y_A a_0^{AO_2}$  within  $R^2 = 0.999$ . (b) Excess energy (or mixing enthalpy at 0 K) of the binary oxide system calculated from equation (4).

which is  $UO_2$  in our case, the relation  $r_{Np^{4+}} > r_{Pu^{4+}} > r_{Am^{4+}}$  corresponds to the  $\Delta E_{\text{mix}}^{U_{1-y}Np_yO_2} < \Delta E_{\text{mix}}^{U_{1-y}Pu_yO_2} < \Delta E_{\text{mix}}^{U_{1-y}Am_yO_2}$  relation.

### 3.3. Complex $U_{1-y-y'}-y''Pu_yAm_yNp_{y'}O_2$ system

Finally, the lattice parameters were compared with available experimental data for a more complex  $U_{1-y-y'}-y''Pu_yAm_yNp_{y'}O_2$  system. Minor actinide fractions were adjusted up to a share of 5 at% while Pu in the host  $UO_2$  matrix was kept in the range of 5–60 at%. Figures 3(a) and (b) illustrate the effect of minor actinides on the lattice parameter of MOX fuel matrix for a complex  $U_{1-y-y'}Pu_yAm_yO_2$  (a) and  $U_{1-y-y'}-y''Pu_yAm_yNp_{y'}O_2$  system (b) as predicted by Arima *et al* at 0 K [31–33]. From both figures, it can be seen that the lattice parameter decreases indeed linearly with an increasing amounts of MA dissolved in the MOX fuel matrix. However, for a fixed Pu concentration, changing the Am ( $y'$ ) - Np ( $y''$ ) fraction, with  $y' = y''$  (cf figure 3(b)), results in a sharper decrease than changing the share of Am ( $y'$ ) in the MOX fuel. This is in line with the experimental work published by Kato and Konashi [23]. Figure 3(c) shows the lattice parameter comparison of this study's EP results to the experimental data [21, 23], and the results of ionic radii model as calculated with equation (3). A good agreement between measured and calculated data suggests that the lattice parameter of  $U_{1-y-y'}-y''Pu_yAm_yNp_{y'}O_2$  obeys Vegard's law.

## 4. Conclusions

The lattice parameters of up to 5 at% MA containing MOX fuel with maximum 60 at% Pu were addressed by empirical potential based atomic scale simulations. The lattice configurations were predicted by a systematic optimization method called rigid lattice method [27]. The method could be easily applied to other selected Buckingham variants, used to address the ionic oxide crystal [44]. However, one of the advantages of the Arima potential set [31–33] is, that it can be relatively easily extended to other oxidation states appearing in non-stoichiometry, e.g. (3+, 5+, 6+), which will be explored in our future works.

The following results were found:

- The configurational space exploration of the arrangement of Pu, Am, Np in the host  $UO_2$  matrix was shown to be highly effective with a rigid lattice approach—where no relaxation is performed in a first stage—in combination with a Monte Carlo- Metropolis particle swapping method.
- The lattice parameter of the binary oxide system  $U_{1-y}Pu_yO_2$ ,  $U_{1-y}Am_yO_2$ ,  $U_{1-y}Np_yO_2$  obeys a linear relation that corresponds to  $a_0^{\text{mix}} = (y_A - 1)a_0^{UO_2} + y_A a_0^{AO_2}$ .

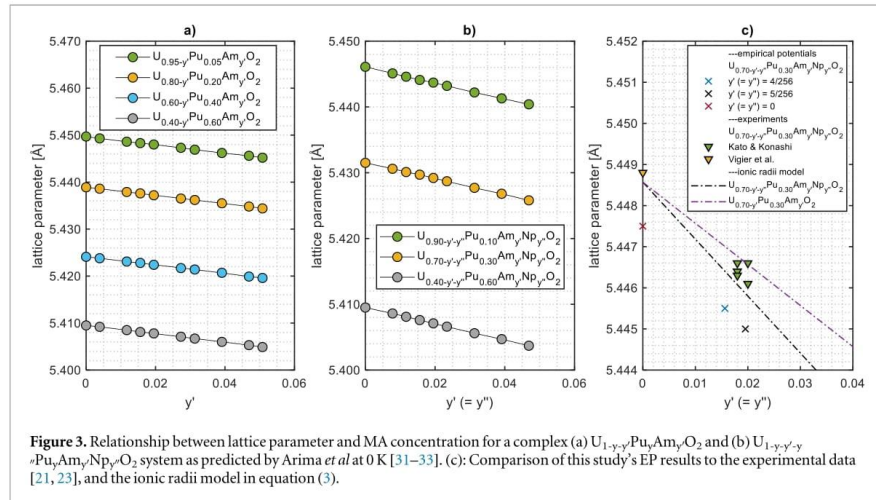


**Figure 3.** Relationship between lattice parameter and MA concentration for a complex (a)  $U_{1-y-y'}Pu_yAm_yO_2$  and (b)  $U_{1-y-y'}Pu_yAm_yNp_yO_2$  system as predicted by Arima *et al* at 0 K [31–33]. (c): Comparison of this study's EP results to the experimental data [21, 23], and the ionic radii model in equation (3).

- The lattice parameter of a complex  $U_{1-y-y'}Pu_yAm_yO_2$  b)  $U_{1-y-y'}Pu_yAm_yNp_yO_2$  system decreases linearly with an increasing amount of MA dissolved in the MOX fuel matrix.

### Acknowledgments

This work is dedicated to the memory of Prof. Alain Dubus, ULB, Bruxelles, Belgium. The financial support of this research by SCK CEN is gratefully acknowledged.

### Data availability statement

The data that support the findings of this study are available upon reasonable request from the authors.

### Declaration of competing interest

The authors declare that there are no known competing financial interests or personal relationships that could have appeared to influence the work reported in this paper.

### CRediT authorship contribution statement

**Emre Caglak:** Conceptualization, Methodology, Investigation, Resources, Writing - original draft, Writing—review & editing, Visualization. **Pierre-Etienne Labeau:** Conceptualization, Writing—review & editing, Supervision, Project administration, Funding acquisition.

### ORCID iDs

Emre Caglak  <https://orcid.org/0000-0003-1586-7187>

### References

- [1] Piroo I 2016 *Handbook of Generation IV Nuclear Reactors* (Cambridge: Woodhead Publishing)
- [2] Olander D R 1976 *Fundamental Aspects of Nuclear Reactor Fuel Elements: Solutions to Problems* (Berkeley (USA): California Univ) Dept. of Nuclear Engineering
- [3] Behera R K, Deo C S and Xu H 2013 Effect of the substitution off-electron elements on the structure and elastic properties of UO<sub>2</sub> *J. Nucl. Mater.* **433** 504–13
- [4] Jossou E, Malakkal L, Ranasingh J, Szpunar B and Szpunar J 2020 Thermophysical properties of (UxAm1 – x) O<sub>2</sub> MOX fuel *Comput. Mater. Sci.* **172** 109324

- [5] Njifon I C, Bertolus M, Hayn R and Freyss M 2018 Electronic structure investigation of the bulk properties of uranium–plutonium mixed oxides (U, Pu) O<sub>2</sub> *Inorg. Chem.* **57** 10974–83
- [6] Ma L, Atta-Fynn R and Ray A K 2012 Elemental and mixed actinide dioxides: an *ab initio* study *J. Theor. Comput. Chem.* **11** 611–29
- [7] Schoenes J 1978 Optical properties and electronic structure of UO<sub>2</sub> *J. Appl. Phys.* **49** 1463–5
- [8] Yamashita T, Nitani N, Tsuji T and Inagaki H 1997 Thermal expansions of NpO<sub>2</sub> and some other actinide dioxides *J. Nucl. Mater.* **245** 72–8
- [9] Fahey J A, Turcotte R P and Chikalla T D 1974 Thermal expansion of the actinide dioxides *Inorg. Nucl. Chem. Lett.* **10** 459–65
- [10] Hurtgen C and Fuger J 1977 Self-irradiation effects in americium oxides *Inorg. Nucl. Chem. Lett.* **13** 179–88
- [11] Chikalla T D and Eyring L 1968 Phase relationships in the americium–oxygen system *J. Inorg. Nucl. Chem.* **30** 133–45
- [12] Vauchy R, Joly A and Valot C 2017 Lattice thermal expansion of Pu<sub>1–y</sub>Am<sub>y</sub>O<sub>2–x</sub> Plutonium–americium mixed oxides *J. Appl. Crystallogr.* **50** 1782–90
- [13] Vauchy R, Belin R C, Robisson A-C, Lebreton F, Aufore L, Scheinost A C and Martin P M 2016 Actinide oxidation state and O/M Ratio in hypostoichiometric uranium–plutonium–americium U<sub>0.750</sub>Pu<sub>0.246</sub>Am<sub>0.004</sub>O<sub>2–x</sub> Mixed Oxides *Inorg. Chem.* **55** 2123–32
- [14] Njifon I C and Torres E 2020 Phonons and thermophysical properties of U<sub>1–y</sub>Pu<sub>y</sub>O<sub>2</sub> mixed oxide (MOX) fuels *J. Nucl. Mater.* **537** 152158
- [15] Elorrieta J M, Manara D, Bonales L J, Vigier J F, Dieste O, Naji M, Belin R C, Baonza V G, Konings R J M and Cobos J 2017 Raman study of the oxidation in (U, Pu) O<sub>2</sub> as a function of Pu content *J. Nucl. Mater.* **495** 484–91
- [16] Prieur D, Lebreton F, Caisso M, Martin P M, Scheinost A C, Delahaye T and Manara D 2016 Melting behaviour of americium-doped uranium dioxide *J. Chem. Thermodyn.* **97** 244–52
- [17] Lebreton F, Belin R C, Prieur D, Delahaye T and Blanchart P 2012 *In Situ* Study of the Solid-State Formation of U<sub>1–x</sub>Am<sub>x</sub>O<sub>2 ± δ</sub> Solid Solution *Inorg. Chem.* **51** 9369–75
- [18] Chollet M, Belin R C, Richaud J-C and Reynaud M 2012 Phase relationships in the U–Np–O system *Procedia Chem.* **7** 472–6
- [19] Epifano E, Beneš O, Válu O S, Zappey J, Lebreton F, Martin P M, Guéneau C and Konings R J M 2017 High temperature heat capacity of (U, Am)O<sub>2 ± x</sub> *J. Nucl. Mater.* **494** 95–102
- [20] Epifano E *et al* Extreme multi-valence states in mixed actinide oxides *Commun. Chem.* **2** 2019 1–11
- [21] Vigier J-F, Martin P M, Martel L, Prieur D, Scheinost A C and Somers J 2015 Structural investigation of (U<sub>0.7</sub>Pu<sub>0.3</sub>)O<sub>2–x</sub> mixed oxides *Inorg. Chem.* **54** 5358–65
- [22] Martel L, Vigier J-F, Prieur D, Nourry S, Guiot A, Dardenne K, Boshoven J and Somers J 2014 Structural investigation of Uranium–Neptunium mixed oxides using XRD, XANES, and 17O MAS NMR *J. Phys. Chem. C* **118** 27640–7
- [23] Kato M and Konashi K 2009 Lattice parameters of (U, Pu, Am, Np) O<sub>2–x</sub> *J. Nucl. Mater.* **385** 117–21
- [24] Yun Y and Oppeneer P M 2011 First-principles design of next-generation nuclear fuels *MRS Bull.* **36** 178–84
- [25] Petit L, Svane A, Szotek Z, Temmerman W M and Stocks G M 2010 Electronic structure and ionicity of actinide oxides from first principles *Phys. Rev. B* **81** 45108
- [26] Wen X-D, Martin R L, Henderson T M and Scuseria G E 2013 Density functional theory studies of the electronic structure of solid state actinide oxides *Chem. Rev.* **113** 1063–96
- [27] Caglak E, Govers K, Lamoen D, Labeau P-E and Verwerft M 2020 Atomic scale analysis of defect clustering and predictions of their concentrations in UO<sub>2 + x</sub> *J. Nucl. Mater.* **541** 152403
- [28] Plimpton S 1995 Fast parallel algorithms for short-range molecular dynamics *J. Comput. Phys.* **117** 1–19
- [29] Busing W R 1970 An interpretation of the structures of alkaline earth chlorides in terms of interionic forces *Trans. Am. Cryst. Assoc.* **6** 57–72
- [30] Ida Y 1976 Interionic repulsive force and compressibility of ions *Phys. Earth Planet. Inter.* **13** 97–104
- [31] Uchida T, Arima T, Idemitsu K and Inagaki Y 2009 Thermal conductivities of americium dioxide and sesquioxide by molecular dynamics simulations *Comput. Mater. Sci.* **45** 229–34
- [32] Arima T, Yamasaki S, Inagaki Y and Idemitsu K 2005 Evaluation of thermal properties of UO<sub>2</sub> and PuO<sub>2</sub> by equilibrium molecular dynamics simulations from 300 to 2000 K *J. Alloys Compd.* **400** 43–50
- [33] Arima T, Yoshida K, Matsumoto T, Inagaki Y and Idemitsu K 2014 Thermal conductivities of ThO<sub>2</sub>, NpO<sub>2</sub> and their related oxides: molecular dynamics study *J. Nucl. Mater.* **445** 175–80
- [34] Balboa H, Brutzel L V, Chartier A and Bouar Y L 2017 Assessment of empirical potential for MOX nuclear fuels and thermomechanical properties *J. Nucl. Mater.* **495** 67–77
- [35] Ewald P 1921 Evaluation of optical and electrostatic lattice potentials *Ann. Phys.* **64** 253–87
- [36] Hayashi H, Sagawa R, Inaba H and Kawamura K 2000 Molecular dynamics calculations on ceria-based solid electrolytes with different radius dopants *Solid State Ionics* **131** 281–90
- [37] Inaba H, Sagawa R, Hayashi H and Kawamura K 1999 Molecular dynamics simulation of gadolinia-doped ceria *Solid State Ionics* **122** 95–103
- [38] Shannon R D 1976 Revised effective ionic radii and systematic studies of interatomic distances in halides and chalcogenides *Acta Crystallogr. Sect. A Cryst. Physics, Diffraction, Theor. Gen. Crystallogr.* **32** 751–67
- [39] Bertolus M, Freyss M, Krack M and Devanathan R 2015 *Assessment of Current Atomic Scale Modelling Methods for the Investigation of Nuclear Fuels Under Irradiation: Example of Uranium Dioxide* (United states: No. NEA-NSC-R-2015-5)
- [40] Grønsvold F 1955 High-temperature X-ray study of uranium oxides in the UO<sub>2</sub> U<sub>3</sub>O<sub>8</sub> region *J. Inorg. Nucl. Chem.* **1** 357–70
- [41] Haschke J M, Allen T H and Morales L A 2000 Reaction of Plutonium dioxide with water: formation and properties of PuO<sub>2 + x</sub> *Science (80-. )*. **287** 285–7
- [42] Asprey L B, Ellinger F H, Fried S and Zachariasen W H 1955 Evidence for quadrivalent curium: X-ray data on curium oxides *J. Am. Chem. Soc.* **77** 1707–8
- [43] Yamashita T, Nitani N, Tsuji T and Kato T 1997 Thermal expansion of neptunium–uranium mixed oxides *J. Nucl. Mater.* **247** 90–3
- [44] Buckingham R A 1938 The classical equation of state of gaseous helium, neon and argon *Proc. R. Soc. London. Ser. A. Math. Phys. Sci.* **168** 264–83